# Aero-Propulsive Analysis of an Over-The-Wing Distributed Propulsion System

## A numerical investigation into the effect of propeller position and wing shape

N.M. Dekkers

TU Delft Delft University of Technology

# Aero-Propulsive Analysis of an Over-The-Wing Distributed Propulsion System

## A NUMERICAL INVESTIGATION INTO THE EFFECT OF PROPELLER POSITION AND WING SHAPE

by

N.M. Dekkers
4224043

To obtain the degree of Master of Science
at the Delft University of Technology,
to be defended publicly on Tuesday December 21, 2021 at 14:00

| | | |
|---|---|---|
| Thesis committee: | L. L. M. Veldhuis | TU Delft, Chairman, Supervisor |
| | R. de Vries | TU Delft, Supervisor |
| | W. J. Baars | TU Delft, Examiner |
| | A. H. van Zuijlen | TU Delft, Examiner |

An electronic version of this thesis is available at http://repository.tudelft.nl/

TU Delft Delft University of Technology

# PREFACE

This project will be the closing step in my studies at the University of Technology in Delft. I've gained numerous skills over the years for which I am very thankful. Additionally, I'm thankful for the friends and experiences gained over this period. This thesis work is the result of a lot of hard work during a challenging and busy period of my life and I am happy to finalize this chapter.

First and foremost, I would like to thank Reynard de Vries, my daily supervisor, for the provided guidance and knowledge over the entire duration of this thesis. I'm still amazed about the sheer amount of continued positive attitude and support I have received over my thesis period, even if this meant very early meetings on a Friday morning. Without his help this thesis would not be where it currently is. Special thanks to Leo Veldhuis for his expertise, enthusiasm and critical remarks, which helped me greatly in my understanding of this project. I would like to thank Nando van Arnhem for his expertise, guidance and support on the propeller performance modeling software he provided. Additional thanks to the members of the propulsion research group for the interesting discussions provided.

Many thanks to my close friends and family for their continued support even if that meant them not hearing from me for long periods. Special thanks to Jeroen Seegers for his continued support in the final stages of my thesis for making me realize my midnight writing automatically comes with serious grammatical flaws.

*Nick Dekkers*
*Delft, December 2021*

# SUMMARY

Aviation will have to adapt to meet the goals for reduction of emissions and to limit the environmental impact of air travel with the ever increasing demand in air travel. A next step in aviation will include a step in power train hybridization. This hybridization comes with opportunities for new aircraft configurations and propeller integration concepts. The increased flexibility of propeller positioning will allow propellers to be positioned in more favorable positions, benefiting the overall aero-propulsive performance. One of the concepts with potential of increasing aero-propulsive efficiency is the distributed Over-The-Wing (OTW) propulsive concept.

This thesis aims to gain further understanding into the aero-propulsive performance of the OTW propulsive concept by analyzing the propeller position and inclination, shroud position and inclination and the wing shape in proximity of the propeller. Previous investigation into this concept has been incomplete and has occasionally been contradicting. This thesis therefore presents a numerical investigation to a wide array of geometrical parameters which define the OTW propulsive configuration with the aim to increase understanding of the aerodynamic interaction between the wing and propeller in a cruise condition. From this, a basis for future design and optimization is aimed to be established.

This investigation employs an automated computational framework, which has been set-up to be able to analyze a wide array of designs. This computational framework, allowing for automated geometry creation, meshing, solving and post-processing, is set-up to constrain the lift coefficient ($C_L = 0.7272$) and propeller power coefficient ($P_C = 0.162$) to allow for a fair comparison of designs. The performance of the respective geometries is ultimately compared by the figure of merit defined as the product of the lift-to-drag ratio and the system propulsive efficiency. The simulations are run using a steady Computational Fluid Dynamics (CFD) Reynolds-Averaged Navier-Stokes (RANS) model where the propeller is modeled through the use of a actuator disk model. The flow as observed by the OTW propeller is highly non-uniform and therefore the propeller modeling approach allows for accurate, but computationally efficient evaluation of the propeller performance, by making use of a pre-computed sensitivity map containing the isolated performance of the propeller. To assess the validity and accuracy of these models, several aspects of the model are validated to existing experimental data. The propeller induced pressure distributions on the wing showed fair agreement to the experimental pressure distributions, but lacked the capability of predicting the downstream impact on the wing following the introduction of the propeller at high thrust settings. At more moderate thrust coefficients ($C_T = 0.2$), similar to the ones used in the upcoming results, the general qualitative behavior of the propeller induced pressure distributions are comparable to experimental results, but the peak pressure values are expected to vary following a overestimation of the upstream pressure peak of 28%.

The uninstalled configuration is used as a reference configuration and consists of the

summation of the isolated performance of the wing, isolated performance of the nacelle and uninstalled performance of the propeller. A baseline OTW configuration is defined which includes a propeller mounted at $x_p$ = 0.85c and a shroud geometry positioned above the propeller. The inclusion of a shroud geometry has a significant impact on the lift-to-drag ratio of the system following the additional wetted area introduced, which increases the friction drag. However the inclusion of a shroud geometry is observed to have the potential of reducing the axial velocity into the propeller plane substantially increasing propulsive efficiency. Studying this mechanism by varying the shroud incidence angle showed that this mechanism can be enhanced by increasing the shroud incidence, however this introduces a pressure drag penalty following the rotation of the normal force of the shroud. The second mechanism observed increasing the propeller efficiency in the OTW configuration is the wing induced downwash onto the propeller plane. The propeller efficiency is observed to increase with increasing angle of attack, which in the OTW configuration is present even when the propeller axis is aligned with the direction of flight. This results in an increase in propeller efficiency, without any additional penalty of propeller normal forces reducing the propulsive efficiency. Exploiting this mechanism by inclining the propeller into the wing geometry to create a larger negative angle of attack to the propeller disk area is observed to increase the propulsive efficiency, but this ultimately is penalized significantly by additional drag following an increased system angle of attack required. Ultimately the un-shrouded baseline wing showed a 0.3% gain in the figure of merit over the uninstalled configuration, but the shrouded baseline configuration showed a 20.8% reduction in the figure of merit following the additional shroud pressure drag. The local wing shape variations showed potential in increasing the propeller efficiency in some designs following either an increase in downwash or a reduction in axial flow velocity into the propeller disk. Wing geometries increasing the thickness at the propeller axial location observed additional drag reduction by introducing a propeller. The changing wing geometries did however not improve the figure of merit when compared to the baseline OTW configuration. The axial position of the propeller is observed to have a strong sensitivity to the performance of the system and a propeller located at 0.4c was found to observe the highest lift-to-drag ratio following a strong reduction of pressure drag. A more downstream axial position of the propeller is observed to increase propulsive efficiency following lower axial inflow velocities to the propeller disk. The propeller tip clearance and shroud axial location showed relatively small sensitivity when compared to the other design variables investigated in this study. A optimization orienting the propeller inclination and shroud inclination at a propeller axial position of 0.8c was observed to increase the figure of merit by 2.8% as compared to the baseline OTW configuration.

# CONTENTS

# LIST OF FIGURES

# List of Tables

# NOMENCLATURE

## Latin Symbols

| | |
|---|---|
| $A_p$ | Propeller disk area [$m^2$] |
| $B$ | Number of propeller blades [-] |
| $c$ | Chord length [m] |
| $c_p$ | Specific fuel consumption [-] |
| $C_D$ | Drag coefficient [-] |
| $C_f$ | Skin friction coefficient [-] |
| $C_L$ | Lift coefficient [-] |
| $C_P$ | Power coefficient [-] |
| $C_Q$ | Torque coefficient [-] |
| $C_T$ | Thrust coefficient [-] |
| $C'_Z$ | Vertical in-plane force coefficient [-] |
| $D_p$ | Propeller diameter [m] |
| $E$ | Energy [J] |
| $f$ | Body force [N] |
| $F_{Z'}$ | Propeller vertical force [N] |
| $h_i$ | Normalized cell size [m] |
| $i$ | Inclination [deg] |
| $J$ | Propeller advance ratio [-] |
| $l$ | Length [m] |
| $K$ | Figure of merit [-] |
| $M$ | Mach number [-] |
| $n$ | Propeller rotational speed [$s^{-1}$] |
| $n_i$ | Number of cells [-] |
| $p$ | Pressure [Pa] |
| $P$ | Power [W] |
| $P_C$ | Propeller shaft power coefficient [-] |
| $Q$ | Torque [Nm] |
| $r$ | Propeller radial position [m] |
| $R$ | Range [m] |
| $Re$ | Reynolds number [-] |
| $S$ | Surface area [$m^2$] |
| $t$ | Time [s] |
| $T$ | Thrust [N] |
| $T'$ | Sectional thrust [N/m] |
| $T_C$ | Propeller thrust coefficient [-] |

| | |
|---|---|
| $T'_C$ | Normalized sectional thrust coefficient [$m^{-1}$] |
| $u$ | Axial velocity [m/s] |
| $u_*$ | Friction velocity [m/s] |
| $U_\phi$ | Uncertainty [-] |
| $v$ | Span-wise velocity [m/s] |
| $V_i$ | Domain volume [$m^3$] |
| $V_a$ | Axial velocity [$m/s$] |
| $V_t$ | Tangential velocity [$m/s$] |
| $V_\infty$ | Free-stream velocity [$m/s$] |
| $w$ | Vertical velocity [m/s] |
| $W$ | Weight [kg] |
| $x_{i,j}$ | Spatial coordinates [m] |
| $X$ | Global axial coordinate [m] |
| $X'$ | Propeller axial coordinate [m] |
| $Y$ | Global span-wise coordinate [m] |
| $Y'$ | Propeller span-wise coordinate [m] |
| $y^+$ | Dimensionless wall distance (y-plus) [-] |
| $y_{cell}$ | Cell height [m] |
| $Z$ | Global vertical coordinate [m] |
| $Z'$ | Propeller vertical coordinate [m] |

# Greek Symbols

| | |
|---|---|
| $\alpha$ | Angle of attack [deg] |
| $\beta$ | Propeller blade pitch angle [deg] |
| $\epsilon$ | Propeller tip clearance [m] |
| $\epsilon_{AM}$ | Regularization constant [-] |
| $\epsilon_d$ | Discretization error [-] |
| $\phi$ | Propeller azimuthal location [deg] |
| $\eta$ | Propeller efficiency [-] |
| $\eta_x$ | Actuator disk axial regularization function [-] |
| $\eta_\phi$ | Actuator disk azimuthal regularization function [-] |
| $\mu$ | Dynamic viscosity [$kgm^{-1}s^{-1}$] |
| $\theta_{sw}$ | Swirl angle [deg] |
| $\rho$ | Density [$kg/m^3$] |
| $\sigma$ | Standard deviation [-] |
| $\tau_w$ | Wall shear stress [Pa] |
| $\tau_{i,j}$ | Stress tensor [] |
| $\Omega$ | Angular velocity [$1/s$] |

# Additional Sub- and Superscripts

| | |
|---|---|
| $\infty$ | Free stream condition |
| a | Axial |
| eff | Effective |
| iso | Isolated |
| max | Maximum |
| min | Minimum |
| OTW | Over-The-Wing |
| p | Propeller |
| ref | Reference |
| sec | Section |
| sys | System |
| t | Tangential |

# List of Abbreviations

| | |
|---|---|
| BEM | Blade Element Momentum |
| BLI | Boundary Layer Ingestion |
| BSL | Baseline |
| CAD | Computer Aided Design |
| CFD | Computational Fluid Dynamics |
| CST | Class-Shape-Transformation |
| DEP | Distributed Electric Propulsion |
| eBPR | effective Bypass Ratio |
| EVM | Eddy Viscosity Models |
| GUI | Graphical User Interface |
| HEP | Hybrid Electrical Propulsion |
| MAC | Mean Aerodynamic Chord |
| MTOW | Maximum Take-Off Weight |
| NASA | National Aeronautics and Space Administration |
| OTW | Over-The-Wing |
| OTWDP | Over-The-Wing Distributed Propulsion |
| OTWP | Over-The-Wing Propulsion |
| PCA | Propulsion-Controlled Aircraft |
| PIV | Particle Image Velocimetry |
| RANS | Reynolds-Averaged Navier-Stokes |
| SA | Spalart-Allmaras |
| SNOPT | Sparse Nonlinear Optimizer |
| SQP | Sequential Quadratic Programming |
| STOL | Short Take-Off and Landing |
| TeDP | Turbo-electric Distributed Propulsion |
| TUI | Text User Interface |
| UDF | User-Defined Function |
| VTOL | Vertical Take-Off and Landing |

# I

# BACKGROUND

# 1

# INTRODUCTION

The need for more efficient aircraft has been fueled by the ever increasing demands of travel together with the increased environmental concerns associated with aviation [1]. Improved aircraft–propulsion integration is one of the points of research in the last several years. With the goal of reducing emissions new hybrid electrical power-trains are investigated for their potential role in aircraft following the potential of increased energy conversion and transmission [2]. The ability of electrical propulsors to solely be connected electrically to their energy sources opens up the flexibility of placing the propellers in a more aerodynamically favorable location [1]. New concepts include Distributed Electric Propulsion (DEP) configurations, which with careful integration can allow for improved propulsive efficiency and increase dynamic pressure across the blown surfaces [1]. The investigation on Hybrid Electrical Propulsion (HEP) is based on the potential improvement in efficiency over conventional propulsion systems [3]. A possible way to improve the aero-propulsive interaction using the DEP configurations is to place the propellers over-the-wing opening up opportunities for increased lift-to-drag ratio [4–7] and added thrust vectoring ability.

The 2017 strategic implementation plan from the National Aeronautics and Space Administration (NASA) includes research and development of DEP as one of the goals of the transition to alternative propulsion and energy [8]. This branch of the strategic implementation plan has as end goal to introduce alternative propulsion systems for aircraft of all sizes after the year 2035. Research into HEP and fully electric aircraft is one of the goals mentioned by the Flightpath 2050: Europe's Vision for Aviation [9, 10]. The recent research is kick-started by funding from programs like the European Union Horizon 2020 program, which is part of the Clean Sky 2 program [10].

## 1.1. HISTORICAL CONTEXT

This section serves to give some background on the use and research done on distributed propulsion and over-the-wing propulsion.

An important aspect of the distributed propulsion is that the power source (e.g. batteries or turbo-electric generators) and the thrust-producing propulsor (e.g. electrically-driven propellers or fans) are generally decoupled. This can have a range of benefits with respect to propulsion-airframe integration and it opens up a range of new aircraft configurations and concepts. In the past few years, conceptual and preliminary work has been done on the side of NASA on the research and development of DEP [1, 11–16]. One

of the early NASA DEP concepts is the Turbo-electric Distributed Propulsion (TeDP) concept. In this concept, a number of highly efficient motors powering a set of distributed fans are employed. The power generated for these fans is obtained by a running one or several of gas turbines [1]. This array of propulsors allows for an higher effective Bypass Ratio (eBPR), while still keeping the high efficiency of large diameter engine cores [1].

The TeDP concept from NASA is one of the proposed concepts to meet the goals set by the strategic implementation plan [8]. This concept is based on the use of a distributed propulsion system which uses advanced generation of electric power, which in turn power an array of distributed fans [11]. One of the aircraft concepts making use of this propulsion system is the NASA N3-X [14, 15, 17], as shown in Figure 1.1a. It makes use of an array of distributed propulsors at the upper surface close to the trailing edge of the blended wing body, which is powered by two turbo-electric generators at the wingtips. A more conventional example of DEP is the NASA X-57 [12] concept, which is shown in Figure 1.1b. This fully electric battery powered aircraft uses twelve smaller wing mounted propellers and two larger wing tip mounted propellers [1].

(a) NASA N3-X [1]

(b) NASA X-57 Maxwell [2]

Figure 1.1: NASA distributed electric propulsion concepts.

The over-the-wing distributed propulsion concept finds itself in the early stages of research and development. Several research institutes have published works investigating the aero-propulsive performance and interactions of this concept. Both experimental and numerical studies on Over-The-Wing (OTW) configurations have been performed to gain insight in the aerodynamic interaction effects.

A recent combined experimental and computational study on the over-the-wing propulsion configuration performed by Marcus et al. investigates aero-propulsive performance and dominant flow phenomena of the system [7]. The axial position of the propeller is of large importance to the overall performance of the system. Moving the propeller more aft increases the lift coefficient at constant thrust coefficient. The pressure drag is found lowest at the thickest position on the wing. The propeller efficiency increases by moving the propeller more aft since the a more uniform inflow is found moving the propeller further aft. The optimal propeller location was found to be near the wing trailing edge, where lift is found to increase the most while only giving minimal reduction in efficiency

[1] https://62e528761d0685343e1c-f3d1b99a743ffa4142d9d7f1978d9686.ssl.cf2.rackcdn.com/files/63856/area14mp/w4dwsdhc-1415268974.jpg

[2] https://www.nasa.gov/sites/default/files/thumbnails/image/x-57_maxwell_city.jpg

and pressure drag.

For the medium and long range commercial aircraft, propeller aircraft are superseded by turboprop engines. The use of propeller engines comes with high noise production and a limitation to the cruise mach number. The noise production is increased by placing the propellers over the wing. Additional complications might arise with the use of Over-The-Wing Propulsion (OTWP), since the wing induced velocity on the propeller is not negligible and can lead to loss in efficiency when no proper design integration is performed in the early stages of the design process. The interaction effect the wing has on the propeller results in reduced propulsive efficiency [6, 7, 18] and an increase in unsteadiness of the blade loading when compared to a tractor configuration. This unsteadiness also has influence on the boundary layer, which in turn can cause earlier separation [19–21]. Investigation on this unsteady OTW interaction is found in the research done by L. Müller and J. Friedrichs [22]. Unsteady Reynolds-Averaged Navier-Stokes (RANS) performed on a channel wing in high lift configuration resulted in flow separation on the flap, resulting in a lower lift increment compared to a tractor configuration. Tractor configurations affect the span-wise angle of attack of the wing whereas OTWP affects the upper-surface pressure distribution. The alteration of this pressure distribution effectively changes the airfoil shape and therefore the wing design most likely needs to be adapted for this change to obtain optimal aerodynamic performance.

At this point of time, the most developed type of aircraft which employs DEP in combination with OTWP, are the smaller personal flight/air taxi aircraft. Development of these aircraft is done party by several private start-up companies, which try to create an option for on-demand air service. One of the most developed distributed propulsion aircraft is the Lilium jet (Munich, Germany), shown in Figure 1.2. A full scale prototype of the his aircraft is built and being tested. The jet employs 36 electric powered ducted fans which are installed over-the-wing.

Figure 1.2: Lilium jet [3]

## 1.2. RESEARCH QUESTIONS

With previous studies, the main focus lied in identifying and understanding the aero-propulsive interaction of OTW propulsion configurations [6, 7, 20, 22–25]. In most of the research, this investigation was performed on an unoptimized baseline wing and arbi-

[3] https://img.redbull.com/images/f_auto,q_auto/redbullcom/2017/10/27/79936ad1-0932-47fd-9039-f0e913f7ce22/lilium-jet-vechicle-rendering.jpg

trary inclined propeller. With the importance of the interaction of the wing and propeller however, the placement of the propeller relative to the wing is found to be of a big influence to the overall performance of the system. In several occasions [10, 22], optimization of the wing geometry and propeller position is identified as the next step in the research. As stated by Hoogreef et al. [10] "Additionally, an increase in the propulsive efficiency is expected for adapted wing configurations in which a rectangular duct is combined with wing airfoil shape optimization to arrive at a more uniform inflow field for the over-the-wing distributed fans.". It has been observed that further understanding of the OTW configuration is needed to gain a better understanding of the aerodynamic mechanisms playing a role in the performance of the system. Additionally, the understanding of the impact of several design variables onto the performance of such a system are not yet fully understood.

Based on the current research interest, the research objective of this research is stated as:

*To perform an investigation into the aero-propulsive performance of an over-the-wing distributed-propulsion configuration by analyzing the effect of wing shape and propeller position*

To reach the main objective, the main research question to be answered is:

*How is the aero-propulsive efficiency affected by changing the wing shape and propeller position in an over-the-wing distributed-propulsion configuration?*

To answer this main research question, several sub questions are established which in turn need to be answered:

1. Which type of model can accurately and swiftly estimate the performance of an over-the-wing propeller with constant lift and power coefficients?
   (a) How can the propeller performance be simulated and coupled to the aerodynamic performance of the system?
   (b) Which assumptions need to be made in the aerodynamic model?
   (c) How does experimental data compare to the numerical results obtained?
2. How are the lift, drag and propeller efficiency affected by changing the design parameters of the system?
   (a) How does the shape of the wing affect aero-propulsive efficiency?
   (b) How does the inclusion of a shroud and nacelle structure affect the aero-propulsive efficiency?
   (c) How does the position, tip clearance, diameter and inclination of the propeller affect the aero-propulsive efficiency?
3. How does the overall aero-propulsive performance of the over-the-wing configuration compare to an uninstalled propeller-wing system?

(a) How does the propulsive efficiency of a propeller in an over-the-wing configuration compare to the uninstalled propulsive efficiency?

(b) How is the lift and drag affected by the over-the-wing propulsive configuration?

(c) How does the combined overall aero-propulsive performance compare to an uninstalled system?

## 1.3. THESIS OUTLINE

This research is divided into four main sections, starting off by describing the aerodynamic and research background in Chapter I. In this chapter, Section 2 will describe the aerodynamic background governing the OTW configurations. The method used in this research is described in Chapter II, consisting of the numerical setup as described in Section 3 and the design space as described in Section 4. Chapter III shows the results obtained by the numerical simulations performed. The validation and verification performed is highlighted in Section 5. The main results obtained form this thesis are compared to an isolated propeller-wing system and a baseline OTW configuration, which are described in Section 6. The results obtained from the sensitivity analysis performed are shown in Section 7. The final chapter, Chapter IV, will reflect on the research questions by concluding the work in Section 8 and from this, recommendations on future research will be made in Section 9.

# 2

# AERODYNAMIC BACKGROUND

The goal of this chapter is to define the aerodynamic interaction effects as experienced by the wing and the propeller in the OTW configuration. Both the propeller and the wing influence the flow field, which in turn alters the performance of both of these objects. The theory discussed in this chapter is partly based on existing isolated performance studies and more recent studies investigating these interaction effects in the OTW configuration. Firstly, the performance of isolated propellers is described in Section 2.1. The impact the aerodynamic surfaces have on the propeller performance is described in Section 2.2. The impact the propeller has on the performance of the wing is described in Section 2.3.

## 2.1. ISOLATED PROPELLER AERODYNAMICS

This section briefly explains the working principles of the isolated performance of propellers. Additionally, this section defines several relations which are essential for assessing the performance of propellers. The momentum theory is described in Section 2.1.1. Based on this, the blade element momentum theory is described in Section 2.1.2. Propeller performance is generally defined by a set of non-dimensionalized parameters, which are highlighted in Section 2.1.3.

### 2.1.1. MOMENTUM THEORY

Assuming inviscid, incompressible and irrotational flow, the propeller can be modeled as a single streamtube. The velocity and static pressure are uniform over each cross section of the disk and streamtube [26]. A schematic of the propeller streamtube is shown in Figure 2.3, where the stream-wise development of various parameters of the flow are given.

A propeller providing thrust will result in a total pressure jump over the propeller due to the increased momentum entered to the flow. The static pressure drops to a minimum and then discontinuously jumps to a higher static pressure behind the propeller. The stream-wise drop in pressure accelerates the flow causing the streamtube to contract, which is required to conserve continuity of the flow.

### 2.1.2. BLADE ELEMENT MOMENTUM THEORY

To understand how the performance of propellers are able to be modeled, Blade Element Momentum (BEM) theory is highlighted in this section. To properly assess the

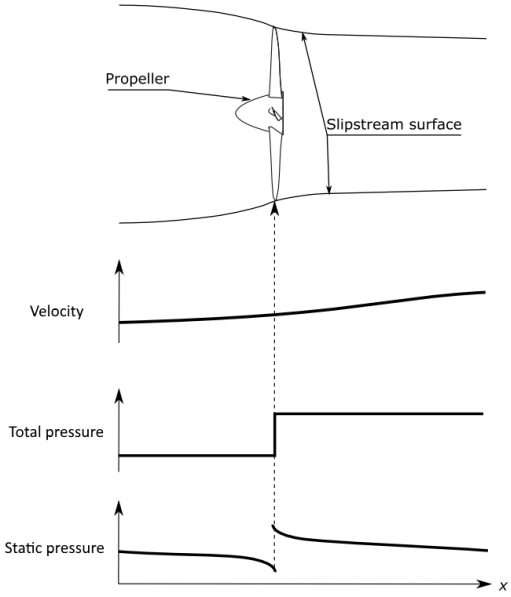


Figure 2.3: Momentum representation of velocity, total pressure and static pressure over the propeller, adapted from Marcus [7].

propeller performance, the non-uniform loading of the blade needs to be taken into account. Therefore, the previous assumptions of uniform velocity and pressure are lifted and replaced by the assumption that the slip-stream can be split up into several non-interacting annular streamtube control volumes. The flow far upstream of the propeller is still purely axial and uniform. The static pressure is assumed to be equal to the static pressure outside of the streamtube far downstream of the propeller due to the low angular velocity of the slipstream in this region [26]. The flow is still considered to be irrotational, but wake rotation is now included. In BEM theory, the complete streamtube is split in to a certain amount of annular streamtube elements. Each of these sections has its own width ($dr$) and the performance of the blade section is based on the 2-dimensional analysis of the wing section. This results in a quasi 3D approach built up by several 2D sections, for this reason 3D aerodynamic effects are not taken in to account in this analysis. Each of the sections will result in a lift and drag value which can be translated to the element wise thrust and torque of the propeller. The process of determining the lift and drag of each element is highlighted in Figure 2.4.

This figure shows the aerodynamic forces which are resulting from the combination of axial and tangential velocity flowing over-the-wing section. To obtain the lift and drag of the section, the velocity magnitude and direction is of importance. Due to the steamtube contraction as shown in Figure 2.3, an additional velocity component in the axial and tangential direction is induced. These additional velocities are defined as an factor which is multiplied to the existing rotational and axial velocities. As a consequence, these two parameters are defined as the axial and tangential induction factors ($a$, $a'$).

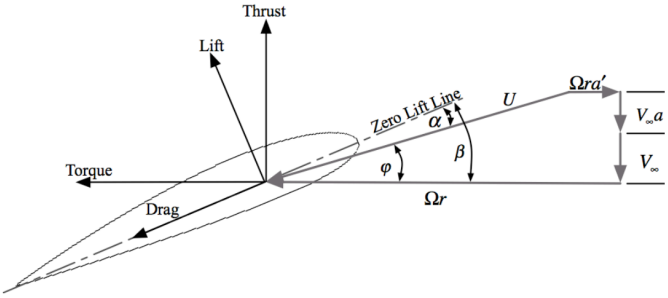


Figure 2.4: Illustration of forces and velocities on blade element, obtained from Rwigema [26].

These are themselves dependent on the generated lift and drag and therefore determination of these velocities and therefore the forces this is done iteratively. The torque and thrust of the elements can be integrated resulting in the total thrust and torque of the system. The axial and tangential velocities are equal to the combination of the initial and induced velocities as defined in Equation 2.1 and Equation 2.2.

$$V_a = V_\infty(1+a) = V_\infty + v_a \tag{2.1}$$

$$V_t = \Omega r(1-a') = \Omega r - v_t \tag{2.2}$$

The actual perceived velocity by the wing element is equal to the square root of the squared total tangential and axial velocities ($V_t$, $V_a$).

The simplifications in BEM theory do not consider vortices shed from the propeller root and tip. Similar to the wingtip vortices being generated in an aircraft wing, these too originate at the tip and root of the propeller blade. These vortices have a significant effect on the flow-field and therefore to the induced velocities experienced by the wing sections. Therefore a root and tip correction as developed by Prandtl is generally applied. This "Prandtl loss factor" reduces the induction coefficients directly. This factor is dependent on the inflow angle, the number of blades and the relative location of the wing element.

### 2.1.3. NON-DIMENSIONALIZED VARIABLES

To be able to compare results, these parameters are non-dimensionalized. The thrust can be non-dimensionalized in two ways and therefore it's important to show both definitions and distinguish the two. The thrust ($C_T$) and torque coefficients ($C_Q$) are given in Equation 2.3 and Equation 2.4 respectively. An alternative thrust coefficient ($T_c$) defined in Equation 2.5, is non-dimensionalized much like the lift coefficient is traditionally non-dimensionalized, namely by dividing the thrust force by the dynamic pressure and a reference area (in this case the propeller disk area). This alternative thrust coefficient ($T_c$) is often used when discussing the impact of the propeller on the wing, since the thrust force is non-dimensionalized similar to the lift and drag coefficient and therefore these three coefficients can be fairly compared to each other.

$$C_T = \frac{T}{\rho_\infty n_\mathrm{p}^2 D_\mathrm{p}^4} \tag{2.3}$$

$$C_Q = \frac{Q}{\rho_\infty n_\mathrm{p}^2 D_\mathrm{p}^5} \tag{2.4}$$

$$T_\mathrm{c} = \frac{T}{0.5\rho_\infty V_\infty^2 A_\mathrm{p}} \tag{2.5}$$

The power coefficient is often used in addition to the torque coefficient. The power is defined as the torque multiplied by the rotational speed of the propeller Equation 2.6. The corresponding power coefficient is defined in Equation 2.7.

$$P = \Omega Q \tag{2.6}$$

$$C_P = \frac{P}{\rho_\infty n_\mathrm{p}^3 D_\mathrm{p}^5} \tag{2.7}$$

$$P_\mathrm{c} = \frac{P}{0.5\rho_\infty V_\infty^3 A_\mathrm{p}} \tag{2.8}$$

One additional important non-dimensionalised parameter is the advance ratio. This variable is the ratio between the axial velocity and the rotational velocity as shown in Equation 2.9. The advance ratio is a very useful non-dimensional velocity, since a particular advance ratio will result in the airfoils of the blade experiencing the same non-induced angle of attack regardless of the inflow velocity.

$$J = \frac{V_\infty}{n_\mathrm{p} D_\mathrm{p}} \tag{2.9}$$

The performance of a propeller is generally assessed by determining the efficiency, which is defined in Equation 2.10. The efficiency is defined as the useful power extracted from the system divided by the power supplied to the system. The useful power is defined as the thrust multiplied with the velocity. The efficiency is alternatively defined by the advance ratio multiplied with the ratio between the thrust coefficient and the power coefficient by substituting Equation 2.3, Equation 2.7 and Equation 2.9.

$$\eta = \frac{V_\infty T}{P} = J\frac{C_T}{C_P} \tag{2.10}$$

The previously mentioned coefficients are used in presenting the propeller performance curves. These parameters are conventionally plotted against the advance ratio, to make these curves independent of inflow velocity. Typical performance curves for thrust and power coefficients are shown in Figure 2.5 and typical efficiency curves are shown Figure 2.6. By definition, the efficiency of a propeller is zero when the inflow velocity is equal to zero ($V_\infty$=0), as can be seen in Equation 2.10. This however does not mean no thrust is produced or that no power is required. At low advance ratios, the trust produced is generally highest given that the angle of attack of the blade is highest, since

increasing the $V_\infty$ only reduces the angle of attack of the blade elements, as illustrated in Figure 2.4. With this high angle of attack, also very high torque is generated, resulting in a high power requirement for achieving this thrust. Maximum efficiency is found where the ratio between thrust (and advance ratio) and power is high. Changing the blade pitch changes the local angle of attack of the blade sections and changes the thrust and torque of each of the sections. Therefore, depending on the pitch angle, the maximum efficiency of that specific blade configuration is found at a different advance ratio. Not only the "optimal" advance ratio changes with changing the blade pitch angle, also the actual maximum efficiency is affected. For an optimal propeller design, the blade pitch which results in maximum efficiency should be the able to produce the thrust required in the cruise condition.

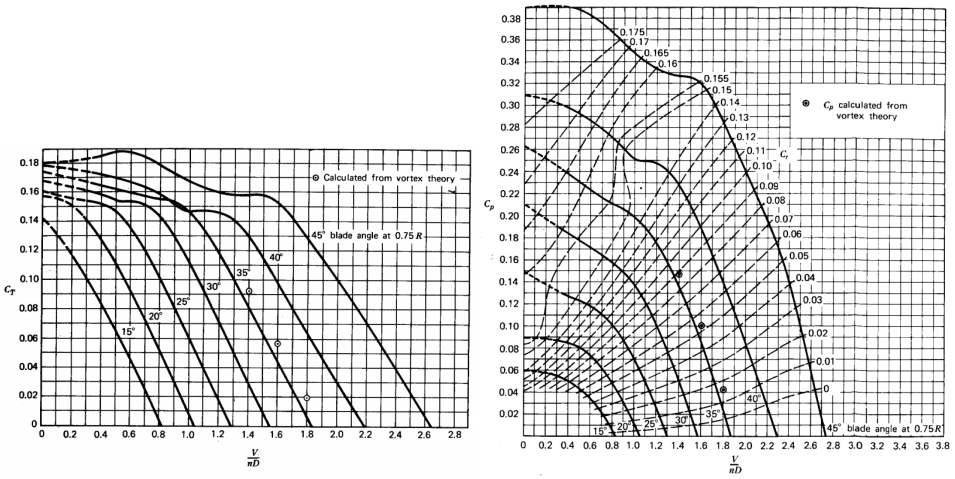


(a) Thrust coefficient

(b) Power coefficient

Figure 2.5: Typical performance curves plotted against the advance ratio at several blade pitch angles, obtained from McCormick [27].

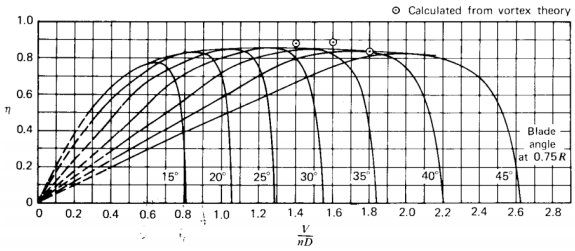


Figure 2.6: Typical efficiency curves plotted against the advance ratio at several blade pitch angles, obtained from McCormick [27].

## 2.2. OVER-THE-WING PROPELLER AERODYNAMICS

The inflow field of the propeller is affected by the wing surfaces, which in turn alters the propeller performance and slipstream. This section will highlight the aerodynamic interaction effects which affect the propeller performance. Both potential flow based interference and viscous based interference can be recognized [28]. Effects like the change in the inflow direction due to the presence of a body and effect like Boundary Layer Ingestion (BLI) can be distinguished in this way.

### 2.2.1. EFFECT OF THE WING

The inflow field of the propeller changes depending on the location of the propeller with respect to the wing. Figure 2.7a shows an example of the wing induced velocities which serve as inflow profiles for the propeller. This sketch shows a generic sketch of the flow field around the wing section where the effect of viscous effects result in a zero velocity at the surface which quickly reaches the inviscid velocity. The steady, inviscid and incompressible flow velocity at the wing is highest at the lowest point of pressure, which is located at the suction peak near the leading edge. From this point the pressure rises and the velocity drops. Therefore a lower induced velocity profile can be found at the trailing edge. The axial induced velocity decreases vertically to zero far away from the wing. The flow direction equals the contour of the wing close to the wing and due to the vertical reduction of the induced velocity the direction becomes aligned with the free-stream flow farther from the wing.

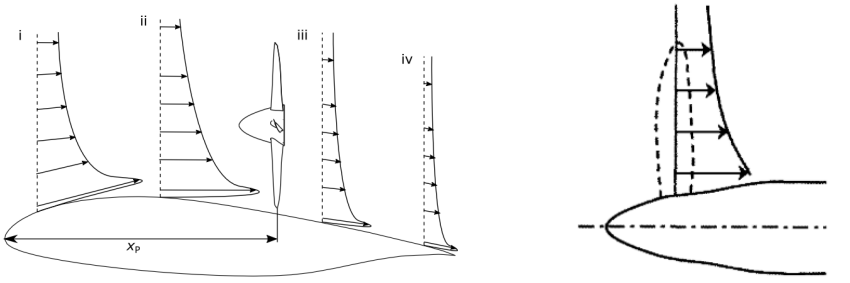


(a) Wing, obtained from Marcus [7].

(b) Nacelle, obtained from Veldhuis [18]

Figure 2.7: Axial induced velocity profiles by the wing and nacelle

CFD simulations done by Müller et al. [24] give an insight in the different phenomena associated with over-the-wing propulsion. A straight wing with a single propeller located at the mid-chord (no distributed propulsion) is investigated. The relative thrust generated by the the propeller at different locations on the disk for take-off and cruise thrust level is shown in Figure 2.8a. The impact of the induced velocity profile as previously described is clearly visible here. The additional axial velocity at the bottom of the propeller reduces the apparent pitch of the propeller blade and therefore reduces thrust. This effect is more pronounced at the bottom of the disk where the axial induced velocity is highest. Depending on the propellers inclination relative to the airfoil surface, the propeller may receive an induced angle of attack by the wing. With a positive angle of attack relative giving down going blades a higher loading and a up going blades a lower

loading as illustrated in Figure 2.8b. The additional velocity induced increases the perceived velocity by the blades and therefore blades reach supersonic speed at lower inflow mach numbers compared to propellers in a tractor configuration [24].

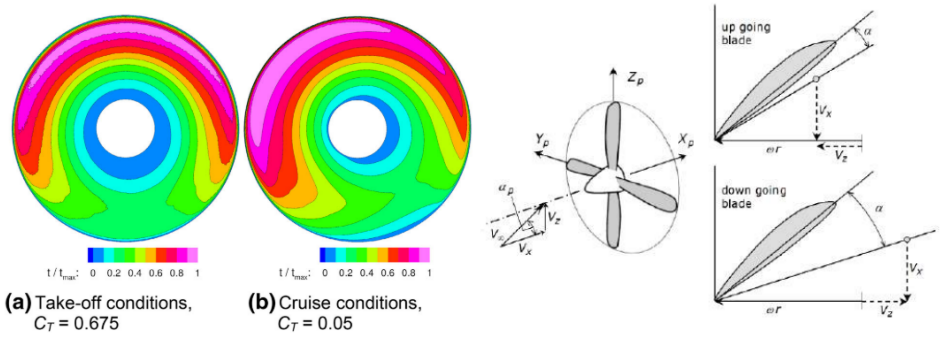


(a) Contours of relative thrust ($t/t_{max}$) as produced by the propeller, obtained from Müller et al. [24]

(b) Local variation of blade pitch angle due to a propeller angle of attack, obtained from Veldhuis [18]

Figure 2.8: Effect of inflow variations on a propeller.

The research performed by Marcus et al. [7] showed the effect of the induced axial velocity on the propeller efficiency. The different inflow fields experienced by the propeller at different axial propeller locations altered the efficiency of the propeller significantly, as shown in Figure 2.13. The greatest loss in efficiency is found at the thickest point of the airfoil ($x/c \approx 0.3$), where the wing induced flow is expected to be greatest. The amount of efficiency lost depends on the thrust setting of the propeller, where greater amounts of thrust result in lower propeller efficiency losses in the majority of the domain, with the exception of a propeller positioned close to the trailing edge. Moving away from this point, the efficiency increases which indicates a more uniform inflow field for the propeller. A propeller positioned at the trailing edge has similar performance to the isolated propeller. Effect of changing the propeller diameter was additionally investigated by Marcus et al. [7] and showed that larger diameter propellers lost more propeller efficiency at a constant excess thrust. This was tested at a propeller axial location of $x/c = 0.95$, where the wing induced velocity is relatively small.

### 2.2.2. EFFECT OF THE NACELLE

The presence of the nacelle imposes a non-uniform axial velocity distribution on to the propeller inflow field, as is illustrated in Figure 2.7b [18]. Due to the presence of the nacelle, the streamlines are curved around the nacelle, changing the local inflow angle over the blade as well as the velocity distribution. The inviscid axial velocity is increased the most at the nacelle and this increment drops of with the distance to the nacelle. This effect is not negligible and therefore should be taken into account when modeling the performance of the propeller.

### 2.2.3. DUCTED FAN PERFORMANCE

The ducted fan designs in the smaller personal jets as shown Figure 1.2 could prove beneficial to the performance of the system. Before assessing if ducting the array of fans

would be an interesting addition to the wing design, the concept should be understood. This section quickly touches upon the different concepts a ducted fan affects the aerodynamics of the system.

The axial induced velocity experienced by the propeller changes with the relative axial position of the propeller in the duct. The loss in performance due to the vortex generated at the blade end can be greatly reduced by the addition of a duct. The reduction of circulation at the tip of the blade is reduced when the gap between the shroud and the blades is small. This effect is commonly referred as the end plate effect. Smaller tip clearances are more beneficial by giving a more pronounced end plate effect, but the overall maximum efficiency, depending on mach number, might be found at different tip clearances. Interference between the duct boundary layer and the blades result in an optimal tip clearance which is slightly larger than minimal [29]. The inclusion of the duct increases the thrust, but also the power requirement, therefore ducted fans aren't more efficient for every flight condition.

An additional contribution to the thrust is the thrust generated by the duct itself. With the propeller providing thrust, the addition of momentum into the flow results in a pressure jump and therefore higher pressure behind the propeller. The inclusion of the duct radially changes the pressure distribution and the slipstream contraction location and development, as can be seen in Figure 2.9. As seen in the figure, the contraction can only happen outside of the duct. The contraction at the duct entry results in a effective angle of attack on the duct resulting in lower pressure at the leading edge. Duct thrust is highly dependent on the slipstream contraction and therefore the duct thrust is greater at higher blade loading at low advance ratios. Aircraft relying on Short Take-Off and Landing (STOL) like the Lilium jet (Figure 1.2) are therefore able to benefit from the additional efficiency gained by the duct. Whereas in cruise performance, the additional viscous drag more likely outweighs the smaller benefit of the lightly loaded propeller.

Research done by Black et al. [29] investigated the effect of different area ratios on the ducted propeller performance for several power loadings and mach numbers from 0 to 0.5. The area ratio is defined as the ratio between the area at the propeller location divided by the duct exit area. With large slipstream contraction at high loading, greater area ratios are desirable. At higher Mach numbers, lower area ratios significantly perform better. For this reason, when designing ducts, a compromise is involved at the area ratio selection of the duct [29].

### 2.2.4. SHROUD INTERACTION EFFECTS

Implementing a shroud around the duct as proposed in the HS3 concept by TUDelft could, as described by Hoogreef et al. [10] be beneficial to the efficiency and the noise shielding. An illustration of the propulsive empennage serial hybrid (HS3) concept is shown in Figure 2.10. Some beneficial effects like the periodically reduced tip losses and more uniform inflow could be achieved with the addition of the shroud. The effectiveness of the end plate effect will be reduced, but so will the additional viscous drag be compared to a fully ducted design. The effect of the secondary wing above the propeller has been previously investigated by Veldhuis and Khajehzadeh [31]. The presence of a secondary wing is said to be able to majorly improve the aerodynamic characteristics. A local reduction of inflow could be realized by the addition of the secondary wing, therefore increasing the propeller efficiency. The work of Veldhuis and Khajehzadeh did not

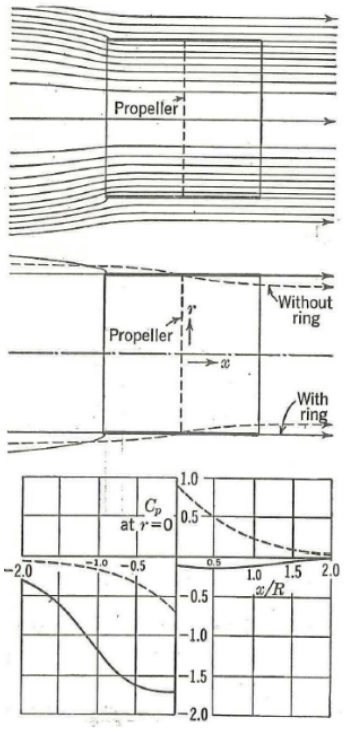


Figure 2.9: Development of the streamlines, slipstream contraction and pressure coefficient over the axial position. The isolated propeller (dashed lines) is compared to the ducted propeller (solid lines) in the bottom two figures, obtained from Küchemann [30].

include an optimization where all of the design variables are varied at once and constant lift and thrust have not been enforced. Therefore, the effect of the addition of the secondary wing could be further investigated and explored.

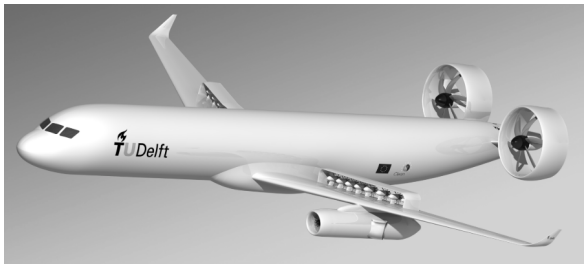


Figure 2.10: Propulsive empennage serial hybrid (HS3) concept aircraft [10]

A recent master thesis performed by Mourão Bento [32] investigated the fundamental aerodynamic effects of an square duct by performing Computational Fluid Dynamics (CFD) simulations. With the shroud concept described by Hoogreef et al. [10] these

aerodynamic effects might occur in the most in- and outboard propellers in the shroud. In a square duct, the blade loading would vary along the rotation, since the axial velocity profile of the duct is non-uniform [32]. Larger induced velocities on the blade were found at azimuthal locations where the tip clearance is smallest, such that the blade is closest to the duct. The average axial velocity in a square duct was found to be lower when compared to a circular duct [32]. Thrust produced by the circular duct was considerably larger than the circular duct when tested at the same advance ratio. The square duct tested by Mourão Bento however was not optimal and showed separation and vortex generation in the corners of the square duct. Unsteady simulations at a constant advance ratio of $J = 0.7$ showed that the square ducted propeller was the least efficient system, since the efficiency was 4.5% lower when compared to a circular ducted propeller [32].

## 2.3. IMPACT OF PROPELLER ON WING PERFORMANCE IN OVER-THE-WING CONFIGURATIONS

The propeller close to the wing has significant effects on the pressure distribution and therefore the lift and drag of the wing. The experiment performed by de Vries et al. [20] provides insight into the effect which the propeller has on the wing. By implementing pressure taps on the wing, the induced pressure coefficient of the propeller can be measured, as is shown in Figure 2.11. Both the effect on a flat plate and on a hinged airfoil are analyzed. As can be seen from the flat plate result in Figure 2.11a, the propeller induces an favorable pressure gradient up to a region close to the propeller and from a region behind the propeller. The size of this region and the amplitude of the pressure gradient depends on the thrust setting. In the region close to the propeller a severe adverse pressure gradient is found. This effect can be well explained by the basic momentum theory explained in Section 2.1.1 where Figure 2.3 shows the same favorable pressure gradient behavior. Due to the assumption that the propeller disk is of small thickness, this discontinuous pressure jump is not realistic. Therefore, a quick rise in static pressure is found instead. For design purposes, it is important to notice the negative effect of the induced adverse pressure gradient. This induced adverse pressure gradient promotes separation and in combination with an already existing pressure gradient as shown in Figure 2.11b, the combined effect results in a very severe adverse pressure gradient which provokes separation in the case where the propeller is placed at the hinge location [20]. With careful placement however, the induced favorable pressure gradient can be used for improved separation characteristics. By for example placing the propeller 0.5R upstream of the hinge location, the favorable pressure gradient in combination with the re-energized and smaller boundary layer result in a more attached flow on the flap surface as shown in Figure 2.12.

Unsteady propeller effects also play a role in the possible induced separation. The tip vortices shed from the propeller generate a negative vorticity which in turn reduces the velocity below the particular vortex. Therefore, the vortex induces periodically reduced axial velocity which in turn promotes separation. When moving the propeller half a radius upstream as seen in Figure 2.12, the vortices are dissipated in the boundary layer and do not contribute significantly to the promotion of separation, the aforementioned favorable pressure gradient can be seen to have a positive effect and increases the veloc-

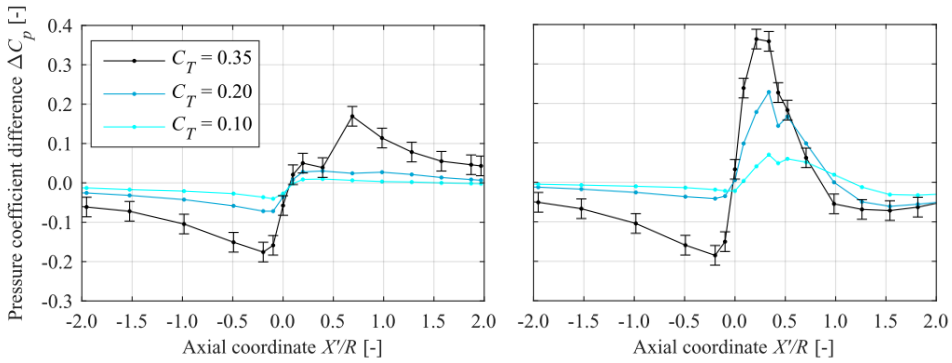


(a) Flat plate configuration

(b) Flapped wing configuration

Figure 2.11: Change in pressure coefficient on the wing due to the influence of an over-the-wing propeller at various thrust coefficients, obtained from de Vries et al. [20].

ity over the flap.

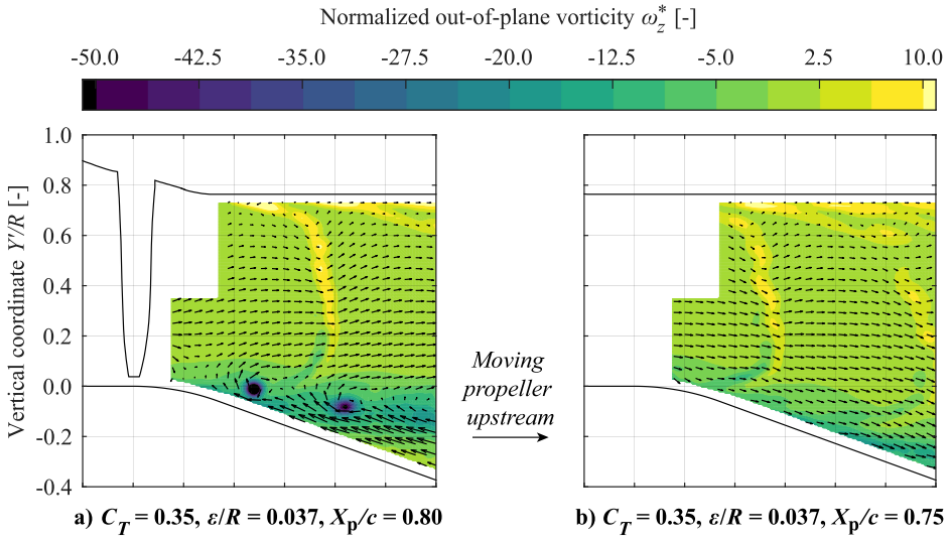


Figure 2.12: Phase-averaged vorticity contours of the flow-field, the velocity vectors represent the in-plane propeller induced velocities ($U_\infty$=20 m/s, $\epsilon/R$= 0.037, $C_T$=0.35), obtained from de Vries et al. [20].

### 2.3.1. EFFECT OF THE CHORD-WISE PROPELLER LOCATION

Proper propeller placement can use the propeller induced aerodynamic effects to increase high-lift and cruise conditions. Several investigations on the possible over-the-wing lift and drag benefits with respect to propeller position have been carried out [5–7, 22, 24, 25, 31, 33]. The greatest reduction in pressure drag is found by placing the pro-

peller at the thickest part of the airfoil [7]. In this way, the lower static pressure in front of the propeller and the higher static pressure behind the propeller result a negative pressure drag.

Due to the variety of different thrust levels and relative propellers sizes of these reports, this section will focus on propellers sized for distributed propulsive applications. Experimental investigation done by Marcus et al. [7] showed that alterations in the boundary layer transition location is minimal and that placing an propeller just in front of the point of transition resulted in earlier transition. This was due to the previously mentioned adverse pressure gradient close to the propeller and the interaction between the tip vortices and the boundary layer.

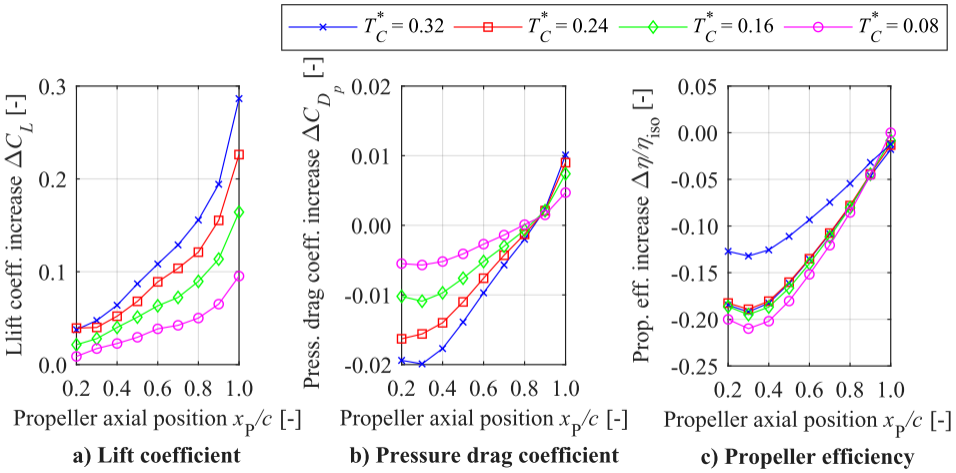


Figure 2.13: The effect of changing the axial position of the propeller on the lift coefficient (a), pressure drag coefficient (b) and the propeller efficiency (c) at constant thrust settings. the pressure drag and propeller efficiency are evaluated at constant lift coefficient ($C_L$=0.5), obtained from Marcus et al. [7].

The variation of chord-wise propeller location has also been experimentally investigated by Marcus et al. [7]. The effect on the lift coefficient, pressure drag coefficient and the propeller efficiency is shown in Figure 2.13. Marcus found an increase of lift coefficient by moving the propeller further aft, this due to a larger portion of the airfoil experiencing the increased suction induced by the propeller. Pressure drag reaches a minimum around $0.3c$ which is close to the maximum point of thickness. When the propeller is placed at approximately $0.9c$, the propeller thrust setting has minimal effect on the pressure drag coefficient and the pressure changes behind and in front of this point scale equally. The propeller efficiency, on the other hand, tends to rise when moving away from the thickest point of the airfoil. This behavior agrees with the previous analysis made in Section 2.3 where the increase in axial velocity by the wing on the propeller reduces the efficiency of the propeller. Therefore, for the sake of best efficiency and lift, the best location is closest to the trailing edge, while the pressure drag is lowest at the thickest point of the airfoil.

# II

# Method

# 3

# NUMERICAL SET-UP

Central to the research is the method of the aerodynamic system performance estimation. This study uses a numerical model to have the freedom of evaluating a large number of different geometrical designs, which is often more time-consuming to do experimentally. Several numerical models are available and previous studies on OTW propulsive aerodynamics have used a variety of numerical models. Lower order models as the one used in [7] employs a panel method and a BEM in combination with a vortex lattice method to model the wing and propeller aerodynamics. Other studies perform a steady RANS CFD simulation, which can be modeled inviscid as in the research by Khajehzadeh [33] or include viscous modeling as in Müller et al. [6]. Unsteady RANS simulations are also used in a study by Müller and Friedrichs [22]. Higher order models are like Eddy Viscosity Models (EVM) are applied when small scale aerodynamic effects like boundary layer interaction are key in the analysis, like in the study performed by Sören [21]. The choice in this research is made to employ a viscous compressible RANS CFD simulation. The viscous effects are included to obtain a more accurate depiction of the impact of design changes trends on the total drag and therefore system efficiency. Given the number of design variables taken into this account in this study, computational effort is a parameter to be kept in mind.

Numerical propeller modeling where propeller-wing interaction plays a role are traditionally performed by either lower order BEM [6, 7, 33] simulations or are simulated using CFD models [21, 34]. The response of the propeller to the non-uniform inflow field as induced by the wing surfaces critically needs to be captured. This model uses a engineering method developed by van Arnhem et al. [34], using existing isolated propeller RANS CFD simulations to create a solution for an arbitrary non-uniform inflow field. This method is significantly more computationally inexpensive than performing a full-blade RANS simulation, while still obtaining acceptable agreement with full-blade and experimental results [34].

## 3.1. COMPUTATIONAL FRAMEWORK

Central to the method applied in this work is the framework written automating the numerical calculations. Due to the nature of this study, automation of the system performance estimation is a requirement due to the number of design evaluations. Obtaining the aerodynamic performance of the system requires several different programs to be called with each their own sub processes. The main task of the framework is to connect

all sub-processes. The challenge in this is to connect these sub-processes in a robust manner for all of the possible designs to be evaluated. The Python (v3.6) programming language is used to write the main framework.

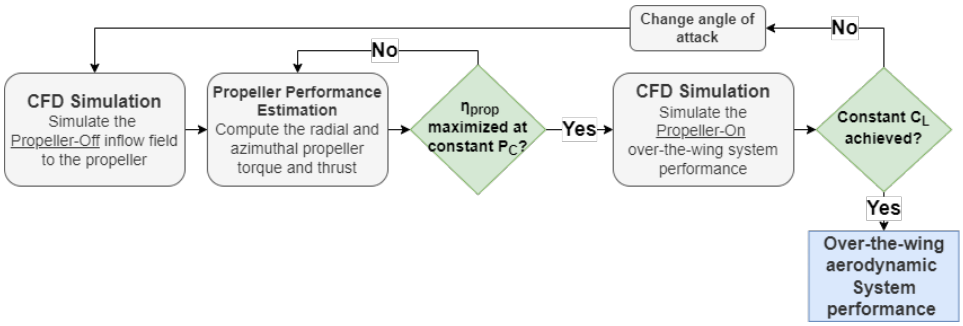


Figure 3.1: Flowchart to achieve the Over-the-wing aerodynamic System performance

The global workflow of the numerical model is shown in Figure 3.1 and shows the path towards simulating the performance of an OTW geometry. One simulation loop includes two CFD simulations and one propeller performance estimation. For a fair comparison of designs, all designs are to be evaluated at a constant lift coefficient. This constant lift coefficient is found by running at least three iterations at a different angle of attack, this new angle of attack is selected to more closely match the desired lift coefficient. From previous iterations, the $C_L$ - $\alpha$ slope is estimated and the angle of attack for the upcoming iteration is derived from this assumed linear relation. This process is iterated upon until the lift coefficient is within 1% of the desired lift coefficient, but generally after the third iteration (which now has the $C_L$ - $\alpha$ slope computed from the first two iterations) the lift coefficient is converged somewhere in the range of 1e-5. When the simulation is not found to be converged, the simulation is re-run on the same mesh with adjusted boundary conditions for the new angle of attack. When the simulation is converged, the previous two simulation results are linearly interpolated to obtain the performance at the specific required lift coefficient to make sure the lift coefficient exactly matches the targeted lift coefficient. This interpolation is performed to have a more accurate and fair comparison of different designs, since this 1% tolerance in lift coefficient can still be larger than any sensitivities found when changing designs. Every design is evaluated at at least three different angles of attack to obtain the lift slope curve which is used for the interpolation of results. The angle of attack for this desired lift coefficient is unknown at the start of the simulation and dependent on the specific design and propeller power setting. Therefore the angle of attack is estimated by using previous iterations if available.

The propeller performance estimation critically includes the estimation of the effect of a non-uniform inflow. Therefore, before estimating the performance of the propeller in the configuration, the inflow field needs to be simulated in the first "propeller-off" CFD simulation. The obtained inflow field is loaded back into the Python framework and prepared to be used as input for the propeller load distribution estimation. The performance of the propeller is estimated by an engineering method created by van Arnhem

et al. [34] able accurately to estimate the propeller performance in a non-uniform inflow at a relatively low computational cost. This engineering method is expanded with an optimizer which finds the maximum propulsive efficiency $\eta_p$ of the propeller at a constant propeller shaft power coefficient $P_C$ by varying the propeller pitch and advance ratio. The propeller performance estimation method is further described in Section 3.5. The propeller thrust and torque distribution is then added into the Fluent CFD solution by adding source terms into the flow through an actuator disk model, as further described in Section 3.5.4. The second "Propeller-on" CFD computation is performed with the inclusion of this actuator disk, which results in the OTW system performance.

## 3.2. GEOMETRICAL SET-UP

A flowchart of the geometry creation process can be found in Figure 3.2. Setting up the CFD simulation starts out with creating the geometry files and fluid domain. The geometry modeled in this research contains a segment of an un-swept un-tapered wing featuring a single OTW propeller. Initial geometry creation commences with the build up of a 2D geometry in Python. Both the wing and shroud airfoil can be parameterized by either using a Class-Shape-Transformation (CST) parametrization method [35] or using NACA-4 or NACA-5 digit airfoil specification. The parametrization method used to describe the shape of the airfoil has a significant role in the system design and optimization. The aim is to have the freedom to explore as many different design alternatives as possible while keeping the number of design variables to a minimum [36]. The NACA airfoil parametrization method is very useful in the sense that it only requires a very small amount parameters to describe a variety of well performing airfoil shapes. In this research however, a higher degree of freedom is required for the airfoil design. This is because the propeller locally impacts the performance of the wing and therefore local change of the airfoil design might result in superior performance. The CST method is selected for the ability to achieve a good approximation of an existing airfoil shape with an acceptably low number of variables [36].

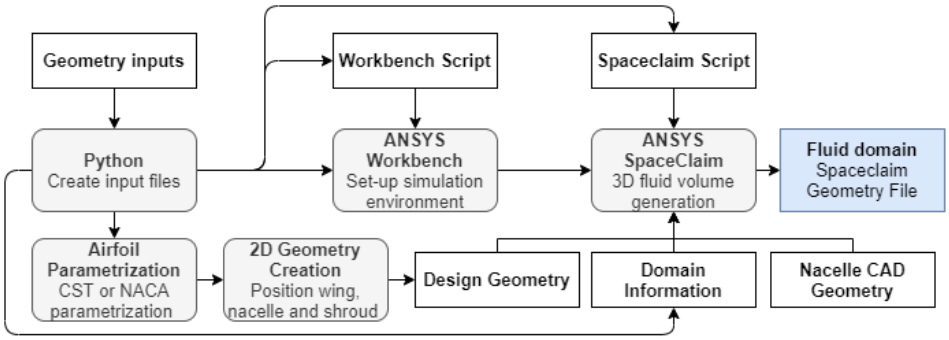


Figure 3.2: Geometry Creation Flowchart

The main wing airfoil shape is parameterized using the Class/Shape function Transformation (CST) as proposed by Kulfan and Bussoletti [35]. This method allows airfoil geometry to be defined with a varying amount of design variables depending on

the amount of control and design freedom requested. The method [35] represents the two dimensional geometry as a product of a class function $C(x/c)$ and a shape function $S(x/c)$. The class function defines the type of geometry to be represented, which in this case is an airfoil. The class function is defined in Equation 3.1, where $N_1$ and $N_2$ are 0.5 and 1.0 respectively in the case of an airfoil geometry [37].

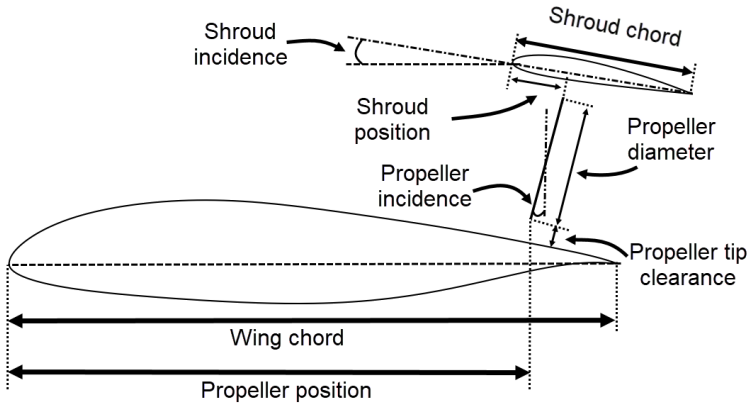


Figure 3.3: Geometrical representation of design parameters

$$C\left(\frac{x}{c}\right) = \left(\frac{x}{c}\right)^{N_1}\left[1-\frac{x}{c}\right]^{N_2} \quad \text{for} \quad 0 \leq \frac{x}{c} \leq 1 \tag{3.1}$$

The shape function selected uses a weighted sum of Bernstein polynomials is selected by Kulfan and Bussoletti [35]. This shape function is defined in Equation 3.2, where the weight factors are stored in the array $b_i$.

$$S\left(\frac{x}{c}\right) = \sum_{i=0}^{n}\left[b_i \cdot K_{i,n} \cdot \left(\frac{x}{c}\right)^i \cdot \left(1-\frac{x}{c}\right)^{n-i}\right] \quad \text{with} \quad K_{i,n} = \frac{n!}{i!(n-i)!} \tag{3.2}$$

These weight factors are the parameters which the user changes to build the airfoil. In the 2D airfoil shape the relative vertical location of the airfoil can be calculated with Equation 3.3, where the last term $\Delta z_{te}$ defines the thickness of the trailing edge. In this study, the trailing edge height is set equal to 0 mm. In a later stage of geometry creation, the trailing edge is cut-off to improve mesh quality.

$$\frac{y}{c} = C\left(\frac{x}{c}\right) \cdot S\left(\frac{x}{c}\right) + \frac{x}{c}\frac{\Delta z_{te}}{c} \tag{3.3}$$

A sketch of the geometrical build-up of the model is shown in Figure 3.3. This two dimensional geometry is modeled as an infinite wing and features a shroud above the propeller. The model is built up by first defining the main wing chord. The propeller is positioned relative to the main wing chord line and therefore the axial propeller position is defined as $x_p/c$. The model is build up defining the propeller axial propeller position

as the main chord projected the position of the lower tip of the propeller as shown in Figure 3.3. Therefore changing just the propeller inclination will move the location of the propeller center. The propeller tip clearance is defined as the distance from the propeller tip to the wing surface in the propeller plane. The shroud is positioned relative to the upper propeller tip location. The shroud location is defined by the location of the propeller tip orthogonal projected location on the shroud chord. The shroud incidence is defined relative to the wing incidence. The wing geometry is based on the NLF-MOD22B designed by Boermans at Delft University of Technology [38], where this specific wing design previously has been used in research by Marcus [7]. The NLF-MOD22B is simplified using a set of CST coefficients allowing for easy adaptation of the wing geometry. The CST coefficients used in the majority of the research are shown in Table 3.1. The top surface of the airfoil is defined by 8 coefficients and the lower surface by 6 coefficients. The values of these coefficients are found by running a least-squares optimization routine on the original coordinates.

Table 3.1: Wing CST coefficients recreating the NLF-MOD22B airfoil [38]

| | | | | | | | | |
|---|---|---|---|---|---|---|---|---|
| CST upper | 0.2151 | 0.3523 | 0.1159 | 0.5660 | -0.1068 | 0.5291 | 0.0529 | 0.3854 |
| CST lower | -0.1376 | -0.1386 | -0.1268 | -0.2369 | -0.3014 | 0.1495 | | |

A summary of the baseline geometrical parameters is given in Table 3.2, where the shroud features a NACA 2412 profile. The propeller selected is the XPROP-S, which previously has been used in previous propeller interaction studies [34, 39–41]. The nacelle used in this study is featured in the experimental study performed by de Vries et al. [20] and is visualized in Figure 3.5b. A downstream propeller chord-wise position is selected based upon previous research [7, 21], observing higher propeller efficiencies and allowing for potential beneficial thrust vectoring capabilities benefiting take-off conditions.

After individual airfoil generation of the main wing and shroud, the complete geometry is build from positioning the two wings relative to the propeller location, resulting in the finalized 2D geometry as illustrated in Figure 3.4a. The XProp-S propeller is selected for this research based on the amount of recent relevant studies performed with this propeller [20, 34]. This propeller is a scaled model of a conventional propeller of a typical regional turboprop aircraft [42]. Several propeller-wing interaction studies [20, 21, 34, 42] have used this propeller resulting in the ability to select validation cases for this research. This propeller features six bladed and a propeller diameter $D_p$ of 0.2032 m and features a variable pitch. The pitch is generally set to 45 degrees at 70% of the propeller radius in several research projects to achieve high thrust and torque coefficients at relatively high advance ratios, which represent cruise conditions of a full-scale aircraft [34]. The propeller is equipped with airfoil sections from the Clark-Y family. The propeller blade radial chord and pitch distribution is shown in Figure 3.5a. A nacelle is included in this research to capture the effect the nacelle has on the wing and on the propeller inflow-field. Additionally, varying design variables like the propeller incidence angle and the axial position of the propeller have an effect on the aerodynamic performance of the nacelle itself. Therefore, when varying these parameters it's important to include these effects, since these contribute to the total system efficiency. It must be noted that this nacelle would not be representative as used in a full-scale aircraft because of the large

Table 3.2: Geometrical specification of the of baseline OTW configuration

| Variable | Parameter | Value |
|---|---|---|
| **Wing** | | |
| Airfoil | | NLF-MOD22B |
| Chord length | $c$ | 0.84 m |
| **Shroud** | | |
| Airfoil | | NACA 2412 |
| Chord length | $c_{\text{shroud}}/c$ | 0.3 |
| Incidence | $i_{\text{shroud}}$ | 5.0 deg |
| Position relative to propeller tip | $x_{\text{p}}/c_{\text{shroud}}$ | 0.3 |
| **Propeller** | | |
| Propeller | | XPROP-S |
| Inclination | $i_{\text{p}}$ | 0.0 deg |
| Diameter | $D_{\text{p}}$ | 0.2032 |
| Tip clearances | $\epsilon/D_{\text{p}}$ | 0.14 |
| Position relative to wing | $x_{\text{p}}/c$ | 0.85 |

relative size of the selected nacelle given its size is based on the geometry as used in previous experimental investigations [20]. This opens up the opportunity of more representative experimental validation of the results obtained in this study. Nacelle friction drag is likely overestimated as a result of its current size and the pressurization of the wing and shroud experience following the introduction of this nacelle will be larger, but the effect this nacelle has on changing the propeller inflow field is not expected to be significant.

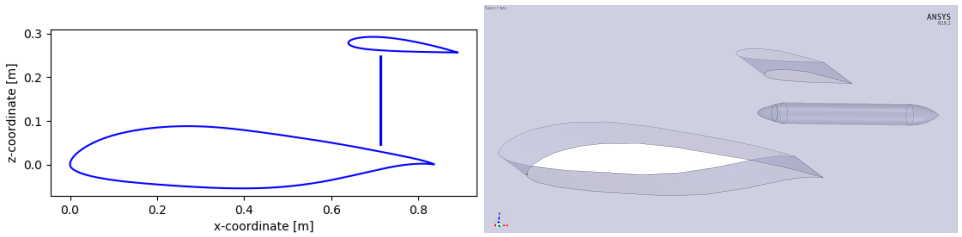


(a) Python geometry after parameterization and positioning

(b) Finalized Spaceclaim geometry

Figure 3.4: Illustration of different stages in geometry creation

With the geometry defined, it is written to files to be read by the SpaceClaim Computer Aided Design (CAD) program. Geometry generation has to be performed autonomous and SpaceClaim gives the option to write a geometry creation script in the IronPython language (version 2.7). Spaceclaim is called though the ANSYS Workbench program, which itself is called in batch mode by passing a ANSYS Workbench script. The ANSYS Workbench follows this script and builds a geometry creation object and runs IronPython SpaceClaim script. The ANSYS Workbench step is required, since SpaceClaim

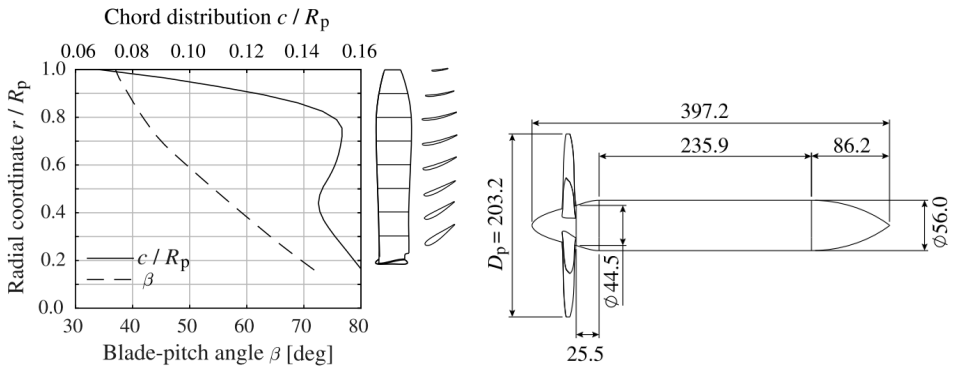


(a) Propeller pitch and chord distribution ($\beta$ = 45 deg)

(b) Nacelle dimensions in mm

Figure 3.5: XPROP-S propeller and nacelle geometry [34]

cannot be called in batch mode directly. SpaceClaim starts by loading geometry and domain information. Both airfoil profiles are loaded in as curves and converted to 3D wings. The propeller nacelle is saved as a cleaned up SpaceClaim CAD geometry file and can be loaded into the domain directly. The nacelle is then positioned according to the geometry layout specification. The next step is creating the fluid domain which is a rectangular domain enclosing the aerodynamic surfaces. The domain boundaries of the finalized fluid domain are named as separate "named selections" such that the Fluent solver has information on which of the surfaces have a boundary condition specified. The fluid domain is exported as .scdoc file which can subsequently be loaded into the volumetric grid generation performed in Fluent Meshing. An illustration of the finalized 3D geometry built up in SpaceClaim is shown in Figure 3.4b

## 3.3. MESHING PROCEDURE

Meshing is an essential step in a CFD computation. The fluid volume is discretized in several smaller volumes where the governing equations are iterated. The local volume size defines the minimum size of the flow phenomena that can be captured in the simulation. The quality and size of the mesh govern the discretisation error, which affects the quality of the results. The type of mesh generated in CFD generally falls in either three categories: a structured, unstructured or hybrid grid. Flexibility is a key point in mesh generation since a range of different geometry configurations are to be evaluated. Robustness of the mesher to generate sufficiently qualitative mesh is key in this research, since all grids are to be generated autonomously. These two factors rule out the creation of fully structured grids, since these grids have a likeliness to fail when the geometry presented differs to much from the baseline geometry. However, structured grids do pose some advantages when it comes to computational effort and accuracy [43]. A hybrid grid is used in this research to obtain the required flexibility, while potentially minimizing discretisation errors at the aerodynamic surfaces by adding a structured inflation layer, represented as a set of prism cells. The inflation layers make sure volume cell normals are aligned with the surface normals and allow for greater control at the no-slip

wall boundary surfaces. The ANSYS Fluent Mesher has an option to mesh the majority of the fluid domain with sets of hexahedral cells, which reduces computational solving time [44]. The domain where the hexahedral cells and the prism layer meet are filled up with set of a unstructured polyhedral cells.

### 3.3.1. MESHING IMPLEMENTATION

A flowchart of the general meshing procedure can be found in Figure 3.6. Fluent Meshing is called in batch mode with the use of a journal file. This journal file describes all actions the program needs to take in the Scheme programming language. Virtually all actions available in the Fluent Graphical User Interface (GUI) have a equivalent Text User Interface (TUI) command. These TUI commands are generated through Python according to the defined mesh inputs. The meshing procedure starts with the importing of the fluid geometry created by SpaceClaim. Additional geometries (bodies of influence) which are used to define local refinement are subsequently created. With all of the geometries created and defined, the surface refinement level on each aerodynamic device is defined together with the local refinement level present inside each of the bodies of influence. With this information, the a surface mesh onto the aerodynamic surfaces and boundaries is created. The skewness of the surface mesh is subsequently smoothed such that the maximum skewness of the surface mesh does not exceed 0.5. After making sure that the quality of this mesh is sufficient, the volume mesh is created. A maximum inverse orthogonal quality 0.75 is assured, such that the quality of each generated mesh is sufficient. After scaling the mesh to meters, this mesh is exported to be used in the flow solver.

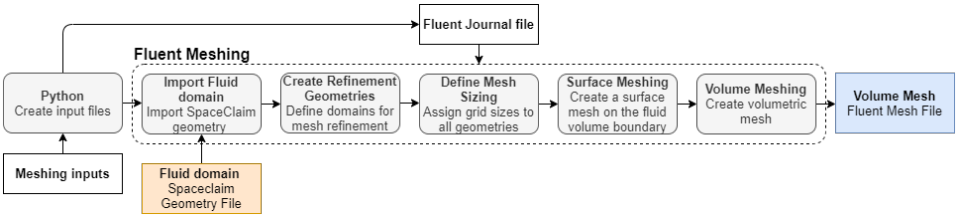


Figure 3.6: CFD meshing procedure in ANSYS FLUENT

### 3.3.2. LOCAL REFINEMENT

Local refinement of the mesh is applied to increase the solution stability and to make sure all relevant flow variables are captured smoothly, while limiting computational effort. High pressure gradients are expected to be found in proximity of the aerodynamic surfaces and the actuator disk location. Fluent Meshing allows the creation of cylindrical and rectangular boxes, which can be used for refinement zones. Several rectangular boxes are placed in proximity of the airfoil to capture the pressure gradients. These boxes increase in size and reduce in level of refinement respectively, such that the size change of mesh size is gradual. An illustration of the mesh can be found in Figure 3.7

The smallest refinement boxes have a refinement level close to the final prism layer mesh size to make sure the transition between the two structured meshes does not come

with large changes in cell volume. The second set of refinement boxes are placed in the wing wake, which make sure the viscous total pressure loss is captured. The trailing edges of the wing have a very small, but finite height and to improve the mesh in this region, several cylindrical refinement bodies are created in this region. Cylindrical refinement bodies are placed around the nacelle to make sure the pressure gradients are captured and to uphold the mesh quality in the transition region between the structured mesh regions. A second set of cylinders with a relatively high level of refinement are placed at the actuator disk. The addition of momentum though the source terms is applied in a relatively small region in the flow, which produces a large pressure gradient. The fine mesh at the actuator disk is required for solver stability and is needed to properly capture the impact the actuator disk has on the aerodynamic surfaces.

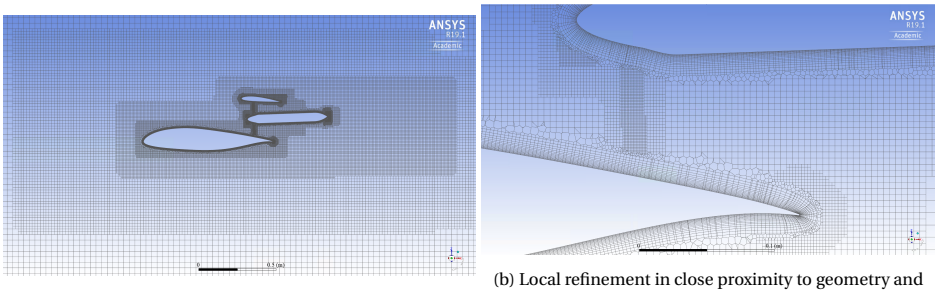


(a) Larger scale wake and pressure gradient refinement

(b) Local refinement in close proximity to geometry and actuator disk

Figure 3.7: Visualization of meshed domain

A set of prism layers is added to the geometry boundaries. The wall function employed in the turbulence model requires a minimum $y^+$ at the aerodynamic surfaces to get a reasonable drag prediction. To get a properly locally aligned mesh around the aerodynamic surfaces, a prism layer is inflated from the aerodynamic surfaces. The initial cell height of this structured mesh is such that the $y^+$, as defined in Equation 3.4, is aimed to be around 30 following the guidelines presented in the ANSYS Fluent manual. This value is recommend to have a cell inside the log-law layer ($30 < y^+ < 300$), such that the viscous sub-layer and buffer layer are modeled completely by the wall function in the cell nearest to the geometry surface.

$$y^+ = \frac{y_{\text{cell}}\mu}{\rho u_*} \tag{3.4}$$

The first layer cell height $y_{\text{cell}}$ is estimated by computing the friction velocity $u_*$ from Equation 3.5.

$$u_* = \sqrt{\frac{\tau_w}{\rho}} \tag{3.5}$$

The wall shear stress is defined in Equation 3.6 and the skin friction coefficient is estimated by Equation 3.7 [45]

$$\tau_w = 0.5 C_f \rho V_\infty^2 \tag{3.6}$$

$$C_f = \left(2\log_{10}(Re) - 0.65\right)^{-2.3} \tag{3.7}$$

Where the Reynolds $Re$ number is defined in Equation 3.8, where $l$ is the typical length scale of the geometry and $\mu$ is the dynamic viscosity of the fluid.

$$Re = \frac{\rho V_\infty l}{\mu} \tag{3.8}$$

The first layer cell height $y_{\text{cell}}$ selected for this study equals 0.26 mm. The number of prism cells is chosen such that the boundary layer is generally fully captured with the prism layer cells. This comes down to 16 layers for the main wing and nacelle and 8 layers on the shroud.

## 3.4. CFD SOLUTION

This section will provide a description on the set-up of the CFD simulations ran in this research and provide background on the governing equations.

### 3.4.1. COMPUTATIONAL IMPLEMENTATION

The simulations run through ANSYS Fluent are described in this section. The first CFD simulation is run without the propeller modeled. The steps made in this propeller-off simulation are shown in Figure 3.8. With the mesh file generated as described in Section 3.3, the Fluent solving module is called in batch mode with the use of a journal file written with Python. The solution environment is set-up by defining boundary conditions, initial conditions, discretisation schemes, relaxation factors, stopping criterion and custom field functions. The set-up of the solution is further described in Section 3.4.3. After solving the solution, output data for the "propeller-off" CFD simulation is computed and exported. This output data includes the mesh and simulation files, which are later picked up by the second "propeller-on" CFD simulation. The second chunk of output data includes forces and moment on each of the bodies as well as velocity and pressure fields later used to analyze and compare designs. Lastly, the inflow field of the propeller is defined and the velocity components are exported to a file. This file is subsequently picked up by python and prepared as input for the propeller performance estimation.

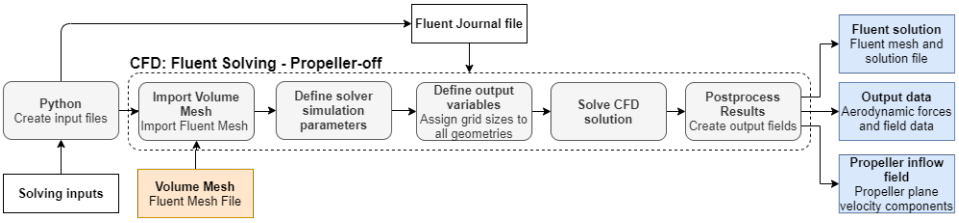


Figure 3.8: Propeller-off CFD simulation flowchart

The second CFD simulation includes modeling of the propeller into the domain. The simulation largely follows the same procedure as the first CFD simulation and the

flowchart is shown in Figure 3.9. The previous mesh and simulation is imported and the actuator disk model is defined by the use of a User-Defined Function (UDF). This function allows the user to perform custom actions which are defined by a script written in the C language. The actuator disk model is further described in Section 3.5.4. After setting up this model, the solution is initialized again and solved. Again a set of forces, moments, pressure and velocity fields are exported which now represent the propeller-on solution.

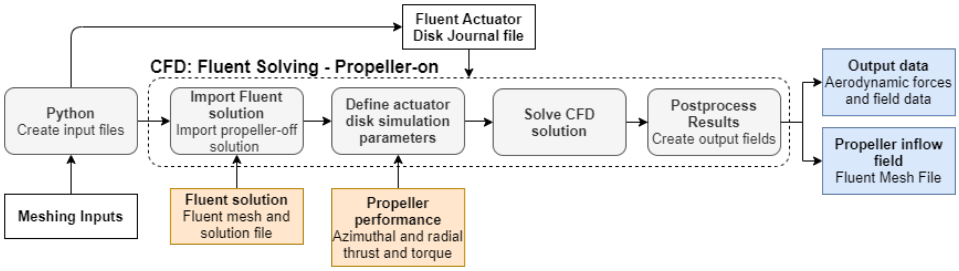


Figure 3.9: Propeller-on CFD simulation flowchart

### 3.4.2. GOVERNING EQUATIONS

This section states the fundamental equations used in the RANS CFD simulation. The software package ANSYS Fluent 19.1 is used for the numerical simulation [44]. The aerodynamic analysis is based on the fundamental equations describing the conservation of mass, momentum and energy equations as listed in Equation 3.9, Equation 3.10 and Equation 3.11. The fluid density is defined by $\rho$, velocity components by $u_{i,j}$, pressure by $p$, spatial coordinates by $x_{i,j}$, time by $t$, the body forces are denoted by $f_j$, the stress tensor is denoted by $\tau_{i,j}$ and $E$ is the total energy.

$$\frac{\delta \rho}{\delta t} + \frac{\delta(\rho u_j)}{\delta x_i} = 0 \tag{3.9}$$

$$\frac{\delta(\rho u_j)}{\delta t} + \frac{\delta(\rho u_i u_j)}{\delta x_i} = -\frac{\delta p}{\delta x_j} + \frac{\delta \tau_{ij}}{\delta x_i} + \rho f_j \tag{3.10}$$

$$\frac{\delta(\rho E)}{\delta t} + \frac{\delta(\rho u_i E)}{\delta x_i} = -\frac{\delta u_i p}{\delta x_i} + \frac{\delta u_i \tau_{ij}}{\delta x_i} + u_i \rho f_j \tag{3.11}$$

The RANS method used in this simulation solve a set of time-averaged, isothermal, compressible and viscous form of the Navier-Stokes equations. By decomposing the velocity component by a mean and fluctuating part as shown in Equation 3.12.

$$u_i = \langle u_i \rangle + u_i' \tag{3.12}$$

Substituting this into the conservation of mass and momentum equations leads to Equation 3.13 and Equation 3.14 respectively.

$$\frac{\delta \rho}{\delta t} + \frac{\delta \rho \langle u_i \rangle}{\delta x_i} = 0 \tag{3.13}$$

$$\frac{\delta(\rho\langle u_i\rangle)}{\delta t} + \frac{\delta(\rho\langle u_i\rangle\langle u_j\rangle)}{\delta x_j} = -\frac{\delta p}{\delta x_i} + \frac{\delta \mu}{\delta x_j}\left(\frac{\delta\langle u_i\rangle}{\delta x_j} + \frac{\delta\langle u_j\rangle}{\delta x_i}\right) + \frac{\delta(-\rho\langle u_i' u_j'\rangle)}{\delta x_j} \tag{3.14}$$

To close the RANS equations, the 1-equation Spalart-Allmaras (SA) turbulence model [46] is used in this study. Previous propeller-wing interaction studies [34, 47] showed good comparison to experimental studies using this turbulence model. To limit computational cost, this study aims to achieve a $y^+ = 30$ and therefore modeling the boundary layer with a wall function. The turbulent viscosity ratio is set to 10 similar to the value used in previous wing-propeller research performed by Stokkermans et al. [47]. The application of this wall function does mean that the flow close to the wall is purely modeled, which means that in complex non-equilibrium flows like for example in re-circulation and high pressure gradients this modeling approach will assume different velocity profiles than the computed ones [48]. This in turn can result in a incorrect prediction of the shear forces and separation location.

### 3.4.3. DOMAIN AND BOUNDARY CONDITIONS

Two volume domains are used in this research. The main domain is represents the free-stream domain using periodic boundary conditions at the span-wise boundaries. The size domain affects the accuracy and stability of the solution at a computational cost. The domain has been selected to give a modeling error of up to 1% on the lift coefficient. After performing a convergence study, which is not discussed in this report, the distance to the far-field boundaries have been selected. The domain encloses the model, where the vertical distance to the model is 11c, the upstream and downstream distance to the model is 12c and 14c respectively, as illustrated in Figure 3.10a. The width of the domain is defined by the propeller width and the clearance between subsequent propellers. In this study the tip clearance of the propellers is set at 7% $D_p$ and therefore the domain width equals 1.07 $D_p$. The distance between the propeller and the edge of the domain equals 3.5% $D_p$ on either side as can be seen in Figure 3.10b. This propeller to propeller tip clearance is selected to be comparable to previous distributed propulsion studies investigating the propeller spacing [41].

The inlet is modeled as a velocity inlet and the outlet is modeled as a pressure outlet with a reference pressure of 0 Pa and reference temperature of 288.15 K. All further atmospheric inputs are further derived from the international standard atmosphere and the dynamic viscosity is computed from Sutherland's law. The inlet boundary condition is also applied on the lower and upper boundary as illustrated in Figure 3.10a, such that a change in inflow angle can be simulated from the domain. This is useful, since it prevents requiring a mesh change when the angle of attack is to be changed to obtain the desired lift coefficient. The sides of the domain are modeled as periodic boundary conditions, simulating an infinite array of propellers.

The second computational domain is a numerical wind tunnel domain is shown in Figure 3.11. The upstream and downstream distance to the inlet and outlet is 3.2 c and

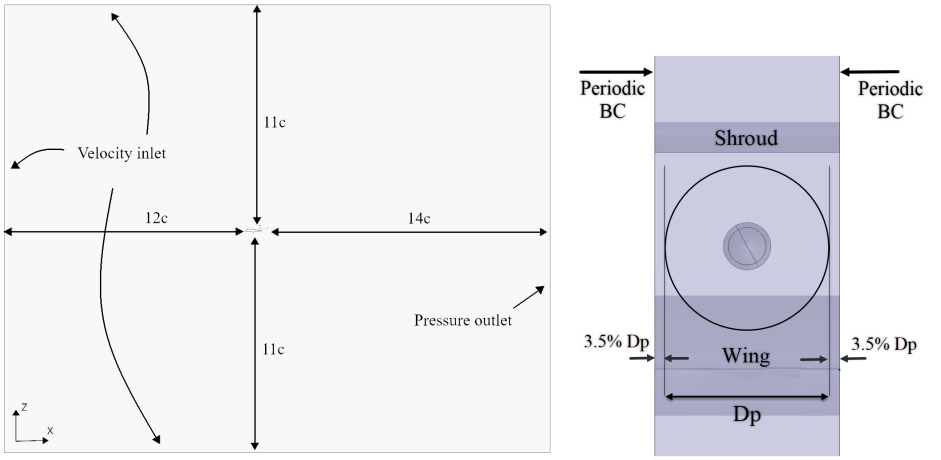


(a) Domain side view

(b) Domain front view

Figure 3.10: Free-stream computational domain geometry geometry and boundary condition

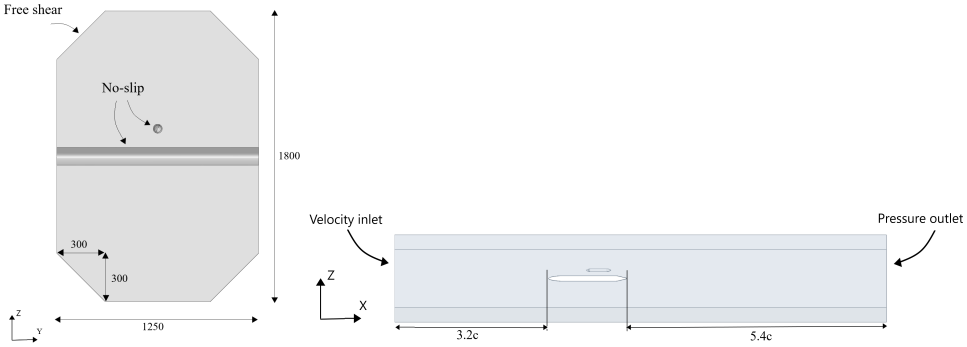


(a) Cross-sectional front view

(b) Side view

Figure 3.11: Wind tunnel computational domain

5.4 c respectively, which is based on the numerical model used in Sören [21]. This geometry is modeled after the geometry of the wind tunnel used in the experiment by de Vries [20]. The model used in the experiment is shown in Figure 3.12 and has been recreated and enclosed in this computational wind tunnel domain. The octagonal test section includes the wing placed in the center spanning the full width of the wind tunnel. The real-life wind tunnel model has slightly diverging walls to prevent the blockage induced by the boundary layer on the walls. The numerical model has a constant cross-sectional area and the walls are modeled as free-shear walls to remove any of these blockage effects. The wing and nacelle are modeled as no-slip walls where the boundary layer is resolved with the use of wall functions, where the $y^+ < 30$. The inlet is modeled as a velocity inlet with a inlet velocity boundary condition. The outlet is modeled as a pressure

outlet where the static pressure is the set to the standard sea level pressure.

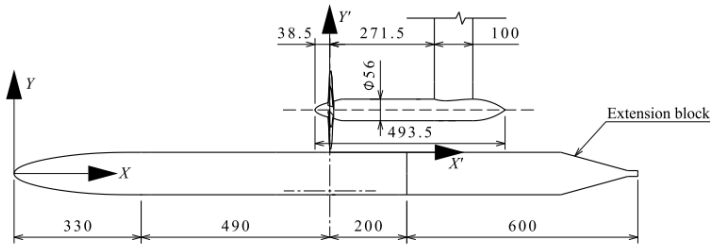


Figure 3.12: Model used in de Vries et al. [20], Figure adapted from Ref [20]

## 3.5. PROPELLER PERFORMANCE ESTIMATION

The performance of the propeller can be estimated with a variety of numerical methods ranging from BEM models to high fidelity time-dependent CFD simulations. The key phenomenon that has to be properly captured in the propeller performance estimation, is to predict the change in propeller performance as a result of the wing induced flow field. Given the desire to analyze a wide array of designs and optimize the propeller efficiency with a constant power setting, the method needs to be computationally inexpensive enough to be evaluated multiple times per design iteration. With this computational requirement, RANS CFD methods where the propeller blade is fully represented in the domain are too computationally expensive. A lower order model such as a a BEM adapted for a non-uniform inflow would be an alternative low cost option, but it may lack the ability to capture relevant flow phenomena. A recently developed engineering method by van Arnhem et al. [34] used a lower-order model to compute the effect of non-uniform loading by using a sensitivity map computed through RANS CFD to estimate propeller performance. This method is computationally efficient, while still preserving the relevant flow phenomena found when using higher order methods. One adaptation to the method is the addition of a correction factor to model the performance impact of varying the propeller pitch.

The process of computing non-inflow induced propeller performance is described in Section 3.5.2. The propeller blade pitch correction and propeller efficiency optimization is further described in Section 3.5.3. After the propeller performance is computed, the final disk loading is exported and subsequently passed in to the OTW Fluent simulation, which with the use of an actuator disk model inserts these forces as momentum sources into the flowfield. This procedure is further detailed in Section 3.5.4.

### 3.5.1. IMPLEMENTATION

A flowchart on how the propeller performance estimation is set-up is shown in Figure 3.13. This computation is performed in MATLAB and is called through Python after providing the relevant inputs, following the availability of the propeller performance estimation code. The outputs are fed back to the python workflow after completion. There are two main components to this process, firstly the computation of the non-uniform

performance of the propeller and secondly the correction of the isolated propeller performance following a blade pitch correction using a BEM method while optimizing for propeller efficiency. The BEM analysis tool used is XROTOR and it serves as a tool to assess the performance impact of changing pitch. The non-uniform propeller performance method uses isolated propeller performance sensitivity maps obtained in previous simulations performed by van Arnhem et al. [34]. This data is used to compute the isolated propeller performance at $\beta_{07} = 45$ deg and $J = 2.0$. These thrust and torque distributions are then scaled following a blade pitch correction using a BEM method. In parallel to this, the change in propeller performance as a result the non-uniform inflow is computed. Both this change in propeller performance and the pitch corrected isolated performance are combined and all relevant output variables are computed and normalized. After this computation, the propeller efficiency and propeller power coefficient are evaluated to see if the propeller efficiency is optimal while power coefficient is equal to the pre-determined constrained value. When this condition is not reached, an optimization procedure is employed which changes the blade pitch and advance ratio targeting this condition.

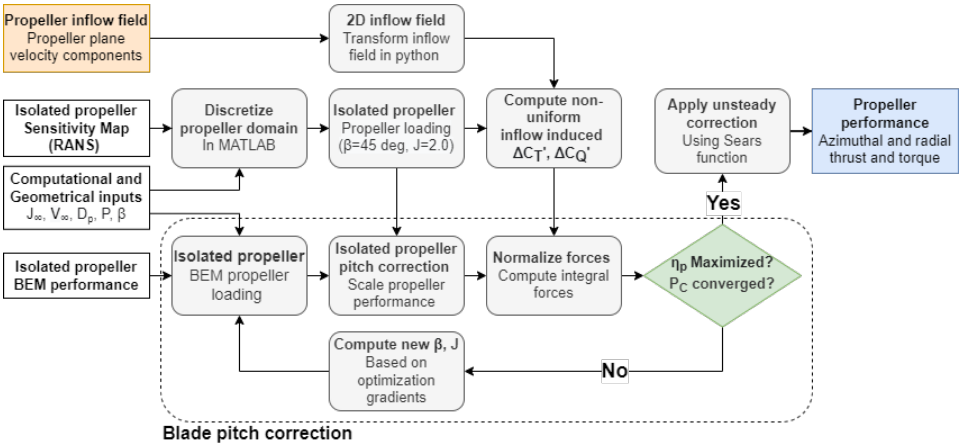


Figure 3.13: Flowchart of propeller performance estimation

The propeller efficiency is a combination efficiency obtained at a certain pitch using a BEM method (as described in Section 3.5.3 as part of the variable pitch correction) and the contribution the change in efficiency as a result of the non-uniform inflow, as shown in Equation 3.15. The change in efficiency as a result of the non-uniform inflow follows from the propeller performance engineering method employed (as created by van Arnhem et al. [34]), which further is discussed in Section 3.5.2.

$$\eta_p = (\eta_{p,\text{Isolated}})_{\text{Pitch-corrected}} + \Delta\eta_{p,\text{Non-uniform}} \tag{3.15}$$

### 3.5.2. NON-UNIFORM INFLOW PROPELLER PERFORMANCE

The performance estimation starts by obtaining the isolated propeller performance from a sensitivity map where the isolated propeller at different advance ratios. This sensitivity

map is obtained with the use of a RANS simulation as described in Stokkermans et al. [47] and performed by van Arnhem et al. [34]. The isolated propeller performance is used to later subtract from the non-uniform inflow propeller performance to obtain the change in performance due to the non-uniform inflow. The sensitivities to the propeller inflow are evaluated at an advance ratio where the efficiency is maximized, which in this report is at $\beta_{07} = 45$ deg, with an advance ratio of $J = 2.0$.

The engineering method developed by van Arnhem et al. [34] is used to estimate the loading distribution of a propeller operating in arbitrary non-uniform flow. The first step in the estimation process is discretizing the propeller domain in radial and azimuthal sections. Each of these sections will have its own loading, where sectional torque and thrust coefficients are identified by adding a apostrophe to the variable. The general principle of the non-uniform inflow propeller performance estimation method is that the local changes in inflow ($\Delta u$, $\Delta v$, $\Delta w$) compared to the uniform isolated flow condition result in a local change in loading ($\Delta C'_T$ and $\Delta C'_Q$) on the propeller blade. This quasi-steady procedure is illustrated in Figure 3.14 [34]. The propeller is discretized in a set of radial ($r/R_p$) and azimuthal ($\phi$)locations. The variables including a prime indicate the local discretized element. The local change in loading is equal to the local loading difference between the propeller at operating at $J_\infty$ and operating at $J_{\text{eff}}$ while experiencing an uniform inflow. Therefore, the method needs the isolated propeller loading distributions at several advance ratios. The local change in velocity is categorized as changes in axial and tangential velocity due to their different characteristic responses to the loading distribution [34]. This results to a local effective axial $J_a$ and tangential advance ratio $J_t$ as defined in Equation 3.16 and Equation 3.17 [34].

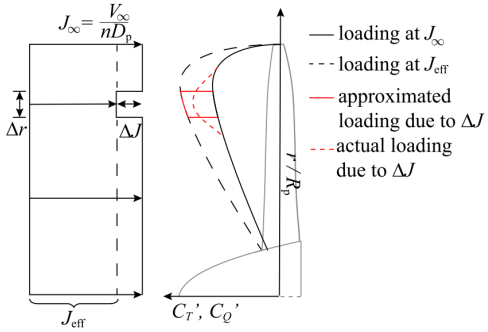


Figure 3.14: Illustration of general working principle of the propeller performance estimation method in a nonuniform inflow field [34], illustration adapted from van Arnhem et al. [34]

$$J_{eff,a}(r,\phi) = \frac{\Delta V_a(r,\phi)}{nD_p} + \frac{V_\infty}{nD_p} \tag{3.16}$$

$$J_{eff,t}(r,\phi) = \frac{V_\infty}{\left(n + \frac{\Delta V_t}{2\pi r}\right) D_p} - \frac{V_\infty}{nD_p} \tag{3.17}$$

The local changes in thrust and torque due to the change of the axial advance ratio are stated in Equation 3.18 and Equation 3.19 [34], where local the change in thrust and

torque is a function of the difference between the local thrust and torque at the effective advance ratio and the local thrust and torque at the free stream advance ratio.

$$\Delta T'_a(r,\phi) = \left(C'_T(J_{eff,a})\frac{\rho}{\rho_\infty} - C'_T(J_\infty)\right)\rho_\infty n^2 D_p^4 \tag{3.18}$$

$$\Delta Q'_a(r,\phi) = \left(C'_Q(J_{eff,a})\frac{\rho}{\rho_\infty} - C'_Q(J_\infty)\right)\rho_\infty n^2 D_p^5 \tag{3.19}$$

Similarly, the local changes in thrust and torque due to the change of the tangential advance ratio are stated in Equation 3.20 and Equation 3.21 [34].

$$\Delta T'_t(r,\phi) = \left(C'_T(J_{eff,t})\left(n+\frac{\Delta V_t}{2\pi r}\right)^2\frac{\rho}{\rho_\infty} - C'_T(J_\infty)n^2\right)\rho_\infty D_p^4 \tag{3.20}$$

$$\Delta Q'_t(r,\phi) = \left(C'_Q(J_{eff,t})\left(n+\frac{\Delta V_t}{2\pi r}\right)^2\frac{\rho}{\rho_\infty} - C'_Q(J_\infty)n^2\right)\rho_\infty D_p^5 \tag{3.21}$$

Combining and normalizing these changes in thrust and torque results in the overall change in thrust coefficient and torque coefficient as shown in Equation 3.22 and Equation 3.23 [34].

$$\Delta C'_T(r,\phi) = \frac{\Delta T'_a + \Delta T'_t}{\rho_\infty n^2 D_p^4} \tag{3.22}$$

$$\Delta C'_Q(r,\phi) = \frac{\Delta Q'_a + \Delta Q'_t}{\rho_\infty n^2 D_p^5} \tag{3.23}$$

These local changes in thrust coefficient and torque coefficient are then integrated to obtain the changes of the integral propeller forces and moments as shown in Equation 3.24 and Equation 3.25 [34].

$$\Delta C_T = \frac{B}{2\pi}\int_0^{2\pi}\int_{R_h}^{R_p}\Delta C'_T(r,\phi)\,dr\,d\phi \tag{3.24}$$

$$\Delta C_Q = \frac{B}{2\pi}\int_0^{2\pi}\int_{R_h}^{R_p}\Delta C'_Q(r,\phi)\,dr\,d\phi \tag{3.25}$$

In addition to the previously quasi-steady estimation a correction for the unsteady effects is taken into account in the method, given that the response of an airfoil to the change in inflow is not instantaneous. The method employs a correction to the thrust and torque distributions by applying Sears' function [34, 49].

### 3.5.3. VARIABLE PITCH CORRECTION

One adaptation to the model as presented by van Arnhem et al. [34] is the inclusion of a variable pitch. Conventionally, the existing isolated propeller data is evaluated at a constant pitch. Changing the propeller pitch ($\beta_{0.7}$) changes the local inflow angle of the propeller blade and therefore changes the loading distributions, which results in a change in propeller efficiency as illustrated previously in Figure 2.6. Since the goal in this

project is to analyze the optimal system performance, selecting the pitch that results in the most optimal efficiency is critical for a fair comparison of designs.

Since the isolated performance data at various advance ratios is only available at a constant pitch ($\beta_{0.7}$ = 45 deg), an alternative means of obtaining the relation of $C_T$ and $C_Q$ to $\beta$ needs to be found. Alternative methods of obtaining these parameters are lower order methods or experimental data. In this research it is opted to use a BEM model to evaluate the pitch sensitivity at a given advance ratio, due to the low computational cost and ability of evaluating small changes in pitch and advance ratio. A comparison of the RANS, experimental and BEM method is shown in Figure 3.15 [34]. The maximum efficiency of the BEM results is very constant over the different values of pitch. The RANS method predicts the highest efficiency and the experimental the lowest.

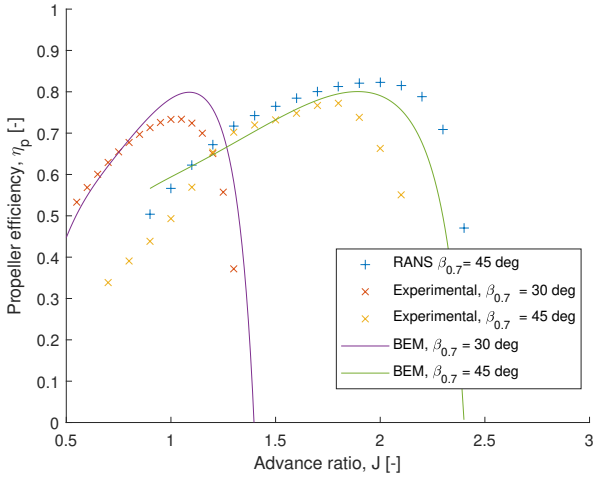


Figure 3.15: Propeller efficiency computed by different methods [34]

The BEM method used is the XROTOR v7.55 developed by Drela [50], where the airfoil performance is obtained from RFOIL v1.1. The implementation of this pitch variation is based upon several assumptions. Firstly, the changes in pitch made in order to obtain maximum efficiency at a constant propeller power are assumed to be small (in the order of +/- 5deg). The propeller propeller power setting is selected such that the optimal propulsive efficiency is obtained with a blade pitch close to 45 deg, at which blade pitch angle the isolated propeller performance data is gathered. Therefore, small changes are assumed to have limited effect on the normalized radial loading distributions. The change in loading due to the non-uniform inflow is assumed to be independent of pitch as the optimal efficiency of the propeller in each given inflow field is optimized. The change in efficiency as a result of the non-uniform inflow field is evaluated at the advance ratio corresponding to the maximum efficiency for the propeller at the given propeller pitch of 45 deg.

One correction to the BEM data had to be made due to the amount of noise resulted by varying the advance ratio to obtain the $C_T$-$J$ and $C_Q$-$J$ curves at different values of $\beta$.

It was observed that this numerical noise prevented the propeller optimization, which aimed to get maximum propeller efficiency, in finding the optimum efficiency. Instead of running the BEM code during the propeller efficiency optimization, it is opted to compute the propeller performance beforehand, such that this noise can be filtered. The propeller performance is calculated with advance ratios varying from 0.9 to 3.4 in steps of 0.01 and the propeller blade pitch is varied from 40 deg to 50 deg in steps of 0.1 deg. The response of the propeller power and thrust is fitted with a fourth order polynomial at each propeller blade pitch resulting in a set of fitted power and thrust curves. An example of the resulting fit of the propeller power coefficient is shown in Figure 3.16a. After fitting both the propeller power and thrust, the resulting efficiency is computed and shown in comparison to the original noisy data in Figure 3.16b. As can be seen, the resulting efficiency curve is now smooth, which is a pre-requisite for the optimization.

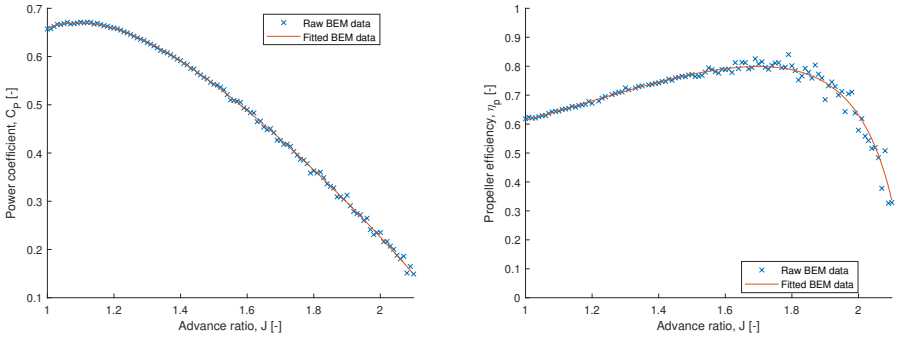


(a) BEM propeller power coefficient

(b) BEM propeller efficiency

Figure 3.16: BEM data noise filtering

After fitting the data, matrices of propeller efficiency, thrust- and torque coefficients are obtained. Combining the efficiency vs eta curves of matrices cover a space as shown in Figure 3.17, where the maximum efficiency at a given propeller power coefficient lies on the top of these combined curves. Moving along maximum efficiency points of these curves by varying the advance ratio shows that the propeller efficiency while changing the propeller pitch, is fairly constant. This opposed to when following the propeller efficiency along one of these curves when changing the advance ratio, where the propeller efficiency changes significantly.

The blade pitch correction part of the code includes an optimization procedure to obtain maximum propulsive efficiency at a pre-defined propeller power target. Constraining the propeller power within the propeller performance estimation is computationally efficient, since the computationally expensive RANS calculations are not needed when constraining this parameter inside the propeller performance estimation. The propeller propeller power is given as an equality constraint for the propeller efficiency optimization and the two design variables used are the advance ratio ($J$) and the propeller pitch ($\beta_{0.7}$). The initial condition for the optimizer is set to the optimal efficiency at the given propeller propeller power in a uniform far field inflow condition. The optimization is performed with the fmincon MATLAB function where the 'interior-point'

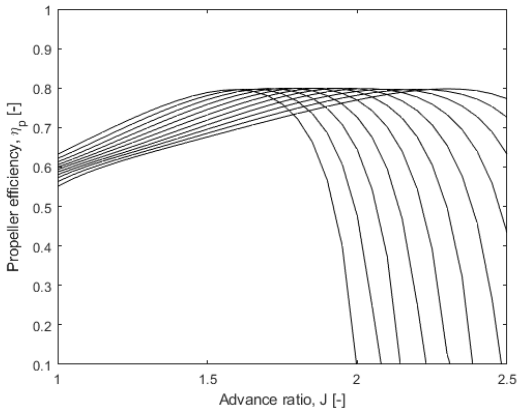


Figure 3.17: Selection of obtained propeller efficiencies at different values of propeller blade pitch $\beta_{0.7}$ = 40 deg to $\beta_{0.7}$ = 50 deg

algorithm is used. This gradient based optimizer is set to terminate when the first-order optimality is smaller than 1e-2 or when the step size to be taken is smaller than 1e-4. The propeller power equality constraint is usually converged well within 1e-4. At the end of every evaluation, the thrust and torque contributions are combined and all relevant propeller disk integral forces and moments are computed and normalized. The constrained optimization is terminated when the tolerances and the first-order optimality are met. When this is the case, the normalized integral forces and moments are corrected for the unsteady effects. On average about 20 to 30 iterations are performed to obtain the optimal efficiency of the propeller in the non-uniform inflow condition.

### 3.5.4. ACTUATOR DISK

The propeller is represented as an actuator disk in the computational domain. The actuator disk model used is developed by Stokkermans et al. [47]. No propeller mesh is required to be generated, since the propeller forces and torque are represented by momentum and energy source terms in the existing cells. The values of the source terms are determined by a UDF function in fluent, which is a compiled C language script developed by Stokkermans et al. [47]. The time-averaged propeller forces and moments are obtained from the propeller performance estimation method as described in in the previous sections. The output from this computation results in the sectional thrust ($T'(r,\phi)$) and torque ($Q'(r,\phi)$) values at all of the radial and azimuthal locations. The sectional thrust and torque are used to compute the momentum and energy to be inserted into the domain as shown in Equation 3.26 and Equation 3.27 [47].

$$F(x,r,\phi) = \eta_x \eta_\phi \left( T' n_T + \frac{Q'}{r} n_Q \right) \tag{3.26}$$

$$S(x,r,\phi) = \eta_x \eta_\phi F \dot{V} \tag{3.27}$$

Where $n_T$ and $n_Q$ ($\phi$) are unit vectors opposing the thrust and torque direction respectively. To avoid singular behavior, the source terms are smoothed by a one dimensional Gaussian kernel, based on the work of Sørensen et al. [51]. The actuator disk model employs this smoothing just in the axial direction, since the azimuthal and radial distributions are already described. An actuator line model would for example additionally employ this smoothing azimuthally. The regularization functions used in the previous equations are defined in Equation 3.28 and Equation 3.29.

$$\eta_x(x) = \frac{1}{\epsilon_{\text{AM}}\sqrt{\pi}} e^{-\left(\frac{|x|}{\epsilon_{\text{AM}}}\right)^2} \tag{3.28}$$

$$\eta_\phi(r) = \frac{B}{2\pi r} \tag{3.29}$$

The regularization function in x-direction ($\eta_x(x)$) contains the regularization constant ($\epsilon_{\text{AM}}$). This constant determines the strength of the Gaussian distribution and is set to the local mesh size width as recommended by Sørensen et al. [51]. This leaves the author to determine the local mesh size. The local mesh at the propeller location features a set of refinement boxes. The process of determining the local mesh size at the actuator disk is further explained in Section 5.1.4.

## 3.6. POST PROCESSING

A significant amount of post-processing of results is performed in this study given the amount of data supplied and desire to understand the system performance. This section describes the relevant equations used to post-process the data shown in Chapter III.

The propeller forces exported from the performance estimation are given in the propeller reference frame. Therefore the thrust component as calculated by the propeller performance estimation does not equal the amount of thrust generated by the system. The net axial thrust is therefore defined by the force generated by the propeller along the flow vector, as illustrated in Figure 3.18. The propeller thrust $T$ and vertical force $F'_Z$ both contribute to the net axial thrust and lift. The net axial thrust generated by the propeller can be computed from Equation 3.30. The propeller angle of attack $\alpha_{\text{p}}$ is the sum of the angle of attack of the main wing $\alpha$ and the propeller inclination $i_{\text{p}}$. The system propeller efficiency is considered in the upcoming sections and is defined using the net axial thrust $T_{\text{net,axial}}$ as calculated by Equation 3.31.

$$T_{\text{net,axial}} = T \cdot \cos\alpha_{\text{p}} - F_{Z'} \cdot \sin\alpha_{\text{p}} \tag{3.30}$$

$$\eta_{\text{p,system}} = \frac{T_{\text{net,axial}} V_\infty}{P} \tag{3.31}$$

The static and total pressures are non-dimensionalised using custom field functions in fluent, which subsequently are output for further analysis and verification. The static pressure coefficient $C_p$ is defined in Equation 3.32 and the total pressure coefficient $C_{p,T}$ is defined in Equation 3.33.

$$C_p = \frac{p - p_\infty}{0.5\rho V_\infty^2} \tag{3.32}$$

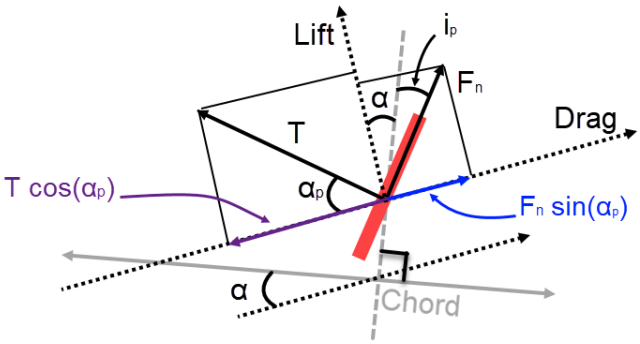


Figure 3.18: Propeller force contributions to net axial thrust

$$C_{p,T} = \frac{p_T - p_{T,\infty}}{0.5\rho V_\infty^2} + 1 \tag{3.33}$$

The performance of the propeller follows from the inflow field supplied to the disk, therefore in future sections the local upwash angle is often used to observe the degree of non-uniformity displayed to the disk. The upwash into the disk is defined in the propeller disk reference frame where an upwash angle of 0 means the flow velocity does not have a vertical component in plane to the propeller disk. the upwash angle is computed by Equation 3.34, where $u'$ is the in plane flow velocity supplied to the disk and $w'$ is the vertical flow velocity in-plane to the disk.

$$\alpha_u = \tan\left(u'/w'\right)^{-1} \tag{3.34}$$

# 4

# DESIGN SPACE

This chapter describes the design space evaluated in this research and highlights the figure of merit (described in Section 4.1) and constraints applied (described in Section 4.2). The operating conditions are defined in Section 4.3. The figure of merit, design variables and performance constraints are summarized in Table 4.3. The design variables mentioned in this table will be varied to investigate their impact on the system performance. These design variables are visualized in Figure 3.3. The design variables are selected to investigate a wide array of geometry variations, while including variables previously investigated in literature to provide additional comparison to literature and increased understanding of the aerodynamic mechanisms. The analysis of the sensitivity of these design variables is further described in Section 7.

Table 4.3: Overview of the design variables, objective and performance constraints

| | **Variable/ function** | **Description** |
|---|---|---|
| **Increase** | $\eta_{\text{p,system}} \cdot C_L / C_D$ | Propulsive efficiency multiplied by lift-to-drag ratio |
| **Design variables** | $X_{\text{main}}$ | Wing geometry |
| | $c_{\text{shroud}} / c$ | Shroud relative chord length |
| | $(x_{\text{shroud}} - x_{\text{propeller}}) / c_{\text{shroud}}$ | Shroud relative axial position to propeller |
| | $i_{\text{shroud}}$ | Shroud inclination |
| | $\epsilon / R$ | Propeller tip clearance |
| | $D_{\text{p}} / c$ | Propeller diameter to chord ratio |
| | $x_{\text{p}} / c$ | Propeller chord-wise position |
| | $i_{\text{prop}}$ | Propeller inclination |
| **Subject to** | $C_L$ - 0.7272 = 0 | Constant lift coefficient |
| | $P_C$ - 0.162 = 0 | Constant propeller power coefficient |

## 4.1. FIGURE OF MERIT

A figure of merit is defined in this section, which is used to compare the system performance of a specific the geometrical design. The aim of the research is to investigate the aerodynamic impact of design variables in a cruise configuration. Therefore, the figure of merit used in this research is derived from the Breguet range equation for propeller aircraft, shown in Equation 4.1. The initial ($W_1$) and final weight ($W_2$) of the aircraft is assumed to be constant, so for a given fuel weight fraction the largest range is to be found. This assumption is made to simplify the problem and confine this study to an aerodynamic investigation only as bounded by this research. It is assumed that the specific fuel consumption $c_p$ is constant, which results in the merit function shown in Equation 4.2. As the lift coefficient in this study is constrained, this effectively means the figure of merit becomes the ratio of propulsive efficiency to drag coefficient.

$$R = \frac{\eta_p}{g c_p} \frac{C_L}{C_D} ln\left(\frac{W_1}{W_2}\right) \tag{4.1}$$

$$K = \eta_{p,system} \frac{C_L}{C_D} \tag{4.2}$$

## 4.2. PERFORMANCE CONSTRAINTS

The performance constraints are in place to ensure fair comparison between designs and represent the same cruise condition in all design evaluations. Two performance constraints are in place, a constant lift coefficient constraint and a constant propeller power coefficient constraint. These constraints are implicitly constrained in one computation loop. Both of these constraints are defined as equality constraints.

The lift coefficient is defined in Equation 4.3. The total lift is equal to all forces in the direction perpendicular to the inflow vector. The lift of the aerodynamic surfaces combined with the force acting on the propeller directed in the lift vector. The angle which the propeller is inclined to the flow is the combination of the angle attack and the propeller incidence angle. The constant lift coefficient is maintained by solely varying the angle of attack of the system. The angle of attack is the main driver in the lift coefficient and the relation between the two is close to linear at the specific cruise condition. The procedure of maintaining a constant lift coefficient is visualized in Figure 3.1. The same geometry is evaluated at several angles of attack until the lift coefficient is within 1% of the required lift coefficient. Generally two to three of these iterations are needed to get the lift coefficient in this range. To maintain the equality constraint, the final two iterations are linearly interpolated by computing the $C_L - \alpha$ slope to obtain the output results at the predefined lift coefficient.

$$C_L = \frac{L_{wing} + L_{shroud} + L_{nacelle} + F_z \cdot \cos(\alpha + i_{prop}) + T \cdot \sin(\alpha + i_{prop})}{0.5 \rho_\infty V_\infty^2 S_{ref}} \tag{4.3}$$

Maintaining a realistic axial force balance is of importance, since the specified cruise condition needs to be maintained for fair comparison. The total axial force balance needs to equal zero to maintain a constant aircraft velocity. Ideally, a constant specific excess thrust is maintained in all simulations. Implementing this comes at a high computational penalty as the drag of the system has to be known before this constraint can

be evaluated. This system drag is only obtained after performing a full CFD run. Observing that the propeller performance computation is significantly faster, it is opted to constrain a purely propeller related variable that could opt as this axial force balance constraint. The propeller power coefficient is selected to be constrained, since it gives each design the same amount of propulsive shaft power and the goal is to use this as efficiently as possible by generating as much thrust in the flow direction as possible.

## 4.3. OPERATING CONDITIONS

The simulations are run at sea level conditions and the operating conditions are calculated using the international standard atmosphere. The input parameters used for the initial and boundary conditions can be found in Table 4.4. The initial conditions are selected because the model used for propeller performance estimation uses propeller data obtained at 40 m/s at sea level conditions and therefore the CFD model initial conditions are selected to match these conditions. It has to be noted that these conditions do not represent a in cruise full scale aircraft because of a discrepancy in Reynolds and Mach number. The reference aircraft for this study is the ATR-72 600 operating in cruise. This regional fixed wing turboprop aircraft is often used as a reference aircraft for hybrid propulsion aircraft studies and OTW propulsive studies [33, 52, 53] and an illustration is given in Figure 4.19. The specifications of the ATR-72 600 reference aircraft are shown in Table 4.5 [54]. The parameters are obtained from the "Jane's All the Worlds Aircraft" database and the flight level "FL230" is selected.

Table 4.4: Simulation input parameters based on wind tunnel operating conditions

| **Input parameter** | **Value** |
|---|---|
| Flow velocity | 40 $m/s$ |
| Density | 1.225 $kg/m^3$ |
| Static temperature | 288.15 $K$ |
| Reference pressure | 0 $Pa$ |

Figure 4.19: ATR72-600 reference aircraft [1]

[1] https://www.atr-aircraft.com/wp-content/uploads/2020/07/ATR-100135HD-scaled.jpg

The two constrains on performance are the lift coefficient and the propeller power coefficient, which are derived from the reference aircraft. To compute the lift coefficient used in this model it is assumed that the aircraft cruise weight equals the lift of the aircraft. The cruise weight is assumed to be 95% of the aircraft Maximum Take-Off Weight (MTOW). The Mean Aerodynamic Chord (MAC) is computed from the tip and root chord and equals 2.12 m. The lift coefficient is computed using Equation 4.4 and equals 0.7272.

$$C_L = 0.5\rho_\infty V_\infty^2 S_{\text{ref}} \tag{4.4}$$

The propeller is constrained by the propeller power coefficient, which is derived from the disk loading of the reference aircraft. The propeller thrust coefficient $T_C$, as normalized by the propeller disk area $A_P$ and the dynamic pressure, is calculated in Equation 2.5, where $A_P = \pi D_P^2/4$. Using the parameters shown in Table 4.5, the $T_C$ is equal to 0.108. The input data for the propeller performance estimation is obtained at a blade pitch $\beta_{07}$ = 45 deg. The maximum efficiency of the isolated propeller at this propeller pitch is obtained at a slightly higher $T_C$. For this reason, the numerical model uses a 20% increment to this $T_C$ to result in a maximum efficiency where the propeller pitch of the isolated propeller at maximum efficiency is closer to $\beta_0 7$ = 45.0 deg. The isolated propeller $T_C$ used in this study is selected to equal to 0.129. Computing the isolated performance of the XProp-S using the atmospheric conditions showed in Table 4.4, this $T_C$ corresponds to a advance ratio of $J$ = 2.00, a propeller blade pitch of $\beta_{07}$ = 45.9 deg, thrust coefficient of $C_T$ = 0.202, torque coefficient of $C_Q$ = 0.0805, propeller efficiency of $\eta_p$ = 0.800, thrust of $T$ = 4.10 N and power of $P$ = 205.5 W. The numerical model constrains the propeller power coefficient to $P_C$ = 0.162 (as computed from Equation 2.8) in the optimization performed inside the propeller performance estimation.

Table 4.5: Reference aircraft ATR-72 600 specifications [54]

| **Parameter** | **Value** |
|---|---|
| Maximum take-off mass | 22800 kg |
| Cruise velocity | 127.5 m/s |
| Air density in cruise | 0.5893 kg/m$^3$ |
| Cruise altitude | 7010 m |
| Estimated Lift/Drag | 17 |
| Number of propellers | 2 |
| Propeller diameter | 3.93 m |
| Wing surface area | 61 m$^2$ |
| Root chord | 2.57 m |
| Tip chord | 1.59 m |
| Wing span | 27.05 m |
| Fuselage diameter | 2.865 m |

The baseline diameter to chord ratio of the OTW system is set to $D_p/c$ = 0.242. This value is selected to be in the range of previous OTW propulsion experiments performed by de Vries et al. [20] and Marcus [7]. The specific value of $D_p/c$ used in this reports is based on a few assumptions of an OTW aircraft configuration based on the geometrical

parameters of the ATR-72 600 as shown in Table 4.5. It is assumed that 30% of the power in cruise is generated by the OTW distributed propulsive array, 10 propellers are installed on each side of the wing, the spacing between propellers is equal to 7% $D_p$ and the $T_C$ incremented by 20%. These parameters result in the propeller array width of 50% of the total wing span. The total thrust generated by the aircraft and the cruise velocity is assumed to be constant. The total Over-The-Wing Distributed Propulsion (OTWDP) propeller area is calculated using Equation 2.5, with $T_C = 0.129$, total thrust $T = 3750$ N ($T = 0.3 \cdot L/D \cdot MTOW \cdot 9.81 \cdot 0.95$), cruise velocity $V_\infty = 127.5$ m/s, air density in cruise $\rho = 0.5893$ kg/m$^3$. This results to a total OTWDP propeller area of 6.07 m$^2$ and with 20 distributed propellers a propeller area of 0.303 m$^2$, giving each propeller a diameter of $D_p = 0.621$ m. The ATR-72 600 root chord is used to compute the diameter to chord ratio of $D_p/c = 0.242$. The propeller diameter used for the study is equal to $D_p = 0.2032$ m. Using the $D_p/c = 0.242$, the baseline chord length of the main wing in the numerical model is set to 0.84 m.

# III

# Validation and Results

# 5

# VERIFICATION AND VALIDATION

There are various types of errors present in computational modeling. Three main sources of error are identified in this section and the extent these sources of error affect the accuracy of the solution is investigated in the following sections. This investigation follows various verification and validation studies performed to show the discrepancies in the modeling approach used in this research.

Aspects like turbulence are traditionally modeled and introduce **modeling errors**. This study models the flow to be steady and computes an averaged solution using the RANS equations, thereby introducing a modeling error. The propeller in this study is modeled by introducing an actuator disk. Additionally, the computation is performed on a finite domain, therefore the boundaries are modeled with the use of boundary conditions. The value prescribed on these boundaries is an estimation of the conditions in the far-field. Differences in the model geometry are often present in numerical models following simplified geometry when omitting smaller details in the model. To investigate the impact and magnitude of the modeling errors, a validation study has been performed in Section 5.2.

The governing equations are a set of differential equations which are discretized to be solved numerically. This spatial and temporal discretisation produces an approximate solutions. The finite volume method employed by the ANSYS Fluent software package employs approximate surface and volume integrals. Increasing the spatial and temporal discretisation in turn increases the accuracy of the solution, but this also severely increases the computational cost of the computation. Given that the simulation is assumed to be steady state, temporal resolution is not applicable in this simulation. The **discretisation error** induced by the spatial discretisation is estimated in Section 5.1.1.

The discretized equations are solved iteratively, which introduces an **iterative error** as the solving process has to be stopped at a some stage. The convergence criterion chosen define when to stop this process. The lower limit of the iterative error is set by the machine precision and therefore double precision is used. The value of the residuals for which the iterative error is deemed acceptable is evaluated in Section 5.1.2.

## 5.1. VERIFICATION STUDIES

This section will describe several verification studies performed. The discretisation error is assessed in Section 5.1.1 by performing a grid convergence study. The iterative error is evaluated in Section 5.1.2. To get an idea on the impact of the impact of the

turbulence modeling the wing pressure and friction profiles are sanity checked in Section 5.1.3. Finally, a small study on the behavior and set-up of the actuator disk is made in Section 5.1.4.

### 5.1.1. GRID CONVERGENCE

The discretization error $\epsilon_d$ introduced by the level of mesh refinement is assessed by running a grid convergence study. The grid refinement is varied systematically to observe the impact on the lift and drag coefficient of an isolated wing. These output variables are expected to converge with increasing mesh refinement. The discretisation error used in this thesis is based on the power series expansion highlighted in Equation 5.1. Where $\alpha$ is a constant, $h_i$ is the typical cell size and $p$ is the order of convergence [55]. The typical cell size is computed by dividing the volume of the domain $V_i$ by the number of cells $n_i$ in the volume and taking the cubic root as shown in Equation 5.2. As the typical cell size $h_i$ tends to 0, the discretization error also tends to zero, meaning that an infinitely dense grid will give the actual solution.

$$\epsilon_d = \alpha h_i^p \tag{5.1}$$

$$h_i = \left(\frac{V_i}{n_i}\right)^{\frac{1}{3}} \tag{5.2}$$

The five typical cell sizes $h_i$, shown in Table 5.1, are evaluated and plotted in Figure 5.1. The normalized lift and drag coefficients are plotted against the ratio of typical cell sizes $h_i/h_1$, where $h_1$ is the smallest typical cell size evaluated. A quadratic fit is made to the data points estimating the value of lift and drag for an infinitely dense mesh ($h_i/h_1$=0). Secondly, the best fit through the data is taken by taking the best least squares fit of Equation 5.1, resulting in an order of convergence of $p$ = 1.709 for the lift coefficient and $p$ = 0.798 for the drag coefficient. The lift coefficient is observed not monotonically converging, while the drag coefficient is monotonically converging. The order of convergence for both variables is in the range of 0.5 to 2.0, which falls in the empirically acceptable range [55].

Table 5.1: Grid sizes used in the isolated wing configuration mesh study

| **Grid** | **Number of cells** | $h_i/h_1$ |
|---|---|---|
| Grid 1 | 13,606,136 | 1.00 |
| Grid 2 | 8,031,677 | 1.19 |
| Grid 3 | 4,998,882 | 1.40 |
| Grid 4 | 3,058,408 | 1.64 |
| Grid 5 | 1,798,568 | 1.96 |

The uncertainty of the solution is calculated by Equation 5.3 [55], where $U_\phi$ is the uncertainty of the variable of interest ($\phi$) at the mesh refinement level. The error $\epsilon_\phi$ that exhibits the smallest standard deviation ($\sigma$) is used for the computation of the uncertainty. The final term $\left|\phi_i - \phi_{\text{fit}}\right|$ is the absolute difference between the computed value

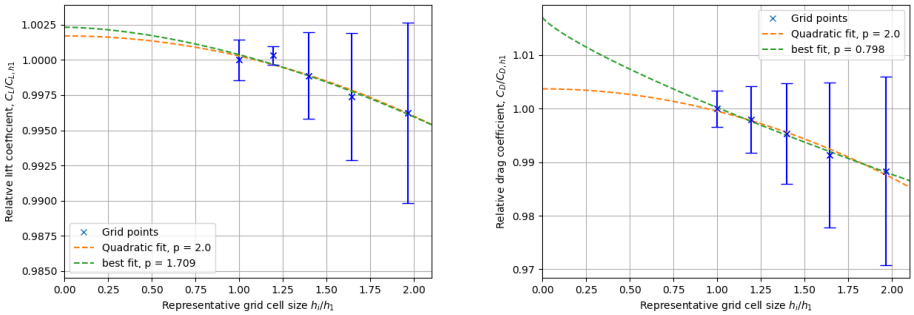


(a) Lift coefficient

(b) Drag coefficient

Figure 5.1: Isolated wing grid discretisation study comparing assessing the convergence of a value of interest ($\phi$) to the typical cell size $h_i/h_1$

of interest and the value of the fitted curve at the chosen value of $h_i/h_1$. Grid 4 is selected for the simulation, resulting in an uncertainty of 0.47% for $C_L$ and 1.35% for $C_D$.

$$U_\phi(\phi_i) = 1.25\epsilon_\phi(\phi_i) + \sigma + \left|\phi_i - \phi_{\text{fit}}\right| \tag{5.3}$$

### 5.1.2. ITERATIVE ERROR

The iterative error is investigated by running a simulation of an isolated wing until all residual values are below 1e-7. The output variables at interest are the drag and lift coefficients of the system. To compare the convergence of these variables, the relative change of the coefficients as compared to the coefficient at a residual of 1e-7 are computed. Note that this value of the coefficient is not fully converged, but the comparison shows the error induced by terminating the solution at an earlier stage. The influence of the residual value on the coefficients is shown in Table 5.2. As can be seen from these figures, the iterative error is relatively small compared to the discretisation and modeling errors. The iteration error should be of an order smaller than the discretisation error in order for the calculation to be accurate [43]. Eça and Hoekstra [55] recommends the iterative error to be two or three orders of magnitude smaller than the discretisation error not to disturb the solution. A residual value of 1e-4 is selected, which results in a 0.001% error in lift and drag coefficient.

Table 5.2: Iterative convergence of an isolated wing simulation

| Residual value | 1e-03 | 1e-04 | 1e-05 | 1e-06 |
|---|---|---|---|---|
| $\Delta C_L$ (%) | -3.01e-02 | -1.03e-03 | 1.88e-04 | 4.28e-06 |
| $\Delta C_D$ (%) | 3.00e-02 | 1.09e-03 | 1.11e-04 | 1.76e-05 |

### 5.1.3. WING PRESSURE DISTRIBUTION

To qualitatively investigate the behavior and modeling error of the CFD modeling approach, the isolated wing performance is compared to an XFoil [56]. A comparison of the pressure and friction coefficient distributions over the wing is made. Both the CFD and the XFoil are simulated at an angle of attack of 4.0 deg and include viscosity and compressibility modeling. The 3D CFD simulation simulates an infinite span given the periodic span-wise boundary conditions used in the Fluent CFD simulation and therefore these can be compared to the 2D XFoil simulation. The mid span wing mesh elements are extracted from fluent to create the 2D profiles. The comparison to Xfoil is shown in in Figure 5.2, where both a fully turbulent and a natural transition simulation are simulated in XFoil. The forced transition in XFoil is applied close to the leading edge to simulate a fully turbulent boundary layer. The laminar boundary layer comes with an increment to the suction on the upper surface and a increase in pressure on the last 0.3c is found at the transition to turbulence. The CFD simulation is modeled to be fully turbulent and compares well to the turbulent XFoil pressure coefficient distribution as seen in Figure 5.2a. The largest impact of the fully turbulent model is the impact on the friction coefficient. Where the laminar boundary layer as simulated by XFoil features a significantly reduced friction coefficient for the laminar portion of the chord. Additionally, after transition, the boundary friction coefficient of the turbulent boundary layer is smaller in the fully turbulent simulation, but the total friction force is higher. Comparing the turbulent Xfoil simulation to the CFD simulation, a similar chord-wise friction coefficient profile is found. The largest discrepancies are found at the leading edge, where the forced transition is applied and at around 0.2c, where the Fluent simulation under predicts the friction coefficient.

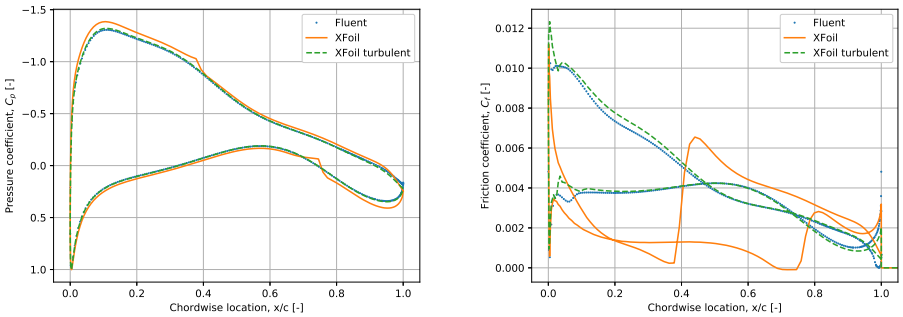


(a) Pressure coefficient

(b) Friction coefficient

Figure 5.2: Chord-wise pressure and friction coefficients of an isolated infinite span wing ($\alpha$ = 4.0 deg, Re = 2.2e6, M = 0.12)

### 5.1.4. ACTUATOR DISK MODEL

The downstream flow field of the actuator disk model, as described in Section 3.5.4, is compared to the full blade RANS simulation [34] in Figure 5.3. Comparing the total pressure, the actuator disk model and the full blade solution match up well in close prox-

imity to the nacelle and from r/R = 0.5 to r/R = 0.8. At the region close to the tip and root, discrepancies start to occur in the axial velocity profile and therefore also the total pressure. At the root region, the actuator disk overestimates the axial velocity and total pressure coefficient. The transition between the free-stream air and the propeller wake is smoothed out in the actuator disk model result resulting in a less discrete transition. One of the main differences between the actuator disk and full blade simulation results, is the lower resolution of the actuator disk model mesh, resulting to more numerical diffusion in the shear layers.

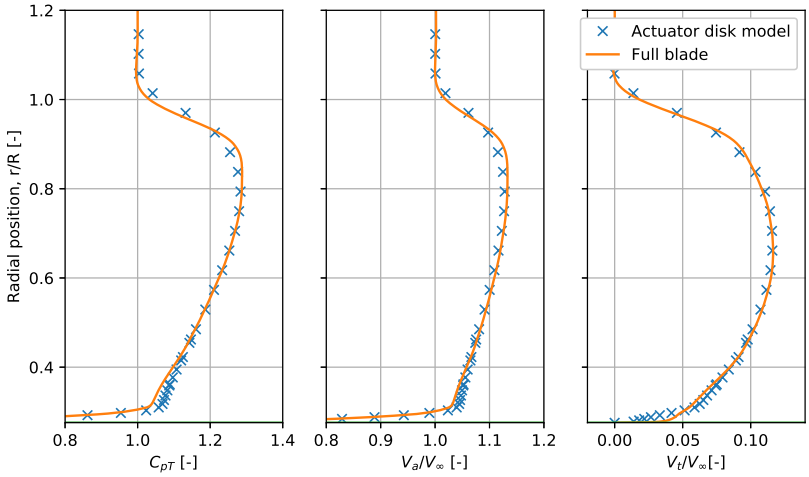


Figure 5.3: Downstream propeller total pressure ($C_{p,T}$), normalized axial velocity ($V_a/V_\infty$) and normalized tangential velocity ($V_t/V_\infty$) distributions of actuator disk and full blade RANS simulations at 1.1 $R_p$ downstream of the propeller [34]

To assess the impact of the actuator model regularization constant ($\epsilon_{\text{AM}}$) (described in Section 3.5.4), a quick study selecting several values of $\epsilon_{\text{AM}}$ is run. The smallest local mesh size in this study is 1 mm and $\epsilon_{\text{AM}}$ is varied from 1 mm to 16 mm. Running the simulation with $\epsilon_{\text{AM}}$ equaling the local mesh size was observed to be unfavorable to the stability of the simulation and causes the simulation not to converge fully to the set stopping criterion. The impact of varying the actuator model regularization constant is shown in Figure 5.4, where the total pressure and pressure coefficients across the actuator disk are shown at a radial position where $r/R = 0.5$. Increasing the actuator model regularization constant, increases the domain in where momentum is added into the domain though the source terms. Higher regularization constants change the propeller induced pressure gradient and pressure coefficient amplitude significantly. The total pressure coefficient shows that the same amount of energy is inserted into the domain downstream from the propeller, but this point is reached later with higher regularization constants. When adding a wing in close proximity to this system, it is important that the propeller induced pressure gradient by the actuator model represents the full blade propeller it is simulating. The full blade propeller has a radially varying chord length

and blade pitch angle as illustrated in Figure 3.5b. To get an estimate for the axial with momentum is inserted into the propeller, the axial propeller width at r/R=0.7 and $\beta$ is calculated. From Figure 3.5b, at r/R=0.7 the blade chord length $c/R$ equals 0.15, which comes down to about 15 mm. At a pitch angle $\beta_{0.7}$ of 45 deg, the chord length in the axial direction equals 10.6 mm. The aim is that the actuator model thickness matches this thickness to approach the similar static and total pressure jump gradients in the actuator model. From Figure 5.4a, it can be found that at $\epsilon_{AM}$ = 2 mm, most of the momentum is inserted into the domain between $X'/R$ = -0.038 and $X'/R$ = 0.038, resulting in an actuator disk thickness of around 0.076 $R$, equaling 7.6 mm (with R = 101.6 mm). This actuator disk thickness is assumed to be in the same order of magnitude as the propeller axial chord thickness and therefore a $\epsilon_{AM}$ = 2 mm, is selected for the study.

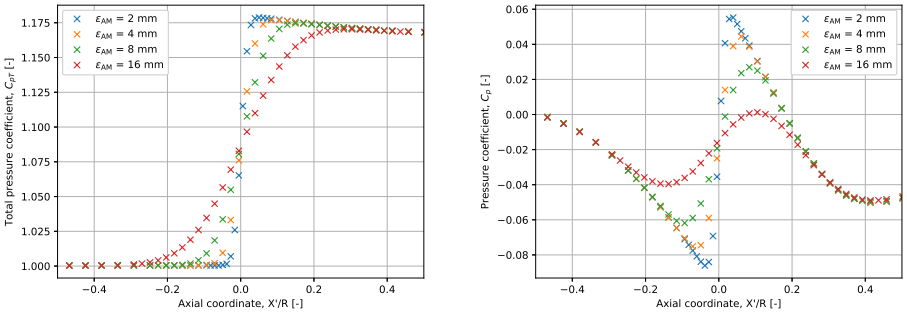


(a) Total pressure coefficient

(b) Pressure coefficient

Figure 5.4: Pressure profiles along the axial coordinate of the isolated propeller at a radial position of $r/R$ = 0.5 ($V_\infty$=40 m/s, $J$=1.8)

## 5.2. COMPARISON TO EXPERIMENTAL RESULTS

This section will highlight the validation study done comparing the numerical results to experimental data. Section 5.2.1 compares the boundary layer profile to experimentally obtained pressure data. The effect the propeller induced pressure field has on the wing is evaluated in Section 5.2.2 and the propeller induced velocity field is evaluated in Section 5.2.3. Finally, a short discussion on the verification and validation results is made in Section 5.3.

### 5.2.1. BOUNDARY LAYER PROFILE

The boundary layer profile of an isolated wing configuration is computed and compared to experimental data. The experimental data provided originates from the experiment described in De Vries et al. [20]. This experiment includes a measurement of the total pressure in close proximity to the isolated "flat plate" wing at a specific axial location (X/c = 0.8). The measurement is performed at a Reynolds number of $1.8 \cdot 10^6$ and of $2.8 \cdot 10^6$ corresponding to a velocity of 20 m/s and 40 m/s respectively. The numerical data follows from the wind tunnel numerical domain and boundary conditions described in Section 3.4.3. The experimental model uses a 3mm wide trip strip located at 7.5% of the chord to create a turbulent boundary layer, this turbulent boundary layer is referred to as "BL1" in the experiment [20]. The numerical model is modeled to be fully turbulent using the Spalart Allmaras turbulence model.

Figure 5.5 shows the comparison between the numerical and the experimental boundary layers. In the majority of the boundary layer, the numerical model predicts higher energy in the flow. When Z'/R is larger than 0.12, the numerical model over-predicts the amount of loss in the flow. Additionally, the boundary layer thickness is larger in the numerical model, where $C_{p,T} = 1$ is reached at around Z'/R = 0.20, compared to around Z'/R = 0.16 for the experimental model. The larger grid spacing in the numerical model at the upper region of the boundary layer is cause for a slight over prediction of the boundary layer thickness. The boundary layer corresponding to the 20 m/s simulation has a lower total pressure than the boundary layer corresponding to the 40 m/s simulation. This is opposed to the experimental data, where the total pressure profiles of the two data sets intersect at Z'/R = 0.08.

### 5.2.2. PROPELLER INDUCED PRESSURE FIELD

To validate the propeller-wing interaction prediction, the numerical simulation has been set up similarly to the experiment described in de Vries et al. [20]. The geometry used for the model is described in Section 3.4.3, using the numerical wind tunnel domain as shown in Figure 3.11.

The propeller induced pressure field on the flat plate is measured through a series of pressure taps at several advance ratios. The numerical pressure coefficients are obtained at the surface of the wing and are compared to the experimental results in Figure 5.6. This graph shows the change pressure coefficient on the wing surface by subtracting the propeller-on condition from the propeller-off condition at several advance ratios (J = 1.225, J = 1.640, J = 1.925) plotted against the axial coordinate. The upstream velocity $U_\infty$ = 20 m/s and the tip clearance $\epsilon/R$ = 0.037. The thrust coefficient at the same advance ratios are over predicted by the numerical model, which is particularly noticeable at the lower thrust settings, where the lowest thrust setting over predicts the thrust coefficient

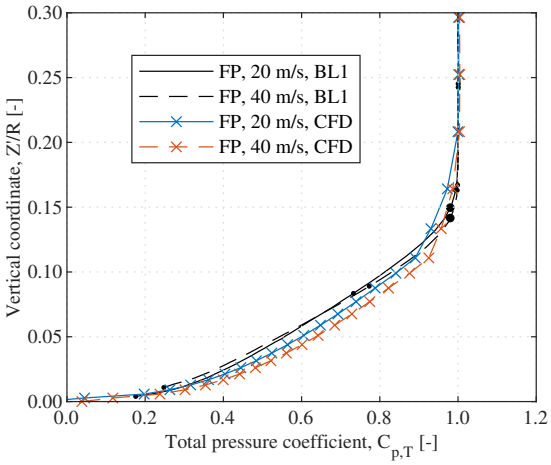


Figure 5.5: Boundary layer profiles of the isolated wing at X/c = 0.8

by 50%. The overestimation is likely driven by the usage of higher Reynolds number propeller data for the input of the numerical propeller performance estimation. Figure 5.7 shows a comparison of the experimental performance of a propeller operating in varying free-stream velocities. The effect of increasing the Reynolds number is clearly visible and increases the thrust coefficient of the propeller at the same advance ratio. A similar increase in thrust coefficient is therefore expected by using higher Reynolds number propeller data as input for the numerical simulation.

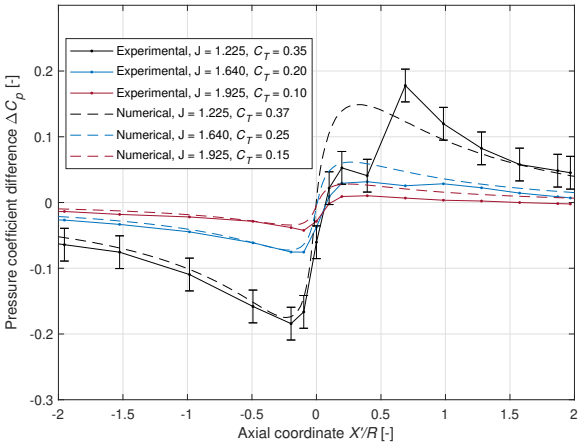


Figure 5.6: Change in surface pressure coefficient along the wing surface as a result of introducing a propeller at various advance ratios

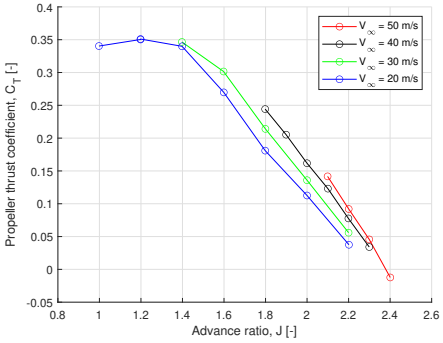


Figure 5.7: Propeller thrust coefficient versus advance ratio at varying free-stream velocities

The pressure coefficient does match up relatively well upstream of the propeller, where the numerical solution in general shows an under prediction of the change in pressure coefficient. Larger differences are observed just downstream of the propeller. This is most clearly visible in the highest thrust setting (J = 1.225), where the delay in the increase of pressure is not observed in the simulation. The secondary peak as observed in the experimental results at $C_T = 0.35$ is also not observed in the numerical simulation. The largest difference in the modeling is the steady state modeling of the propeller and therefore the periodic movement of the blade tip approaching the wing is not modeled. Further downstream, the change in pressure difference between the numerical and experimental results decreases.

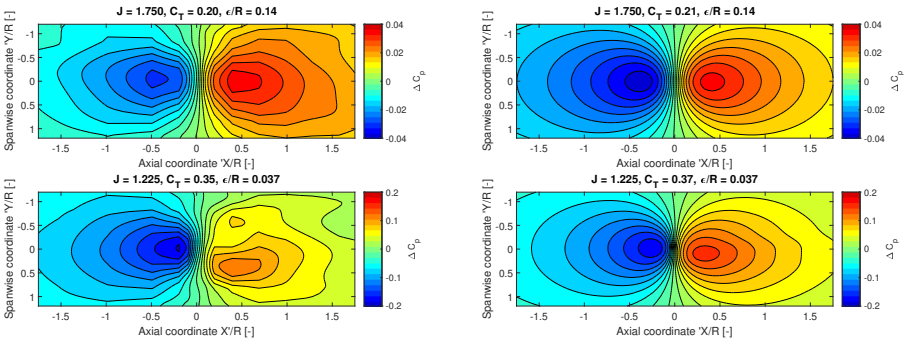


(a) Experimental

(b) Numerical

Figure 5.8: Change in pressure coefficient on flat plate induced by propeller

Two contour plots of the change in pressure coefficient induced by the propeller on the wing surface are shown in Figure 5.8. The top contour plots feature a low thrust setting ($J = 1.750$, $C_T = 0.20$) and a larger tip clearance $\epsilon/R = 0.14$, taken at a free-stream velocity of 40 m/s. The bottom contour plots are computed at a higher thrust level ($J = 1.225$, $C_T = 0.35$) and a lower tip clearance $\epsilon/R = 0.037$, taken with a free-stream velocity

of 20 m/s. The simulated thrust coefficient ($C_T = 0.21$) in the low thrust setting is close to the experimental value of 0.20, with now matching Reynolds numbers for the numerical propeller input data. The downstream change in pressure coefficient shows qualitative agreement, while the upstream change in pressure peak is overestimated by about 28%. The higher thrust and lower tip clearance results shows a 4.5% underestimation of the upstream change in pressure by the introduction of the propeller. The upstream differences in the higher thrust case however are significant as a result of the under prediction of the downstream span-wise shift of the maximum $\Delta C_p$. The numerical simulation does see a contribution of the swirl, but significantly underestimates the amount of this when comparing it experimental data. Additionally, the maximum change in pressure is overestimated by about 24%.

### 5.2.3. PROPELLER INDUCED VELOCITY FIELD

The experimental velocity fields are obtained by a stereoscopic Particle Image Velocimetry (PIV) measurements taken in-between the nacelle and the wing as per the experiment described in de Vries et al. [20]. The geometry used for the model is described in Section 3.4.3 and shown in Figure 3.11.

The numerical propeller velocity field components are compared to the experimental PIV data in this section. The data used in this section features the higher thrust setting ($J = 1.225$, $C_T = 0.35$) and the lower tip clearance $\epsilon/R = 0.037$. Figure 5.9 shows a comparison of the axial velocity field to the experimental results. The largest difference observed is is located in the boundary layer. Both models estimate a increase of boundary layer thickness across the propeller plane as a result of the strong slipstream contraction. The subsequent downwards movement of the streamtube and reduction of the boundary layer thickness is not captured to the same extent as in the numerical model. Figure 5.10 shows several 2D slices further highlighting the comparison between the experimental and numerical results. This figure shows the propeller induced axial velocity as computed by subtracting the prop-on and prop-off axial velocity field. Figure 5.10 shows the shrinking of the experimental boundary layer, which is missing from the numerical model. The axial velocity matches up well in the region between r/R = 0.3 to r/R = 0.7. The numerical model underestimates the axial velocity in the region below r/R = 0.3 and above r/R = 0.7. The boundary layer on the nacelle is smaller in the numerical model.

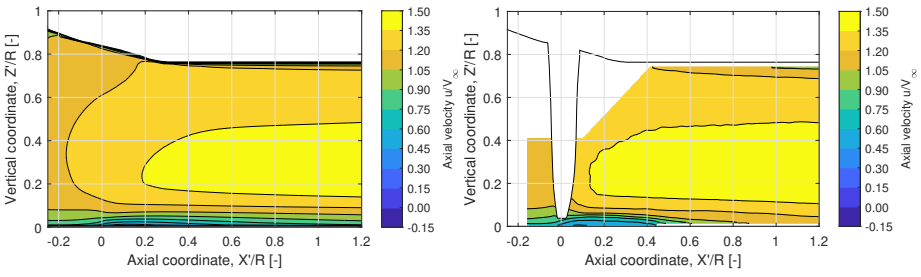


(a) Numerical

(b) Experimental

Figure 5.9: Prop-on axial velocity contours between the nacelle and wing ($J = 1.225$, $\epsilon/R = 0.037$)

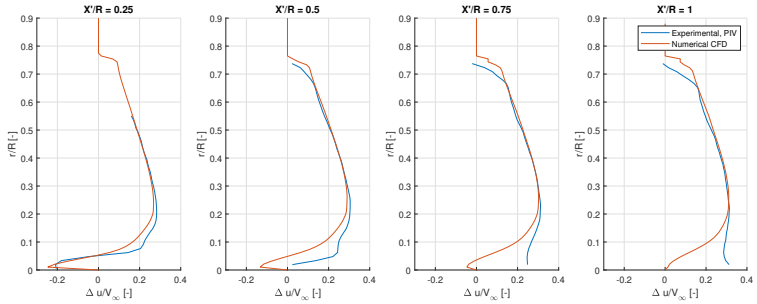


Figure 5.10: 2D Propeller induced axial velocity ($\Delta u = u_{\text{prop,on}} - u_{\text{prop,off}}$) profiles at several axial coordinates for the numerical and experimental models

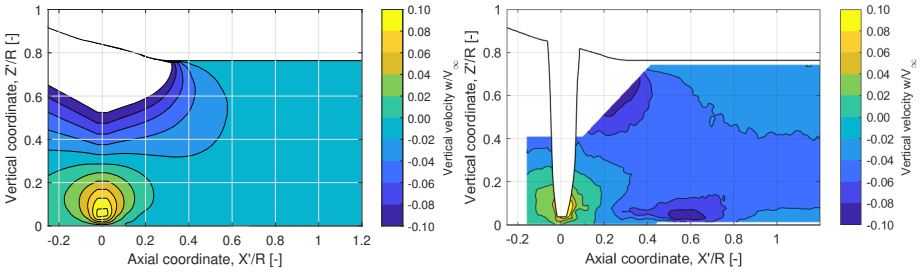


(a) Numerical

(b) Experimental

Figure 5.11: Vertical velocity contours between the nacelle and wing ($J = 1.225$, $\epsilon/R = 0.037$)

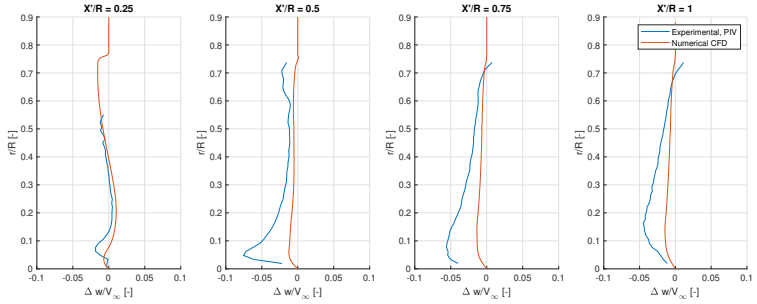


Figure 5.12: 2D Propeller induced vertical velocity ($\Delta w = w_{\text{prop,on}} - w_{\text{prop,off}}$) profiles at several axial coordinates for the numerical and experimental models

A contour plot of the vertical (in-plane) velocity is shown in Figure 5.11. The experimental result shows the downwards movement of the slipstream between X'/R = 0.5 and X'/R = 0.7. Figure 5.12 shows the downwash profile at several axial positions highlighting the propeller induced downwash. The near propeller (X'/R = 0.25) downwashing profile shows similarities in the region of downwash close to the wing surface, although this mechanism is more pronounced in the experimental data. Figure 5.12 shows the

discrepancy between downwards moving slipstream at X'/R = 0.5, where $w/V_\infty$ reaches -0.08 opposed to around -0.015 in the numerical model. In both cases, there is a negative propeller induced vertical component present in the flow. Further downstream, the experimental region of downwash widens, while the downwash profile stays relatively constant in the numerical model.

## 5.3. DISCUSSION

The previous sections investigated the errors present in the model through comparing results to existing numerical and experimental results. It must be kept in mind that aerodynamic modeling of the wing assumes the model to be fully turbulent following from the investigation done in Section 5.1.3. The lack of any laminar region on the wing surface affects the pressure distribution. Additionally, when it comes to relating the upcoming results to full sized aircraft performance particularly the discrepancy in Reynolds number and Mach number should be kept in mind. The thicker boundary layer profile present in this research has a larger potential to be ingested into the propeller disk compared to configurations analyzed at higher Reynolds numbers. Drag coefficients presented in this study should be interpreted keeping in mind the Reynolds number of these simulations given the strong impact the Reynolds number has on the boundary layer profile and friction coefficient. Similarly, the Reynolds number of the propeller simulated has a strong impact on the propeller thrust and torque coefficients as can be seen in Figure 5.7. The relatively low mach numbers simulated in this configuration are a source of additional modeling error to be kept in mind when translating these results to full scale aircraft designs. Higher propeller mach numbers increase both the lift and drag coefficient of the airfoil on the blade experiencing high mach numbers, which will alter the propeller performance.

At similar operating conditions when comparing the numerical results to the experimental results, it was observed that the boundary layer profiles showed acceptable agreement to the experimental results from Figure 5.5. The propeller induced pressure distributions on the wing showed fair agreement to the experimental pressure distributions, but lacked the capability of predicting the downstream impact on the wing following the introduction of the propeller at high thrust settings, especially between 0.0 > X'/R > 1.0. At more moderate thrust coefficients ($C_T$ = 0.2) similar to the ones used in the upcoming results, the general behavior of the propeller induced pressure distributions are comparable to experimental results, but the peak pressure values are expected to vary following a overestimation of the upstream pressure peak of 28%.

The method fairs well in predicting the velocity fields downstream of the propeller in regions outside the boundary layer of the wing and nacelle geometries, but shows a lack in accurate prediction of the behavior close to the wall at a high thrust coefficient ($C_T$ = 0.35). The downstream region close to the wall where the boundary layer was observed to decrease in height was not observed in the numerical model, which shows potential for overestimation of the boundary layer thickness in the upcoming investigations. To more accurately capture this phenomenon a higher fidelity modeling approach (as presented by Sören [21]) is recommended to be performed when verifying the aerodynamic behavior of the flow in proximity to the wall.

# 6

# REFERENCE CONFIGURATIONS

This section describes the aero-propulsive performance of the two reference configurations. These configurations give better insight into the relative performance of the different geometry changes made in Section 7. The isolated performance of the propeller and the wing are described in Section 6.1. This section serves as a reference for the performance of all following OTW configurations and can be considered as the uninstalled propeller-wing configuration. The second reference configuration is denoted as the "baseline configuration" and serves as the initial condition for the OTW configuration sensitivity study. The baseline configuration geometry and aero-propulsive performance is described in Section 6.2

## 6.1. UNINSTALLED SYSTEM PERFORMANCE

A reference configuration used as a comparison of the performance of the OTW configuration is the combined performance of the uninstalled propeller at zero angle of attack and an isolated single wing subject to $P_C = 0.162$ and $C_L = 0.7272$ respectively. Section 6.1.1 highlights the performance of the uninstalled propeller and describes the sensitivity of this propeller to changing the propeller angle of attack and inflow velocity. Section 6.1.2 summarizes the combined performance of the propeller and the isolated wing and nacelle. Additionally, this section highlights the impact introducing a nacelle and a shroud has on the wing performance.

### 6.1.1. PROPELLER PERFORMANCE

The uninstalled propeller performance is summarized in Table 6.3. The uninstalled propeller efficiency equals $\eta_p = 0.800$, at a thrust coefficient of $C_T = 0.202$ ($T_C = 0.129$).

A visualization of the disk loading of the uninstalled propeller can be found in Figure 6.13a. The disk loading presented shows the normalized sectional thrust coefficient $T'_C$. The sectional thrust $T'$ is similarly defined as the sectional thrust coefficient $C_T$ related to the thrust coefficient $C_T$ defined in Equation 3.24. Normalizing the sectional thrust by the dynamic pressure and the propeller disk area as per Equation 2.5 results in the sectional thrust coefficient $T'_C$. The normalization by the dynamic pressure and propeller disk area (to obtain $T_C$) is selected for illustration of the disk loading instead of a normalization used in calculating the thrust coefficient $C_T$, since the advance ratio will differ between configurations. This in turn changes the rotational propeller velocity $n$ and therefore the normalization between configurations. The radial distribution of

Table 6.3: Uninstalled propeller performance

| Variable | value |
|---|---|
| $\eta_p$ | 0.7986 |
| $C_T$ | 0.202 |
| $C_Q$ | 0.0805 |
| $T_C$ | 0.129 |
| $P_C$ | 0.162 |
| $T$ | 4.10 N |
| $\beta_{07}$ | 45.9 deg |
| $J$ | 2.00 |

the sectional thrust coefficient $T'_{C,\text{net,axial}}$ is shown in Figure 6.13b, where the peak disk loading is found at 0.85 $r/R$.

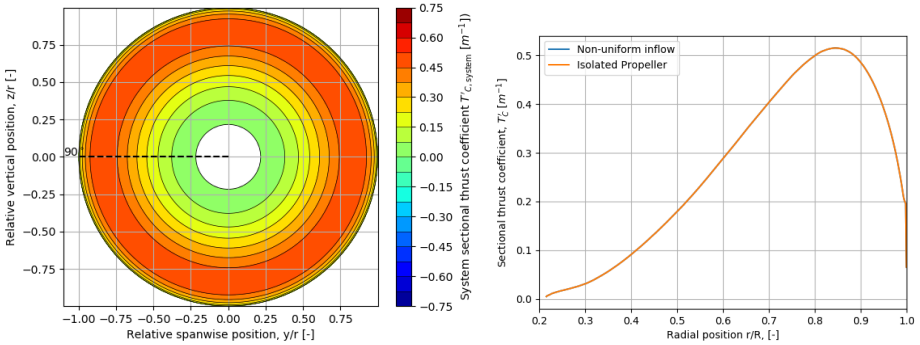


(a) Normalized disk loading

(b) Radial distribution at azimuthal location of 90 deg

Figure 6.13: Uninstalled propeller sectional net axial trust coefficient $T'_{C,\text{net,axial}}$

To give an idea on how the propeller performance is affected by changing inflow conditions, the performance of the propeller at an uniform angle of attack is evaluated. The propeller is evaluated at an advance ratio of $J$ = 1.8 and at a blade pitch angle of $\beta_{07}$ = 45 deg. With a constant inflow velocity of $V_\infty$ = 40.0 m/s, the propeller angle of attack is varied from -10.0 to 10.0 degrees. The efficiency, power coefficient and thrust coefficient are shown in figure Figure 6.14. The propeller efficiency of the propeller rises when moving away from $\alpha_p$ = 0.0 deg, as a result of the trust coefficient $C_T$ increasing relatively more than the $C_P$. The larger efficiency points to a larger trust being generated at a constant power coefficient, which is to be kept in mind in future analysis where the power coefficient is constrained. Another interesting aspect of the change in propeller angle of attack is the effect it has on the vertical in-plane force coefficient $C_{Z'}$. With increasing propeller angle of attack, the $C_{Z'}$ increases. This in-plane force matters while assessing the total trust contribution along the inflow velocity vector, since a the total

trust coefficient along inflow velocity vector is reduced by $C_{Z'} \cdot \sin\alpha_p$. This then results in a smaller propulsive efficiency when calculated along the inflow velocity vector when increasing the $\alpha_p$ away form 0 degrees. This is illustrated by observing the propulsive efficiency ($\eta_{p,sys}$) shown in Figure 6.14. $\eta_{p,sys}$ is calculated following the same reasoning as Equation 3.30 and calculates the efficiency along $V_\infty$ by including both the components of $C_{Z'}$ and $C_T$ along this axis. The propulsive efficiency along $V_\infty$ is maximum at $\alpha_p$ = 0 deg, stating that aligning the propeller rotation axis withe the incoming flow is most efficient in an isolated case.

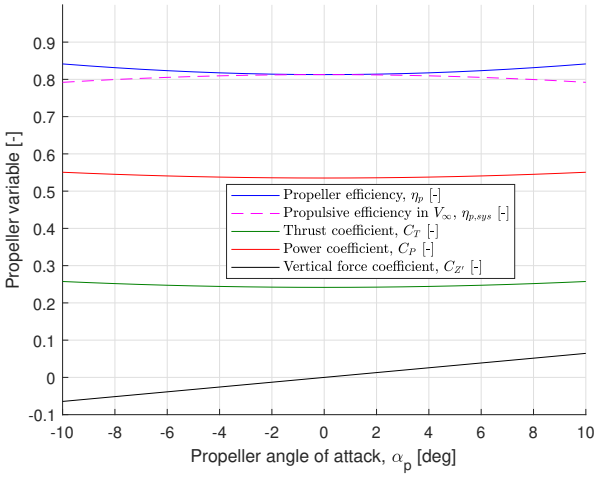


Figure 6.14: Propeller efficiency, thrust, power and vertical force coefficient for an uninstalled propeller at an angle of attack, $J$ = 1.8, $\beta_{07}$ = 45 deg

The propeller efficiency responds strongly to changing axial inflow velocity, as might be induced by the wing in a OTW configuration. To investigate the sensitivity to the changing inflow condition experienced by the propeller, the axial inflow velocity has been altered while keeping the $V_\infty$ constant. Figure 6.15 shows the effect on the propeller performance when varying the axial inflow velocity $V_a$. When increasing the $V_a$, both the thrust and power coefficients reduce as a result of the smaller angle of attack perceived by the propeller blade as a result of a higher perceived advance ratio $J_a$. This results in a lower propeller efficiency (as normalized with $V_\infty$) with increased $V_a$. Following this assessment, placing the propeller in an area with a large wing-induced velocity like at a suction peak, it is expected that the efficiency will drop. Similarly, if the inflow velocity is able to be reduced below $V_\infty$, an efficiency benefit is expected. To highlight the underlying propeller efficiency response to changing advance ratio, an additional propeller efficiency, as normalized by $J_a$ has been plotted. In this case, the propeller efficiency increases with increasing axial inflow velocity (and increasing advance ratio). The increase in efficiency with increasing $J_a$ can be explained by looking at the simulation showing the performance of the propeller following the supplied sensitivity maps in Figure 3.15, where at $J$=1.8, increasing the advance ratio increases the propeller effi-

ciency. The increase in efficiency is observed to be less steep than as observed with the efficiency calculated normalized with $V_\infty$.

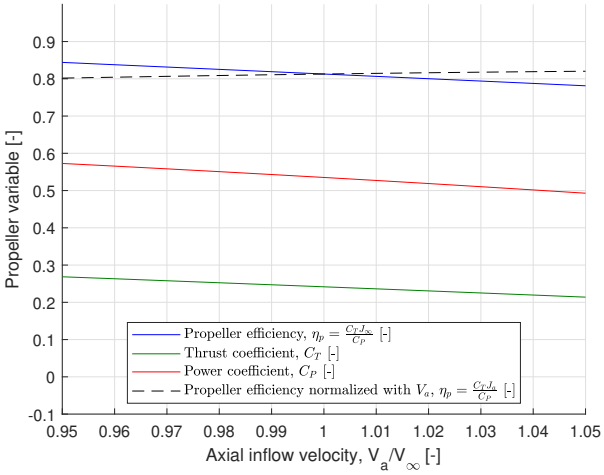


Figure 6.15: Propeller efficiency, thrust, power and vertical force coefficient for an uninstalled propeller with varying axial inflow velocity, $J = 1.8$, $\beta_{07} = 45$ deg

### 6.1.2. COMBINED PERFORMANCE

The isolated performance of the wing, nacelle and combined system (summation of isolated wing and nacelle performance) is summarized in Table 6.4. The wing at an angle of attack of 4.250 deg results in a lift coefficient of $C_L = 0.7272$ and drag coefficient of $C_D = 0.01251$. The pressure distribution of the isolated wing is shown in Figure 6.16. The drag coefficient of the nacelle $C_{D,\text{nacelle}} = 0.002227$ and the total system drag equals $C_{D,\text{system}} = 0.01474$ resulting in a lift-to-drag ratio of $C_L/C_D = 49.33$. With the uninstalled propeller efficiency of $\eta_\text{p} = 0.800$, the figure of merit for the reference uninstalled configuration is $C_L/C_D \cdot \eta_\text{p} = 39.40$. The isolated wing drag consists of 63.2 % friction drag and 36.8 % pressure drag.

The nacelle used in this study is designed for a wind tunnel model and therefore will be substantially larger than a nacelle used in a full scale aircraft design. For this reason, it's interesting to observe the impact of the nacelle on the solution and on the aerodynamic characteristics of the wing and propeller. The effect of adding the nacelle is illustrated by showing the mid-span pressure coefficient along the wing in Figure 6.17a. The nacelle is placed fitting with a propeller axial position of $x_\text{p} = 0.85$c and is installed with a 0 degree inclination to the chord line of the main wing. At this particular nacelle configuration, the presence of the nacelle increases static pressure on the wing upstream of the nacelle and decreases static pressure downstream.

Introducing the shroud geometry as defined in Table 3.2 into the domain results a change of pressure distribution the wing as shown in Figure 6.17b. It is observed that the shroud increases the pressure on the isolated wing upper surface at $0.3 < x/c < 1.0$.

Table 6.4: Isolated wing and system performance

| Variable | value |
|---|---|
| $C_L$ | 0.7272 |
| $C_{D,\text{wing,isolated}}$ | 0.01251 |
| $C_{D,\text{nacelle,isolated}}$ | 0.002227 |
| $C_{D,\text{system,isolated}}$ | 0.01474 |
| $C_L/C_D$ | 49.33 |
| $C_L/C_D \cdot \eta_\text{p}$ | 39.40 |
| $\alpha$ | 4.250 deg |
| Excess thrust | 1.464 N |

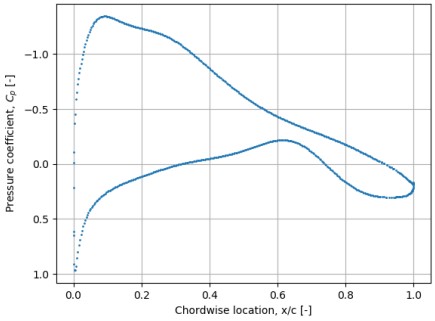


Figure 6.16: Isolated wing chord-wise pressure coefficient at $\alpha$ = 4.250 deg, $M$ = 0.1175, $Re$ = 2.6 e6

The increment in wing surface pressure is observed at around 0.7c, just upstream of the shroud geometry. Interestingly, a small increment in wing suction is observed at the leading edge of the wing, likely as a result of a change in the stagnation location of the wing. This wing-shroud configuration is set-up as a bi-planing configuration and the current orientation of these surfaces results in additional pressure observed between the two geometries when compared to the uninstalled performance of these specific wings.

## 6.2. BASELINE OVER-THE-WING CONFIGURATION

A baseline OTW configuration is defined in this section and is used in upcoming sections as a reference to analyze variations in design. The parameters defining the geometrical set-up of the model are summarized in Table 3.2, where Figure 3.3 gives further visual aid to these parameters.

An illustration of the flow field of the baseline configuration can be found in Figure 6.18. These figures show the total and static pressure coefficients at the mid-span location of the domain, where the $y' = 0$. The static pressure coefficient $C_p$ in Figure 6.18a shows the pressure distribution over the domain, where the static pressure distribution is dominated by the wing and shroud geometries. A relatively small pressure jump can be found over the propeller plane, following the low thrust coefficient selected in the cruise

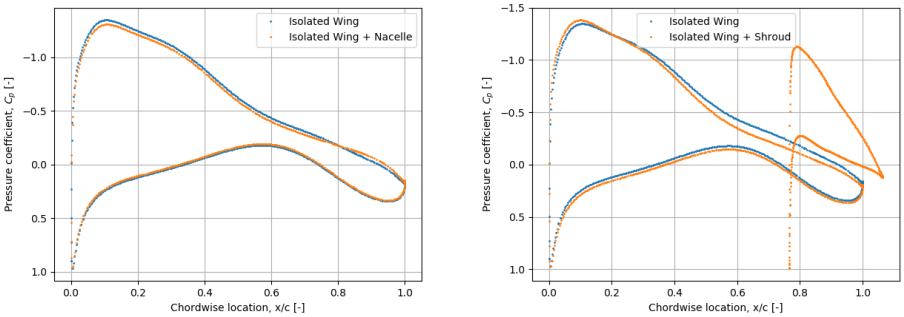


(a) Including Nacelle

(b) Including Shroud

Figure 6.17: Pressure coefficient along the isolated wing and wing including the shroud or nacelle at $\alpha$ = 4.25 deg

condition. The total pressure coefficient is shown in Figure 6.18b, where the momentum added into the system by the actuator disk is observed where the $C_{p,T} > 1$. As shown in Figure 6.20a, the highest propeller disk loading is found at an azimuthal location of 260 deg, which translates in the largest value of $C_{p,T}$ found downstream above the propeller when the swirl of the propeller rotates this flow counter-clockwise. Regions of lower total pressure $C_{p,T} < 1$ show the friction loss of the main wing, shroud and nacelle.

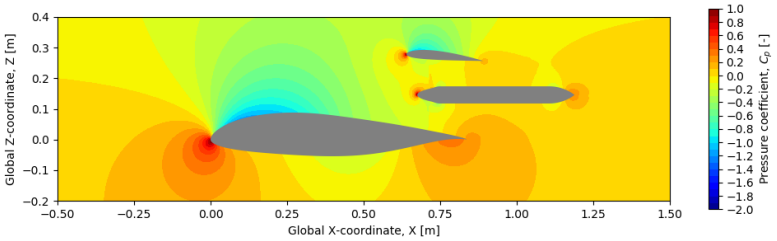


(a) Static pressure coefficient, $C_p$

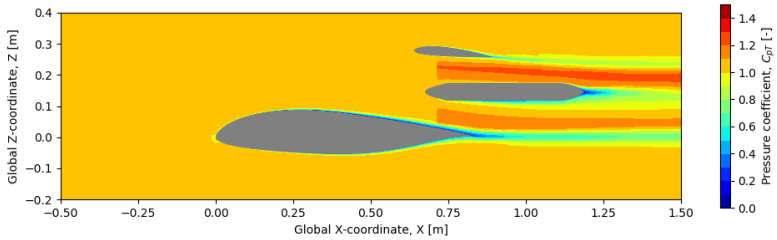


(b) Total pressure coefficient, $C_{p,T}$

Figure 6.18: Baseline configuration static and total pressure distributions at the domain mid-plane

The velocity components on the propeller plane are visualized in Figure 6.19. These plots show the propeller-off velocity fields as calculated by the first CFD simulation.

These velocity fields are then used for the propeller performance estimation. Figure 6.19b shows the normalized disk-normal axial velocity component ($V_a/V_\infty$). Firstly, the boundary layer of the main wing can be found at the bottom of the contour plot, where lower velocities are found. Lower axial velocities are also observed above the nacelle, as a result of the local downwards inflow field onto the nacelle. The inclination of the nacelle results in higher stagnation pressure on the upper part of the nacelle, which lowers the propeller plane normal axial velocity. A similar explanation can be given for the higher axial velocity below the propeller, as the inclination of the nacelle to the local flow vector increases suction and velocity below the nacelle. The upper part of the axial velocity field velocity is higher as a result of the suction of the shroud, which is placed at approximately the maximum thickness-to-chord location of the shroud airfoil. Figure 6.19a shows the propeller plane normal upwash fields as calculated by Equation 3.34 using the propeller plane normal velocity ($u'$) and propeller plane tangent vertical ($z'$) velocity ($w'$). This plot shows the upwash angle the propeller plane experiences. As Equation 3.34 shows, there is a large range of upwash angles the propeller experiences. In general, a downwash angle is experienced by the propeller by the local direction of the flow as a result of the main wing geometry. Close to the propeller nacelle a change in flow direction causes local upwash above the nacelle and additional downwash below the nacelle geometry. Most critical for the propeller performance is the local inflow as observed by the propeller blade. The largest changes in blade angle of attack are observed at the blade azimuthal locations of 90 deg and 270 deg, where the upwash angle most strongly affects the blade angle of attack. In the baseline configuration, the upwash angle at these azimuthal locations is around -7 deg increasing to almost -12 deg close to the nacelle as a result of acceleration of the flow at the span-wise extremes of the nacelle.

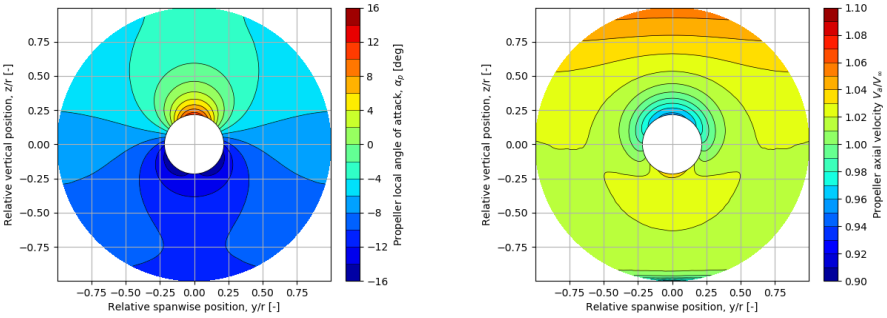


(a) Upwash angle

(b) Propeller axial velocity field $V_a/V_\infty$

Figure 6.19: Propeller-off propeller plane velocity fields of the baseline configuration

A visualization of the disk loading of the propeller of the baseline configuration can be found in Figure 6.20a. Similar to the plots displayed in the uninstalled propeller performance, these plots show the normalized sectional thrust coefficient $T'_C$. The downwash in the propeller plane results in additional thrust generated by the upwards moving propeller blade. Figure 6.20b shows the change in radial thrust to the isolated configuration. Due to a limitation of the model the thrust in the inboard section of the blade at an

azimuthal location of $\Phi = 90$ deg is overestimated. The local change in advance ratio in this area is out of bounds of the sensitivity map provided to the propeller performance estimation method resulting in an overestimation of the propeller performance in this region. This will affect the performance of geometries featuring a larger downwash angle to the propeller disk more, overestimating the thrust to a larger extent in these cases. The region affected only covers a relatively small portion of the total propeller thrust and therefore is not expected to have a significant impact on the final result, but at higher propeller angles of attack, this effect is to be kept in mind when interpreting the results.

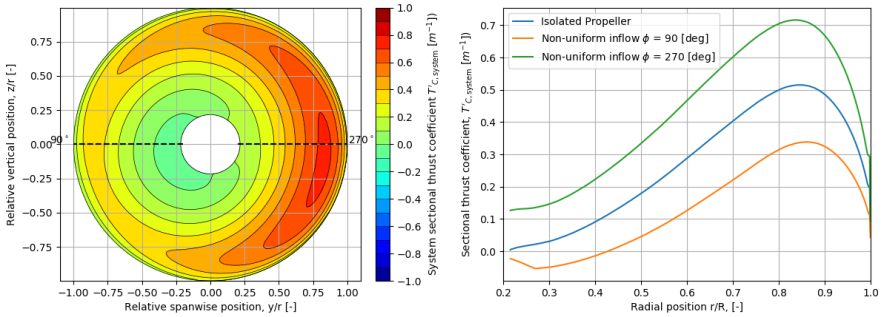


(a) Normalized disk loading

(b) Radial distribution at azimuthal location of 90 deg

Figure 6.20: Baseline configuration sectional net axial thrust coefficient $T'_{C,\text{net,axial}}$

The pressure coefficient of the baseline OTW configuration is compared to the pressure coefficient of the isolated wing at $C_L = 0.7272$ in Figure 6.21. The addition of the shroud results in additional lift being generated, which results in a lower angle of attack ($\alpha = 2.82$) needed to obtain the same lift coefficient (as normalized by the main wing chord length).

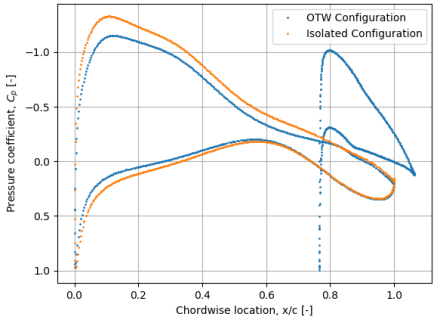


Figure 6.21: Baseline OTW configuration mid-span pressure coefficient at $C_L = 0.7272$, $M = 0.1175$, $Re = 2.6$ e6

The drag build up of the system is given in Figure 6.22. The majority of the drag is friction drag generated by the main wing. In this bi-planing configuration, the main

wing produces thrust while the inclination of the shroud produces the largest amount of pressure drag. As a result of the normal force of the shroud having a component in the drag direction, the pressure drag of shroud is largest.

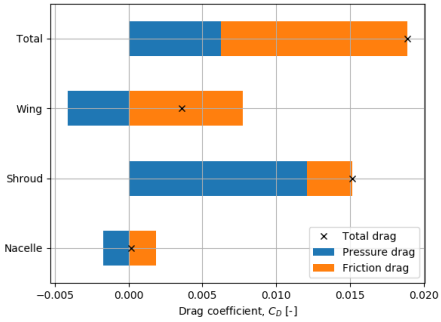


Figure 6.22: Baseline OTW configuration drag breakdown showing friction and pressure drag components of the individual geometries

The performance of the baseline configuration including and excluding a shroud geometry is summarized in Table 6.5. This table shows that the lift-to-drag ratio of the of the system reduces with the introduction of the propeller. The additional drag induced by the propeller outweighs the additional lift generated induced. This effect is more significant with the inclusion of a shroud geometry following a smaller benefit of the additional lift induced by the propeller compared to the un-shrouded configuration. The propeller efficiency when including the baseline shroud increases by 2.2%, but the total drag increases significantly with the inclusion of the shroud.

Table 6.5: Summary of baseline OTW performance including the un-shrouded baseline OTW performance and the uninstalled performance

| Configuration | $C_L/C_D$ | $\eta_{\text{system}}$ | $C_L/C_D \cdot \eta_{\text{system}}$ |
|---|---|---|---|
| Uninstalled | 49.52 | 0.7986 | 39.55 |
| Baseline OTW prop-off | 40.11 | - | - |
| Baseline OTW prop-on | 38.45 | 0.8141 | 31.30 |
| Un-shrouded OTW prop-off | 50.16 | - | - |
| Un-shrouded OTW prop-on | 49.80 | 0.7963 | 39.68 |

# 7

# SENSITIVITY ANALYSES

This chapter will describe the aero-propulsive performance impact of various design variables in a OTW configuration. This study is performed to give insight into the trends observed when varying the various parameters of the geometry which further increases understanding of the performance of an OTW propulsive configuration. To provide a comparison of the performance of these results, the performance of the upcoming geometry changes are compared to a reference configuration. The uninstalled system (uninstalled propeller + isolated wing and nacelle) performance previously described in Section 6.1, will be used as a reference for the system performance of the upcoming geometries. To be kept in mind is that the uninstalled reference case does not include a shroud and therefore the shrouded configurations inherently carry an additional drag penalty. The second reference configuration referred to in this chapter is the baseline OTW configuration as presented in Section 6.2, which is used to analyze changes in wing pressure distribution, propeller inflow and propeller loading.

To investigate the effect of changing the propeller orientation, a study into the propeller incidence is described in Section 7.1. From literature, the chord-wise propeller position is observed to change the OTW system performance significantly and therefore additional analysis into this parameter on the geometry used in this research is performed in Section 7.2. The amount of research done into the diameter-to-chord ratio in an OTW propulsive configuration is limited and therefore changing the diameter-to-chord ratio is analyzed in Section 7.3. The propeller tip clearance to the both the wing and the shroud is varied and the performance impact this has has been analyzed in Section 7.4. The inclusion of the shroud has a strong impact on the OTW system performance and therefore the incidence of the shroud is varied in Section 7.5. The chord length of the shroud is varied and performance impact is analyzed in Section 7.6 and the performance impact of the axial position of the shroud is analyzed in Section 7.7. The final sensitivity study analyzes the local wing shape below the propeller in Section 7.8. This section investigates if the combined system performance can be improved by a more synergistic orientation of the wing and propeller. The wing shape is varied in several steps to observe if the changes in geometry follow similar trends with larger departures. Finally a discussion reflecting on the results and looking forward to the future design and optimization studies is presented in Section 7.9.

## 7.1. PROPELLER INCIDENCE

The propeller incidence angle, defined as the angle between the wing chord and the direction normal to the propeller plane is varied from -6.0 deg to 10.0 deg. The resulting normalized propulsive efficiency, lift over drag ratio and figure of merit are shown in Figure 7.23.

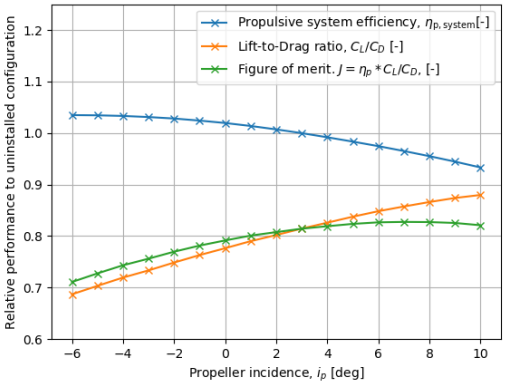


Figure 7.23: Change in performance as result of variation of propeller incidence $i_{\text{propeller}}$

The efficiency favors lower propeller incidence angles, where the local inclination of the propeller increases the downwash onto the propeller plane resulting in a more negative propeller angle of attack. To understand what drives this behavior, the axial inflow and downwash fields of a propeller at $i_{\text{propeller}}$ = 6 deg are compared to the baseline configuration ($i_{\text{propeller}}$ = 0 deg) in Figure 7.25. At this propeller inclination, the axial inflow velocity to the propeller reduces below the propeller ($\phi$ = 180 deg) and increases above the propeller ($\phi$ = 0 deg). The flow around the nacelle is more aligned compared to the baseline OTW configuration as the axial velocity is closer to $V_\infty$ at r/R = 0.2. A large part of the change in axial velocity in the propeller plane can be attributed to the change in angle of attack of the nacelle given that the changes in inflow velocity are largest near the nacelle, which can be further confirmed by looking at the velocity contour in Figure 7.24a. The increase in axial velocity above the propeller is expected to contribute to the reduction of efficiency following the investigation in Section 6.1.1.

At $i_{\text{propeller}}$ = 6 deg the inflow to the propeller is more aligned to the propeller axis and the upwash angle at $\phi$ = 270 deg is reduced to about -1 deg, which means that the change in thrust compared to the uninstalled propeller as a result of a change in tangential advance ratio $\Delta J_t$ is relatively small. From the investigation done on a propeller under a angle of attack in Section 6.1.1, reducing the $\alpha_{\text{propeller}}$ will reduce the propeller efficiency $\eta_{\text{p}}$ and propeller vertical force coefficient $C_{Z'}$.

The more uniform inflow field as compared to the baseline OTW configuration then results to a more uniform thrust distribution around the disk as observed in Figure 7.26a. The radial sectional thrust distributions therefore show distributions closer aligned to the isolated thrust distributions as shown in Figure 7.26b.

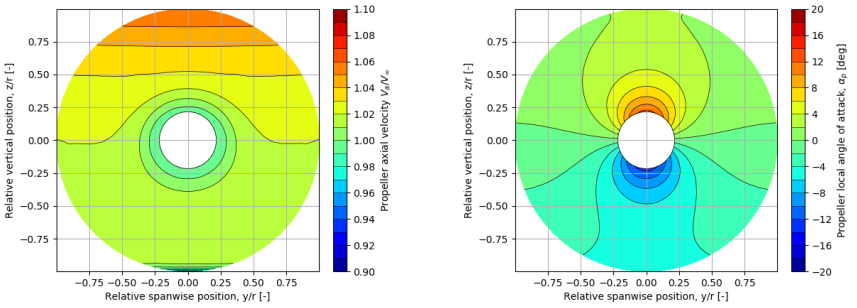


(a) Normalized axial flow velocity

(b) Upwash angle

Figure 7.24: Propeller-off propeller plane velocity fields at $i_{\text{propeller}}$ = 6 deg

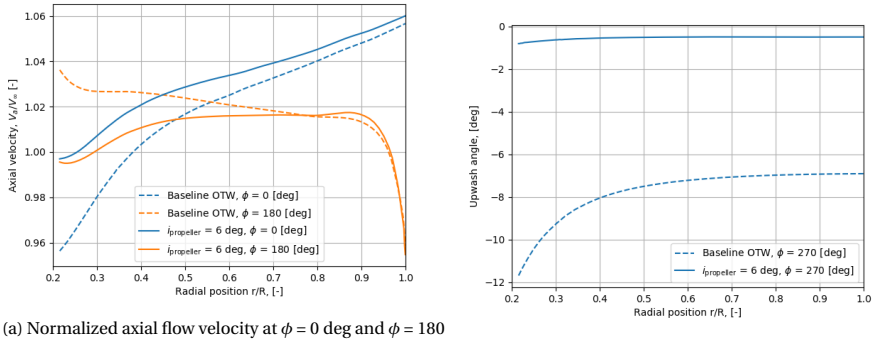


(a) Normalized axial flow velocity at $\phi$ = 0 deg and $\phi$ = 180 deg

(b) Upwash angle at $\phi$ = 270 deg

Figure 7.25: Radial velocity profiles at $i_{\text{propeller}}$ = 6 deg compared to the baseline OTW configuration at $i_{\text{propeller}}$ = 0 deg

To understand why the optimal propeller efficiency is not located where the inflow is most uniform, the propeller forces normal to the propeller plane and in-plane ($F_{Z'}$) are analyzed compared to these forces in an uninstalled propeller under an angle of attack at constant propeller power coefficient. The components of these two forces along the $V_\infty$ vector are computed, to show how much each of them contributes to the system efficiency of the system. This decomposition of forces is further illustrated in Figure 3.18. Both the propeller vertical force ($F_{Z'}$) and propeller thrust ($T$) contribute towards the net axial propeller force ($T_{net,axial}$) when the propeller is inclined to the direction of flight (i.e. has a nonzero $\alpha_{\text{propeller}}$). The normalized net axial propeller force ($T_{C,net,axial}$) is plotted together with the thrust contribution to the normalized propeller force ($T_C \cdot \cos(\alpha_p)$) in Figure 7.27, where $T_{C,net,axial} = T_C \cdot \cos(\alpha_p) - F_{Z',C} \cdot \sin(\alpha_p)$. The difference between these two graphs will be the contribution of the in-plane vertical force $F_{Z',C} \cdot \sin(\alpha_p)$. These are plotted for both the OTW and an uninstalled propeller at constant power coefficient to highlight the differences. For the uninstalled propeller under

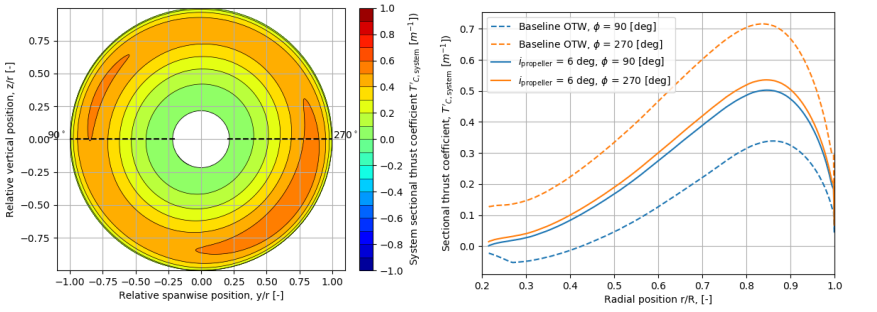


(a) System sectional net axial thrust coefficient $T'_{C,net,axial}$

(b) Radial sectional thrust coefficient $T'_C$ at $\phi = 90$ and $\phi = 270$

Figure 7.26: Radial velocity profiles at $i_{\text{propeller}} = 6$ deg compared to the baseline OTW configuration at $i_{\text{propeller}} = 0$ deg

an angle of attack, an increase in angle of attack comes with both an increase in propeller in plane vertical force ($F_{Z'}$) and propeller thrust ($T$). Decomposing the forces and computing the net axial thrust in direction of flight ($T_{net,axial}$), the maximum net axial thrust is found at a propeller angle of attack of 0 degrees. The in-plane vertical force counters the additional propeller plane normal thrust obtained from increasing the angle of attack as previously described in Section 6.1.1. In the OTW configuration however, with the wing under an angle of attack, the wing circulation increases downwash onto the propeller plane. At a 0 deg propeller angle of attack, the OTW propeller thrust is increased as a result of the angle of attack induced by the wing's flow field, without being penalized by in plane propeller forces.

Unlike in the isolated condition, increasing the propeller angle of attack in the OTW configuration results the propeller vertical force contributing to the net axial thrust, since the net axial thrust is larger than only the thrust component $T\cos\alpha_p$. This effect originates from the negative inflow angle into the propeller following the downwash provided by the wing, resulting in a component of the vertical propeller force vector pointing in the direction opposite to the drag vector. The propeller thrust however still drops with increasing $\alpha_p$ given that the out of plane trust gained by the propeller decreases when the inflow angle to the propeller reduces and the flow into the propeller gets more aligned. When looking at high propeller angle of attack values, the contribution of $F_{Z'}$ reaches zero at around $\alpha_p = 9$ deg.

Although the propeller favors lower propeller inclinations, the drag of the system increases when reducing the propeller inclination. This is likely due to the propeller force vector contributing less to the lift vector at a lower propeller inclination. This then requires the angle of attack of the system to increase, increasing the drag of the system. The relative change in the drag contributions of the geometry components is shown in Figure 7.28a, where it's observed that the largest contribution towards the drag is pressure drag. The nacelle in this case has a particularly strong response, which is likely due to its angle of attack changing when changing the propeller inclination. Both the wing

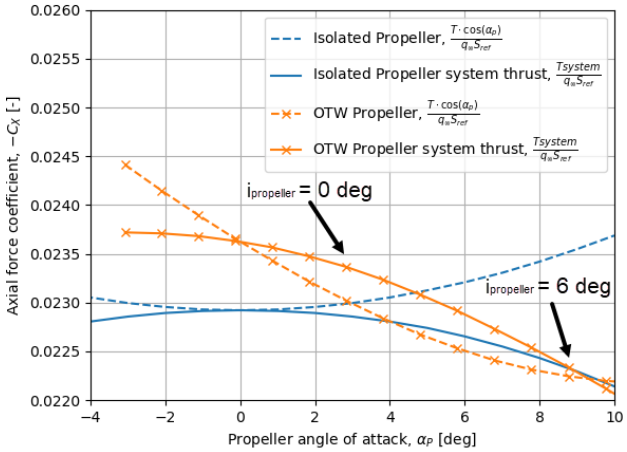


Figure 7.27: Change in axial propeller force as result of variation of propeller incidence

and shroud drag reduce with increasing propeller incidence.

To investigate this effect on pressure drag, the mid-plane pressure coefficient is shown in Figure 7.29. The increment of propeller incidence show a small reduction to the suction provided on the wing and sees the geometry of the shroud moving backwards. Other than this, the the pressure distribution is relatively similar to the baseline OTW configuration. The reduction of angle of attack does mean that the normal force vector on the wing and shroud have a smaller component pointing in the direction of drag, where the change in system angle of attack is about 0.008 degrees per degree of propeller incidence.

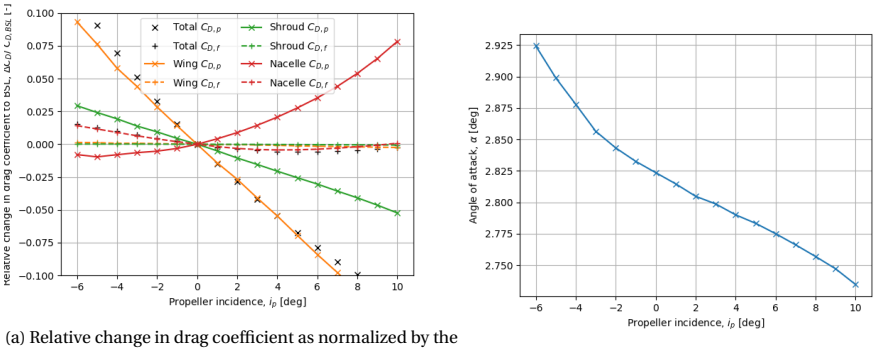


(a) Relative change in drag coefficient as normalized by the baseline drag coefficient

(b) Variation in system angle of attack

Figure 7.28: Effect on system performance on the drag contributions and angle of attack of the system by changing the propeller incidence angle

An additional component to the increased drag observed at lower propeller inclina-

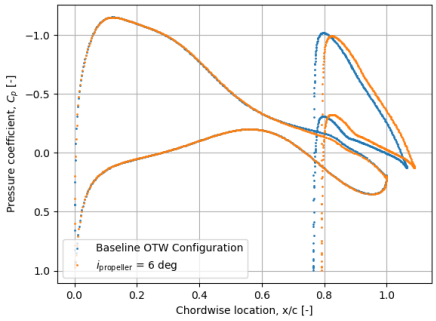


Figure 7.29: Wing and shroud pressure coefficient at $i_{\text{propeller}} = 6$ deg compared to the baseline OTW configuration where $i_{\text{propeller}} = 0$ deg

tions is the strong increment in pressure drag following the introduction of the propeller as observed from Figure 7.30b. This when the $\Delta C_L$ is relatively unchanged as shown in Figure 7.30a.

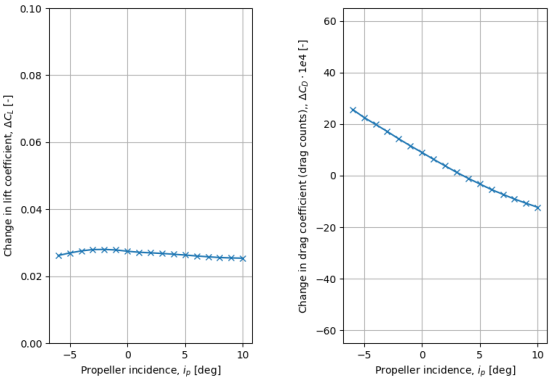


(a) Lift coefficient

(b) Drag coefficient

Figure 7.30: Change in lift and drag coefficient with $P_C = 0.162$ to propeller-off $P_C = 0$ at different propeller inclinations

## 7.2. PROPELLER POSITION

The propeller chord-wise position has been varied from $X_p/c = 0.15$ to $X_p/c = 0.9$. Moving the propeller implies moving the shroud position with the propeller to maintain constant tip clearance to the shroud and constant relative position to the shroud chord-wise position. The shroud incidence is unchanged while moving the propeller, which can result in sub-optimal shroud inclination due to the changing perceived angle of attack of the shroud.

Due to a limitation to the pitch correction applied in this method, the propeller efficiency in the region between $X_p/c = 0.3$ to $X_p/c = 0.7$ is sub-optimal. As a result of the increase in axial velocity induced by the wing, the optimal blade pitch reduces. After hitting the bounds of the bounded propeller efficiency optimization, the constant propulsive power coefficient is achieved by varying just the advance ratio at the bounded propeller pitch. In the region between $X_p/c = 0.3$ to $X_p/c = 0.7$, this means that the resulting propeller efficiency is slightly lower than optimal.

Moving the chord-wise position of the propeller has a significant effect on both the propulsive efficiency and the lift-to-drag ratio of the system. Similar to the trends observed by Marcus [7], the propulsive efficiency with the propeller moving upstream to a lower $X_p/c$. The magnitude of the reduction in efficiency is however lower than observed by Marcus [7], which can be attributed to the variable pitch applied in this method. The lift to drag ratio is observed to be optimal at around 0.4c to 0.5c, being slightly more downstream than observed by Johnson and White [4] who found a maximum $C_L/C_D$ at $X_p/c = 0.2$c. The results by Johnson and White modeled a three-surface regional transport configuration and tested a handful of propeller axial locations, which can explain the different location of maximum $C_L/C_D$. The inclusion of the shroud does seem to affect the location of maximum lift-to-drag ratio, moving it slightly upstream, given that the un-shrouded maximum lift to drag ratio is found to be at 0.3c.

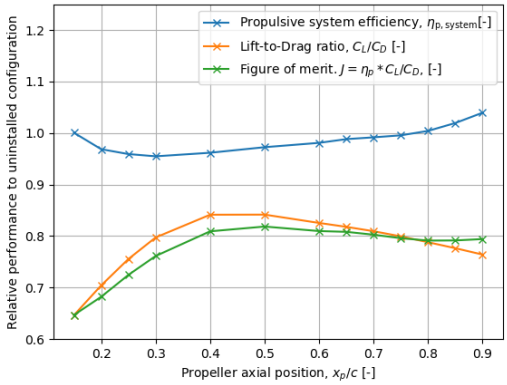


Figure 7.31: Change in performance as result of variation of propeller chord-wise position $X_p/c$

To highlight the impact of the propeller on the lift to drag ratio, the difference in lift an drag coefficients as a result of introducing the propeller are shown in Figure 7.32. It shows the largest increment in lift found at a propeller placed at $X_p/c = 0.65$c. Comparing this trend to literature [5, 7], it is observed that the $\Delta C_L$ generally is observed to increase with increasing $X_p/c$. The inclusion of the shroud does play a significant role in the trend observed in Figure 7.32a as the un-shrouded $\Delta C_L$ trend follows the trend previously observed in literature [5, 7], finding the largest $\Delta C_L$ at the trailing edge. The added suction in front of the propeller is maximized when moving the propeller downstream along the chord of the wing. The propeller impact on drag is shown in Figure 7.32b, where the

largest reduction in $\Delta C_D$ is found at $X_p/c = 0.4$c. This is slightly upstream of the location observed by Marcus [7], but it follows a similar trend as observed previously in literature [4, 5, 7]. The shroud again seems to have a effect on the location of minimum $\Delta C_D$ as observed by the un-shrouded simulation results shown in Figure 7.33b, where the location of minimum $\Delta C_D$ is found at 0.3c, which coincides with the thickest point of the wing. This confirms earlier conclusions stating that the suction in front of the propeller and higher pressure behind the propeller reduces the pressure drag of the wing. Additionally, the inclusion of the shroud reduces the observed reduction in pressure drag by around a factor of 2.

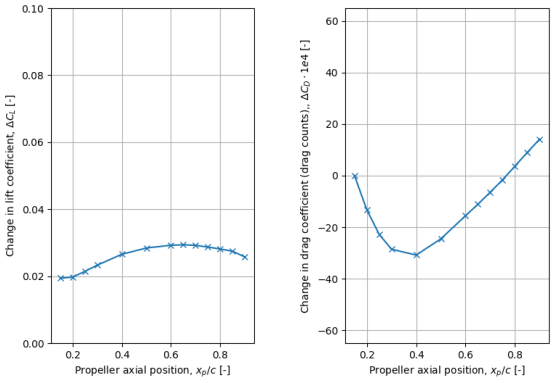


(a) Lift coefficient (b) Drag coefficient

Figure 7.32: Change in lift and drag coefficient with $P_C = 0.162$ to propeller-off $P_C = 0$ at different chord-wise propeller locations

The observations on the $\Delta C_L$ and $\Delta C_D$ are further highlighted by looking at the un-shrouded pressure profiles of a downstream propeller location ($X_p/c = 0.85$) and an upstream propeller location ($X_p/c = 0.3$) in Figure 7.34. The additional suction is observed to propagate upstream of the propeller location. The change in pressure coefficient is larger at $X_p/c = 0.3$, but this is applied over a smaller area and therefore with a lower $\Delta C_L$. The largest drag reduction at $X_p/c = 0.3$ is explained by looking at Figure 7.34b, where all the suction is added upstream of the point of maximum thickness and therefore acts to reduce the pressure drag on the wing. The un-shrouded OTW configuration shows significant improvements to the lift to drag ratio at $X_p/c = 0.3$, following the significant reduction in $\Delta C_D$. At $X_p/c = 0.3$, the un-shrouded configuration shows an increment in lift-to-drag ratio of 45.5% compared to the uninstalled configuration.

## 7.3. PROPELLER DIAMETER-TO-CHORD RATIO

Not a lot of previous investigation has been performed to analyze the trends following varying the propeller diameter-to-chord ratio $D_p/c$ in OTW configurations. The nature of this parameter makes it mainly suitable for numerical investigation. Looking at the complete aircraft system, this parameter is likely to play a significant role in the complete

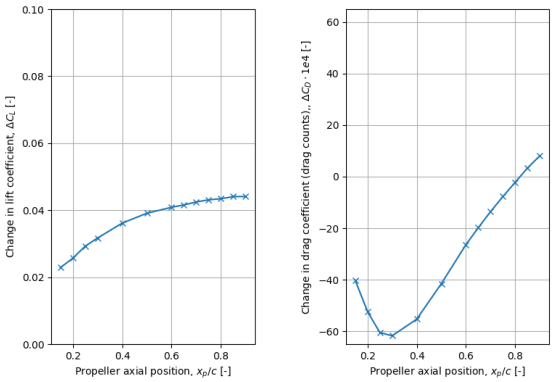


(a) Lift coefficient

(b) Drag coefficient

Figure 7.33: Change in lift and drag coefficient with $P_C = 0.162$ to propeller-off $P_C = 0$ at different chord-wise propeller locations in the un-shrouded configuration

aircraft design. Marcus [7] performed numerical simulations investigation the diameter-to-chord ratio in a OTW configuration, with a propeller placed at $X_p/c = 0.95$ at constant $T_C$ and constant $C_L$. Marcus [7] observed an increase in $\Delta C_L$ with a reduction of $D_p/c$ and increased $\eta_p$, while observing minimal change in $\Delta C_{D,p}$. The larger $\Delta C_L$ was attributed the top of the propeller being closer to the wing surface and therefore inducing larger changes to the wing pressure distribution [7]. The increase in wing induced inflow angle contributes to the increase in propeller efficiency [7].

In this study, due to the limited availability of the propeller sensitivity maps the propeller diameter is kept constant. Keeping this limitation in mind, to better assess the diameter-to-chord ratio, a simulation solely featuring the main wing and the actuator disk has been run to eliminate variations in geometry like relative shroud position. The limitation of changing the chord length to assess the diameter-to-chord ratio means the variation comes with a change in Reynolds number. This will affect the drag of the system considerably as observed by running an isolated wing at different chord lengths at constant $V_\infty$ (thus different Reynolds numbers). This must be kept in mind when analyzing the results. The lift coefficient and power coefficient are kept constant in this study, which does mean that the total lift of the system reduces with a reduction in chord and therefore increment of $D_p/c$. Figure 7.35 shows the summary of the variation of $D_p/c$, where the $D_p/c$ used in the isolated and baseline configuration is equal to 0.242. The absolute lift-to-drag ratio as normalized by the uninstalled configuration (which does include the nacelle) is higher in this figure following from not including the nacelle in these simulations.

The effect of changing the the diameter-to-chord ratio shows a slight increase in propeller efficiency with decreasing $D_p/c$ as shown in Figure 7.35. The total lift-to-drag ratio has a preference to the smaller $D_p/c$, but this is largely due to the increasing Reynolds number with reducing $D_p/c$, which in turn reduces the drag coefficient. To observe how

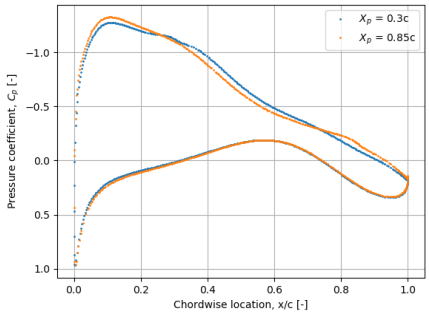


(a) $X_p/c = 0.3$ vs $X_p/c = 0.85$, $P_C = 0.162$

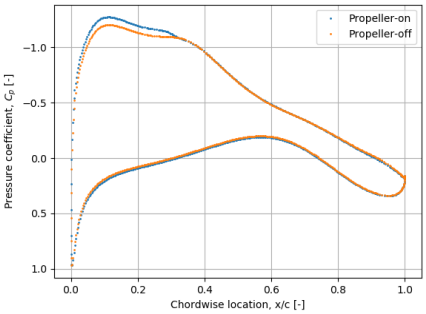


(b) $X_p/c = 0.3$, $P_C = 0.162$ vs $P_C = 0$

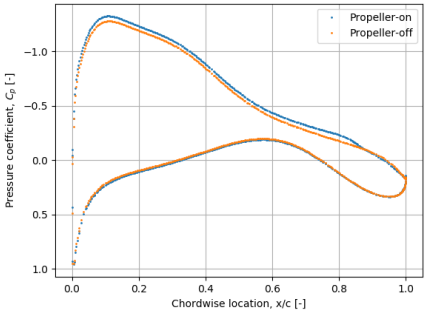


(c) $X_p/c = 0.85$, $P_C = 0.162$ vs $P_C = 0$

Figure 7.34: Chord-wise pressure profiles at $X_p/c = 0.3$ and $X_p/c = 0.85$ of an un-shrouded OTW configuration

the propeller impact on lift and drag changes, the change in lift and drag coefficient of the propeller-off to the propeller-on condition are shown in Figure 7.36b. An increase in $\Delta C_L$ and a decrease in $\Delta C_D$ is found with increasing $D_p/c$. The increase and reduction of drag results from slightly more suction present upstream of the propeller at higher $D_p/c$ as can be seen by the pressure distributions presented in Figure 7.37. For a given span, a larger $D_p/c$ results in less propellers spanning the OTW propeller array. Compared to the investigation done by Marcus [7], the $\Delta C_L$ trend observed is opposite, which could be a result of the different modeling approaches. In this study, the propeller power coefficient $P_C$ as normalized by the span and diameter (both constant) is constrained, while the total lift decreases with increasing $D_p/c$ (keeping constant $C_L$). The larger thrust to lift ratio at larger $D_p/c$ can be a reason for the found increase in $\Delta C_L$ and reduction in $\Delta C_D$.

Increasing the $D_p/c$ reduces the propulsive efficiency as shown in Figure 7.35, which agrees with the trend found by Marcus [7]. Similar to the observations made by Marcus, increasing the $D_p/c$ reduces the downwash angle as observed by the propeller as a result of the top of the propeller being further away from the wing surface and therefore downwash field as can be seen from Figure 7.38b. This reduced downwash reduces the

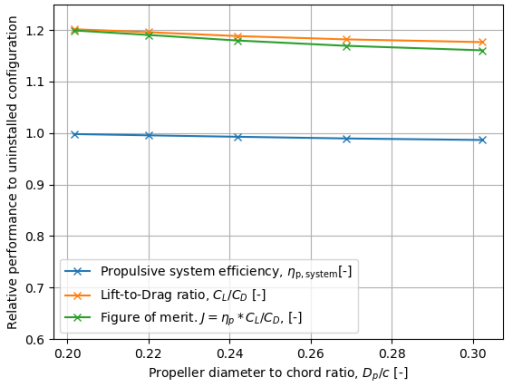


Figure 7.35: Change in performance as result of variation of propeller diameter to chord ratio $D_p/c$, by varying the chord length in an un-shrouded configuration without nacelle

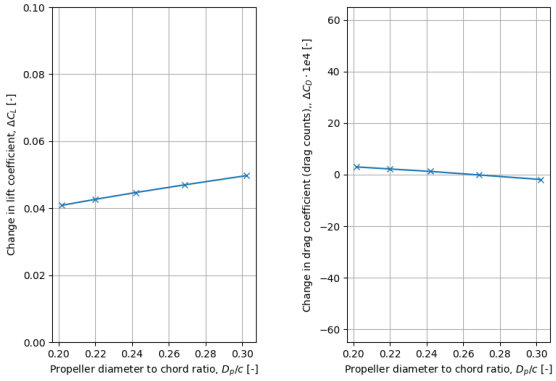


(a) Lift coefficient

(b) Drag coefficient

Figure 7.36: Change in lift and drag coefficient with $P_C = 0.162$ to propeller-off $P_C = 0$ at different values of diameter-to-chord in the un-shrouded configuration

efficiency benefit as described in Section 6.1.1.

A fairer way of modeling the aerodynamics of the system would be to constrain the total lift given a constant span and a constant total axial thrust and then varying the amount of propulsors on that given span to assess the system performance. One example of this is the work performed by Wick et al. [57] assessing the benefits of several integrated distributed propulsion configurations.

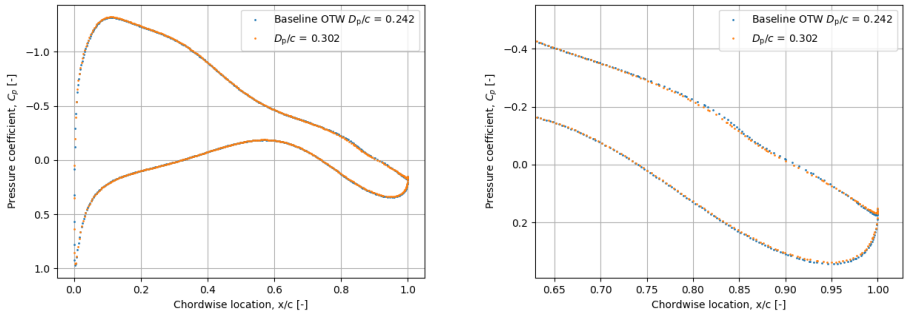


(a) Pressure coefficient distribution

(b) Local pressure coefficient distribution

Figure 7.37: Pressure coefficient of the un-shrouded baseline without nacelle at ($D_p/c = 0.242$) and at a larger diameter-to-chord ratio ($D_p/c = 0.302$) at constant $P_C = 0.162$ and $C_L = 0.7272$

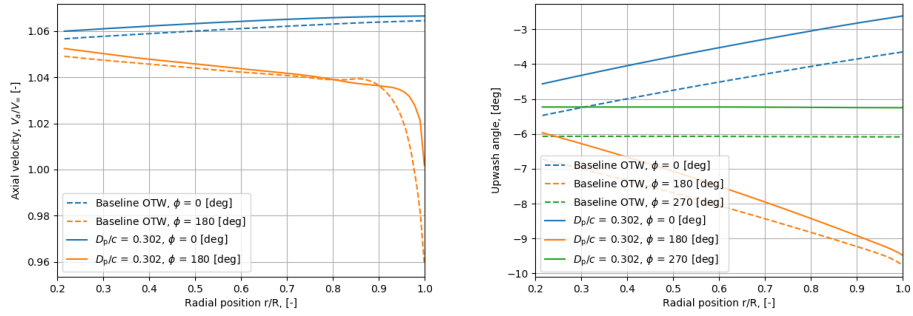


(a) Radial distribution of axial inflow

(b) Radial distribution of upwash angle

Figure 7.38: Radial velocity distributions at specific azimuthal locations of the un-shrouded baseline without nacelle at ($D_p/c = 0.242$) and at a larger diameter-to-chord ratio ($D_p/c = 0.302$) at constant $P_C = 0.162$ and $C_L = 0.7272$

## 7.4. PROPELLER TIP CLEARANCE

The propeller tip clearance has been varied from $\epsilon/D_p = 1.75\%$ to $\epsilon/D_p = 28\%$, where the baseline OTW configuration is set to $\epsilon/D_p = 7\%$. The propeller tip clearance is varied for both the tip clearance to the wing and to the shroud. Therefore, reducing the tip clearance moves the nacelle closer to the wing and moves the shroud closer to the nacelle and therefore the shroud moves closer to the wing, given that both the upper and lower propeller tip clearances are both changed simultaneously. The impact of changing the propeller tip clearance on the propulsive efficiency and lift to drag ratio is found to be relatively small. The propulsive efficiency is observed to increase with reducing tip clearance, where at the lowest tip clearance ($\epsilon/D_p = 1.75\%$). The slight increment of propulsive efficiency with decreasing tip clearance is in disagreement with results from the OTW channel wing study from Müller et al. [25], where the propeller efficiency is

observed to decrease with decreasing tip clearances. The channel wing will have a larger impact on the propeller performance given that this embedded propeller has a closer proximity to the wing for a significantly larger range of azimuthal positions. The increment of efficiency is very small and by looking at the azimuthal efficiency distribution in Figure 7.40, reduces slightly on the downwards moving blade and increases when the blade is closest to the wing surface. The increment in efficiency at $\phi$ = 180 deg follows from the propeller tip intersecting more of the wing boundary layer increasing its thrust following a lower inflow velocity, which can be observed from looking at Figure 7.41. Reducing the tip clearance at this axial position has the added effect of slightly reducing the downwash onto the propeller, which can be a reason for the slightly reduced efficiency at the other azimuthal locations.

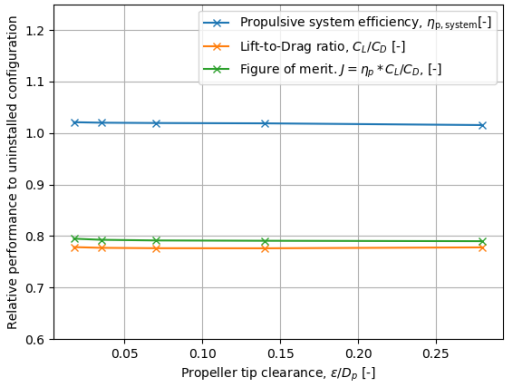


Figure 7.39: Change in performance as result of variation of propeller tip clearance $\epsilon/D_p$

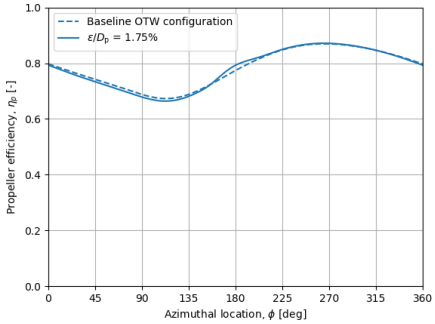


Figure 7.40: Change in propeller efficiency along the azimuthal location as result of variation of propeller tip clearance from $\epsilon/D_p$ = 7% to $\epsilon/D_p$ = 1.75%

The difference in lift an drag coefficients as a result of introducing the propeller at varying propeller tip clearances are shown in Figure 7.42. Interestingly, the relation be-

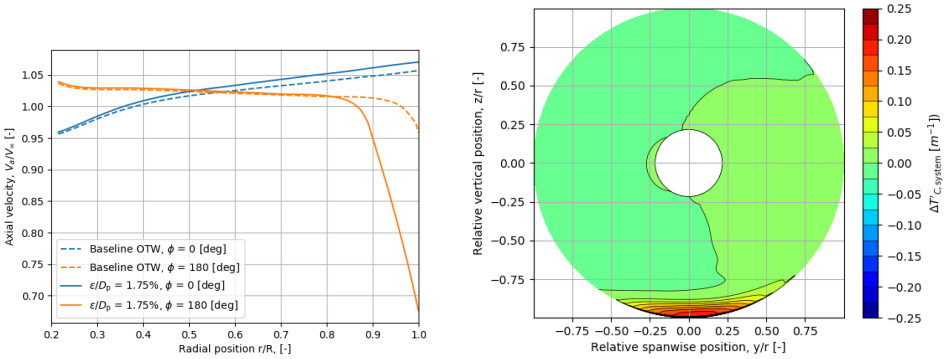


(a) Radial axial velocity distributions

(b) Change in net axial thrust coefficient

Figure 7.41: Change in radial axial velocity and change in net axial thrust when reducing the propeller tip clearance ($\epsilon/D_p$ = 1.75%) as compared to the baseline OTW configuration($\epsilon/D_p$ = 7%)

tween the tip clearance and propeller change in lift coefficient seems to increase exponentially at small tip clearances and linearly at higher tip clearances. This $\Delta C_L$ behavior, does show similarities to the results from the OTW channel wing study from Müller et al. [25] when varying the propeller tip clearance in a OTW channel wing configuration. The wing and shroud pressure coefficient of the lowest tip clearance ($\epsilon/D_p$ = 1.75%) is compared to the baseline OTW configuration in Figure 7.43, to see how the change in $\Delta C_L$ results from the changed pressure distribution over the wing. With the propeller located at 0.85c, the reduction in tip clearance increases the suction on the wing locally upstream of the propeller. Additionally, the propeller induced suction on the pressure surface of the shroud increases. This additional suction at the propeller location are in agreement to the OTW channel wing study from Müller et al. [25], where decreasing the propeller tip clearance increases the suction peak on the wing geometry. The $\Delta C_D$ shows a small sensitivity to the tip clearance favoring higher tip clearances. It's important to keep in mind the axial position of the propeller when observing the $\Delta C_D$ trends as the propeller impact on the drag changes significantly at different propeller chord-wise positions as observed in Section 7.2. Previous exploratory experimental investigation to OTW propeller tip clearance on a two propeller three-surface regional transport configuration as performed by Johnson and White [4] confirms this, showing small sensitivity to $\Delta C_D$ at a propeller positioned at the trailing edge of the wing ($X_p/c = 0.8$), but larger sensitivity at a more upstream propeller chord-wise position ($X_p/c = 0.2$ and $X_p/c = 0.4$). At these upstream propeller chord-wise positions, the increased suction introduced by the propeller reduces the pressure drag of the wing, and bringing the propeller closer to the wing surface enhanced this benefit. Johnson and White observed the largest drag reduction to be at $\epsilon/D_p$ = 3%, being the lowest tip clearance evaluated. The trend of increasing favorable effects seen when reducing the tip clearance were also found by Putnam [58] when experimentally reducing the tip clearance of an OTW blown jet configuration where the tip clearance was reduced from $\epsilon/D_p$ = 1.5 to $\epsilon/D_p$ = 0.75. To confirm this

mechanism and the observations by Johnson and White and Putnam, a un-shrouded tip clearance study is performed, placing the propeller at a more upstream chord-wise position of ($X_p/c = 0.3$). The impact on the lift and drag coefficients by introducing the propeller are shown in, Figure 7.44, simulating an un-shrouded variation of tip clearance at a chord-wise position of $X_p/c = 0.3$. The initial observation when looking at the $\Delta C_D$, is that at this chord-wise position, the propeller reduces the drag on the wing and does this to a greater extent as when the system includes a shroud. Secondly, the impact on drag now shows increasing drag reduction with decreasing tip clearance similar to the observations from Johnson and White [4].

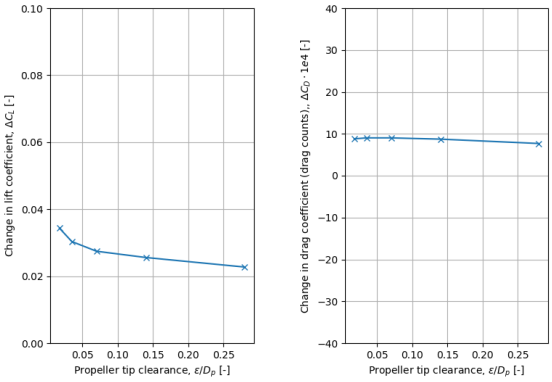


(a) Lift coefficient (b) Drag coefficient

Figure 7.42: Change in lift and drag coefficient with $P_C = 0.162$ to propeller-off $P_C = 0$ at different tip clearances

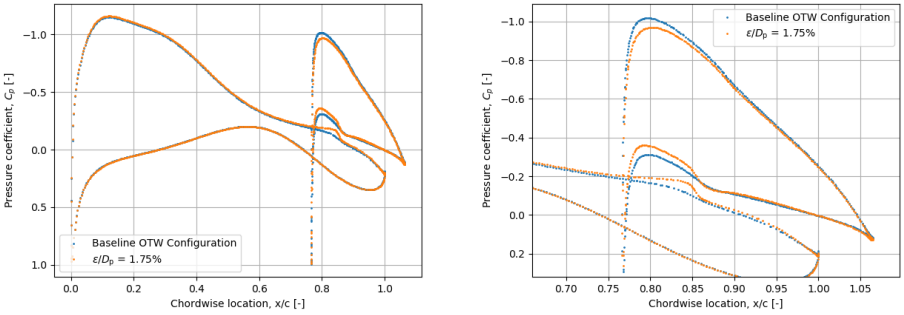


(a) Pressure coefficient (b) Shroud Pressure coefficient

Figure 7.43: Pressure coefficient of baseline OTW configuration ($\epsilon/D_p = 7\%$) and small tip clearance ($\epsilon/D_p = 1.75\%$)

As a final note, the optimal propeller tip clearance will likely be constrained by ad-

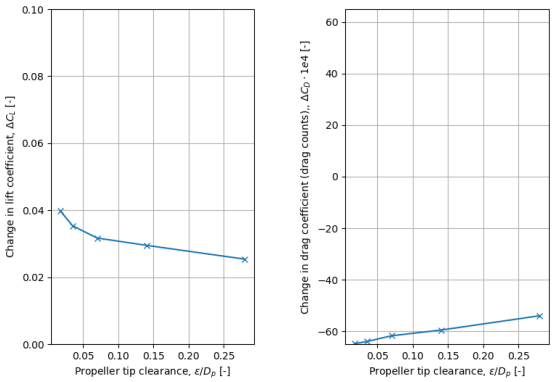


(a) Lift coefficient (b) Drag coefficient

Figure 7.44: Change in lift and drag coefficient with $P_C = 0.162$ to propeller-off $P_C = 0$ at different tip clearances, for an un-shrouded OTW configuration at $X_p/c = 0.3$

ditional structural and aerodynamic effects not taken into account in this study. Unsteady aerodynamic effects of the propeller tip intersecting with the boundary layer can be detrimental to the wing boundary layer, especially in adverse pressure gradients when deploying a flap as investigated by de Vries et al. [20] and Müller et al. [25]. At lower tip clearances, the unsteadiness of the propeller blade loading will increase, making the unsteadiness of the system more important to evaluate. The impact on the structural design of the blades will also play a role with this varying propeller loading.

## 7.5. SHROUD INCIDENCE

The shroud incidence angle is varied to observe the effect of changing the inflow to the propeller by changing the velocity field induced by the shroud. Figure 7.45 shows the sensitivity to changing the shroud incidence angle, illustrating the impact on propulsive efficiency and system lift-to-drag. The lower propulsive system efficiency spotted in $i_{\text{shroud}}$ = -3 deg is a result from the propeller performance optimization loop converging to a slightly lower efficiency compared to the ideal configuration and it is assumed this is an artifact of a modeling error instead of an aerodynamic response.

The system propulsive efficiency strongly favors larger shroud inclination, where with the increasing inclination, the axial inflow velocity decreases. The reduction in inflow velocity increases the propeller efficiency as previously described in Section 6.1.1. To observe how increasing the shroud incidence affects the inflow to the propeller, the axial velocity inflow field at $i_{\text{shroud}}$ = 8 deg is shown in Figure 7.46a. This propeller plane normal inflow velocity $V_a$ at a shroud incidence angle of 8 deg shows a lower inflow velocity than the baseline case showing around a 5% reduction in $V_a/V_\infty$. As shown in Figure 7.46b, the largest reduction of axial velocity is located in proximity to the shroud, reducing the velocity to 0.98 $V_\infty$, when compared to the baseline OTW configuration where $i_{\text{shroud}}$ = 5 deg. Increasing the shroud inclination reduces the downwash expe-

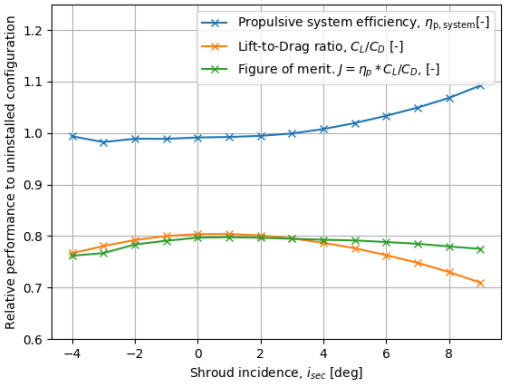


Figure 7.45: Change in performance as result of variation of the shroud incidence angle $i_{\text{shroud}}$

rienced by the propeller disk, which will reduce the propeller efficiency and in plane propeller force ($F_{Z'}$). The reduction in downwash is around 1 degree when increasing the shroud incidence form $i_{\text{shroud}}$ = 5 deg to $i_{\text{shroud}}$ = 8 deg.

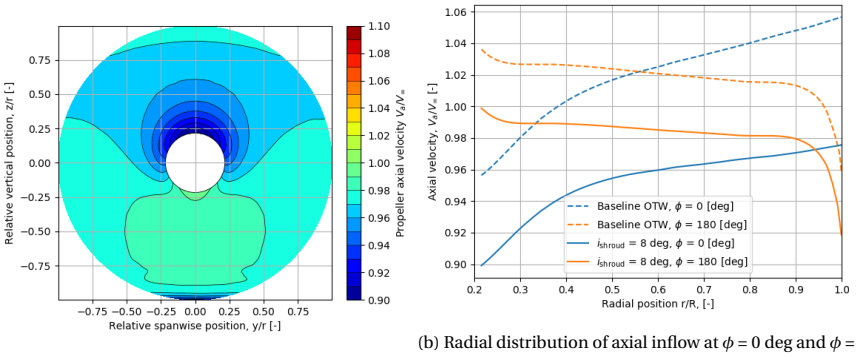


(a) Axial inflow

(b) Radial distribution of axial inflow at $\phi$ = 0 deg and $\phi$ = 180 deg

Figure 7.46: Propeller-off propeller plane normalized axial velocity at $i_{\text{shroud}}$ = 8 deg

The resulting net axial thrust distribution on the disk at $i_{\text{shroud}}$ = 8 deg is shown in Figure 7.47, showing an increase in loading in the upwards moving blade. When looking at the propeller efficiency along the azimuthal location in Figure 7.48, the loading on the disk at $\phi$ = 110 deg is similar to the baseline configuration and increases when moving away from this azimuthal location. The increase in propeller efficiency with increasing shroud inclination was also found by a similar investigation to the shroud incidence in an analysis on an OTW system performed by Khajehzadeh [33]. Results were obtained similarly at at constant propeller power, but not at a constant lift coefficient.

With the increasing shroud incidence, the loading on the shroud naturally increases

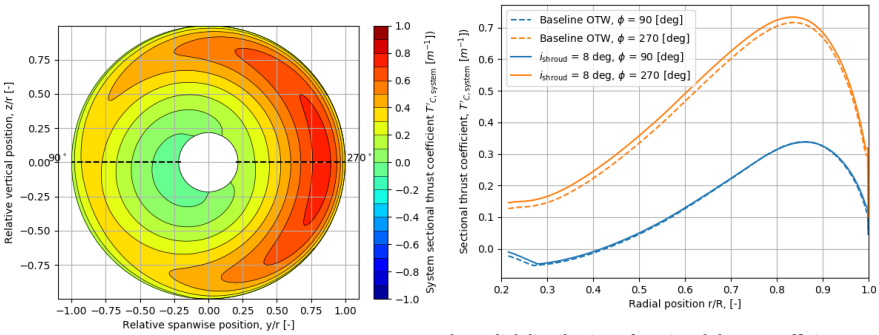


(a) Sectional net axial thrust distribution

(b) Radial distribution of sectional thrust coefficient at $\phi = 90$ deg and $\phi = 270$ deg

Figure 7.47: Net axial thrust contour and propeller efficiency at $i_{\text{shroud}} = 8$ deg

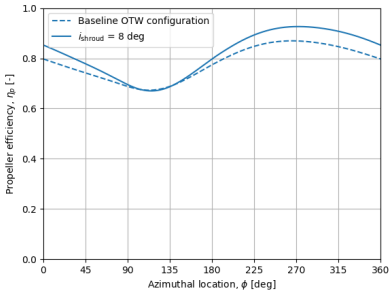


Figure 7.48: Propeller efficiency along the azimuthal location of the disk at $i_{\text{shroud}} = 8$ deg compared to the baseline OTW configuration where $i_{\text{shroud}} = 5$ deg

and with a constant lift coefficient, this means a reduction in system angle of attack follows lowering the loading on the wing. This mechanism is visible in Figure 7.49, where the reduction in suction on the top surface of the wing is found and the increment of suction on the shroud is found. It must be noted that the suction profile on the shroud at the larger shroud inclinations is not ideal with the sharp suction peak and resulting steep adverse pressure gradient following this. To assess the impact of this on the friction drag, the change in drag contributions while varying the shroud inclination are shown in Figure 7.50. This figure shows that the change in pressure drag is dominant at high shroud inclinations. The friction drag on the wing does however shows to be increasing with lower shroud inclinations. The sub optimal top surface pressure distribution on the nacelle can be mitigated by increasing the camber to the shroud profile. The largest contribution to the total drag is the increment in pressure drag, which is lowest at around a shroud incidence of 0 degrees. In this bi-planing configuration, while increasing the shroud incidence, the pressure drag of the shroud increases strongly, while the pressure drag of the wing decreases strongly. This pressure drag behavior was similarly found by

Khajehzadeh [33].

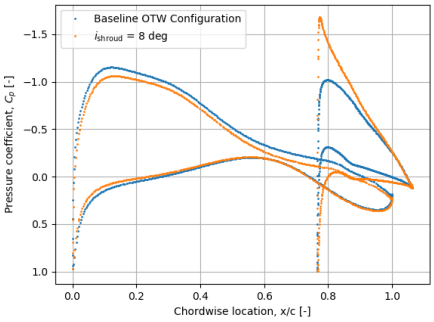


Figure 7.49: Wing and shroud pressure coefficient at $i_{\text{shroud}}$ = 8 deg compared to the baseline OTW configuration where $i_{\text{shroud}}$ = 5 deg

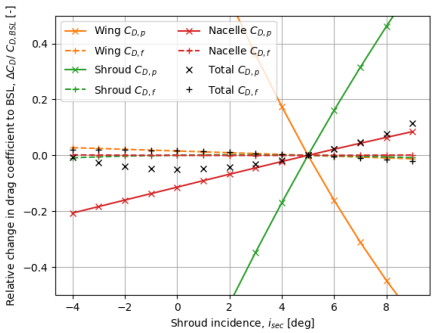


Figure 7.50: Relative change in drag coefficient as normalized by the baseline drag coefficient while varying the shroud inclination

## 7.6. SHROUD CHORD

Figure 7.51 shows the sensitivity to changing the shroud chord length, illustrating the impact on propulsive efficiency and system lift-to-drag. The OTW configuration favors a shorter chord as a result of the reduction in friction drag improving the system lift-to-drag ratio. This trend points to an optimal un-shrouded configuration, which may be limited in terms of the structural design of the system. With this trend, it is observed that at this specific shroud inclination, the shroud does not improve the propeller efficiency enough to compensate for the additional drag. At a larger shroud inclination, the impact on propeller efficiency is expected to be larger following the large increase of propeller efficiency found in Section 7.5. This will however come with the additional penalty on drag as found when increasing the shroud incidence.

The effect of the increase in drag is further highlighted in Figure 7.52, where a break-

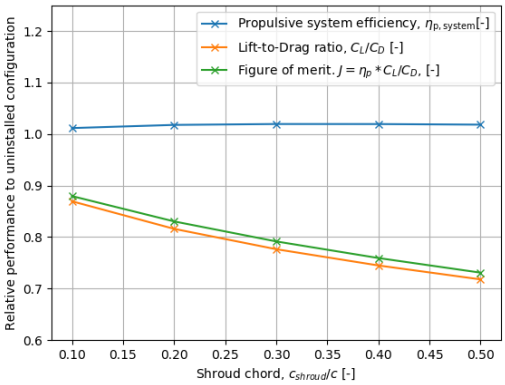


Figure 7.51: Change in performance as result of variation of the shroud chord length $c_{\text{shroud}}/c$

down of the drag contributions is shown. The figure shows both the change in pressure and friction drag as normalized by the total drag coefficient of the baseline OTW configuration. The reduction of the shroud chord has a strong impact on the wing and shroud pressure drag, where the wing pressure drag reduces with a longer shroud chord and the shroud pressure drag increases with the increase of shroud chord. These variations in pressure drag ultimately counteract each other resulting in a slight sensitivity to the total pressure drag with variation of shroud chord, where a reduction in pressure drag is found with a reduction in shroud chord. The increment of friction drag is the more significant parameter in the change in total drag, following Figure 7.52.

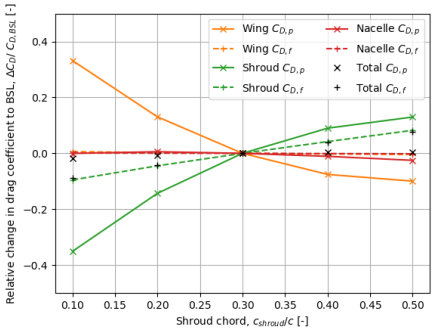


Figure 7.52: Change in pressure and friction drag coefficients as result of variation of propeller tip clearance $\epsilon/D_{\text{p}}$

## 7.7. SHROUD POSITION

The shroud position is defined relative to the propeller upper tip location, where increasing the $x_p/c_{\text{sec}}$ moves the shroud upstream. A geometric illustration of changing

the relative shroud position to $x_p/c_{sec} = 0.5$ is visualized in Figure 7.53. The sensitivity to the shroud position is relatively low as shown in Figure 7.54. The lift-to-drag ratio slightly favors a lower $x_p/c_{sec}$ and therefore downstream shroud location, which is maximum at $x_p/c_{sec} = 0.4$. The efficiency of the propeller rather favors a lower $x_p/c_{sec}$ and more downstream shroud location. The effect on the lift over drag ratio is a similar order as the propulsive system efficiency and the selected figure of merit is optimal at $x_p/c_{sec} = 0.25$.

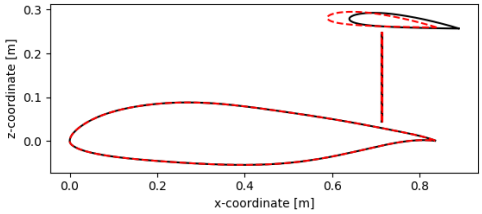


Figure 7.53: Geometrical illustration of $x_p/c_{sec} = 0.5$ (red) compared to the baseline OTW configuration $x_p/c_{sec} = 0.3$ in black

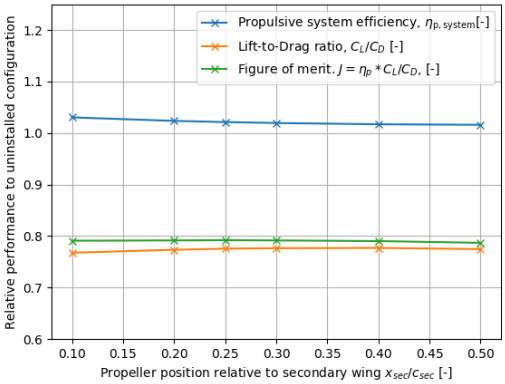


Figure 7.54: Change in performance as result of variation of the shroud position

The larger efficiency at $x_p/c_{sec} = 0.1$ originates from the lower axial inflow velocities, which are shown in Figure 7.55. The axial flow velocity reduces most close to the shroud and a more uniform inflow field is found at $x_p/c_{sec} = 0.1$.

The change in shroud position affects the lift and drag contribution by the propeller as seen in Figure 7.56. Both the propeller contribution to the $\Delta C_L$ and $\Delta C_D$ increase by moving the shroud downstream. The $\Delta C_L$ trend is relatively linear, while the $\Delta C_D$ responds strongest at low $x_p/c_{sec}$. The reduction of $\Delta C_L$ observed with increasing $x_p/c_{sec}$ follows from the additional shroud chord experiencing the suction upstream of the propeller, reducing the lift. This additional suction on the shroud surface does reduce the $\Delta C_D$ following additional suction present on the shroud in the direction of flight.

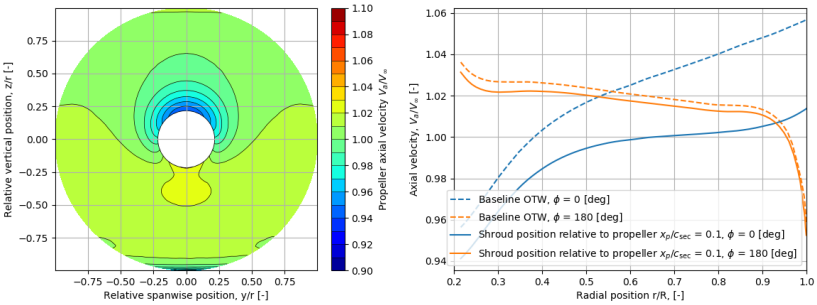


(a) Normalized axial flow velocity contour

(b) Radial velocity profiles at $\phi = 0$ deg and $\phi = 180$ deg

Figure 7.55: Propeller-off propeller plane velocity fields at $x_p/c_{\text{sec}} = 0.1$ compared to the baseline OTW configuration $x_p/c_{\text{sec}} = 0.3$

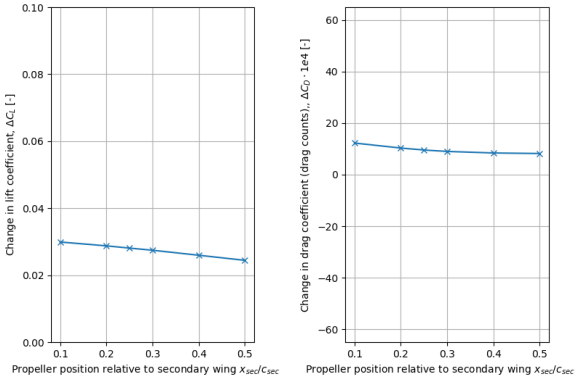


(a) Lift coefficient

(b) Drag coefficient

Figure 7.56: Change in lift and drag coefficient with $P_C = 0.162$ compared to to propeller-off $P_C = 0$ at various shroud axial locations ($x_p/c_{\text{sec}}$)

## 7.8. WING SHAPE VARIATION

The wing shape under the propeller has been varied to analyze the impact on the OTW system performance. The geometries are selected to alter the inflow angle and axial velocity experienced by the propeller affecting the efficiency of the propeller. Additionally, these changes in geometry will have an effect on the pressure drag of the wing by following the change in direction of the normal forces of the local geometry. A point to be made, is that these geometries are not aimed to be structurally viable and purely the aerodynamic effects are investigated. Therefore, some geometries might not be suitable for a final wing design. Four elementary geometries are selected and feature either a local valley, hill, step-down and step-up in the surface below the propeller as shown in Figure 7.57. The geometries are selected to be simple to allow for a more unobstructed

understanding of the aerodynamic effects when comparing the results back to the baseline OTW configuration. Each shape is run with with two steps to observe if the trend observed with a geometry change is continued or if the trend drops off. As can be seen from figure Figure 7.57a and Figure 7.57b, the valley and hill geometries also alter the vertical position of the shroud as a result of the constant tip clearance, which is not the case with the step down and step up geometries. These geometries are constructed using a set of 20 CST coefficients on the top and bottom surface defining the main wing airfoil shape. The increased CST coefficients are selected to obtain a CST control point every 0.05c. The different geometries are build by altering three CST coefficients, the coefficient at ($X_p/c$ = 0.85c), in front ($X_p/c$ = 0.80c) and behind the propeller location ($X_p/c$ = 0.90c). For reference on the lift-to-drag performance, these geometries are simulated in a propeller-off condition at constant lift coefficient and power coefficient. A summary of the lift-to-drag performance for both the propeller-on and propeller-off case evaluated at a constant lift coefficient of $C_L$ = 0.7272, is summarized in Table 7.6.

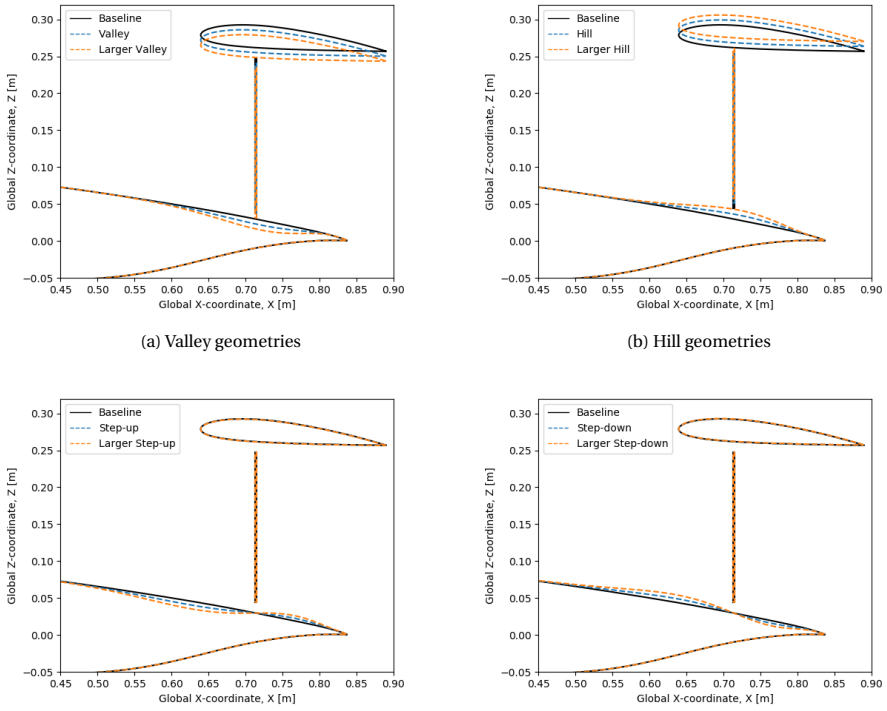


(a) Valley geometries

(b) Hill geometries

(c) Step-up geometries

(d) Step-down geometries

Figure 7.57: Wing shape variations

The change in the propulsive system efficiency and lift-to-drag ratio by changing the local wing shape is summarized in Figure 7.58. The x-axis in these figures show the effect of moving away form the baseline OTW configuration.

Table 7.6: Summary of lift to drag ratios for different wing shapes at $P_C = 0$ (propeller-off) and $P_C = 0.162$ (propeller-on) a constant lift coefficient of $C_L = 0.7272$

| Geometry | Baseline | Valley | Large valley | Hill | Larger hill | Step-up | Larger step-up | Step-down | Larger step-down |
|---|---|---|---|---|---|---|---|---|---|
| $C_L/C_D$ [-], $P_C = 0$ | 40.10 | 40.35 | 40.31 | 39.48 | 38.20 | 39.88 | 39.12 | 39.90 | 39.13 |
| $(C_L/C_D)/(C_L/C_D)_{BSL}$ [-], $P_C = 0$ | 1 | 1.006 | 1.005 | 0.984 | 0.952 | 0.995 | 0.975 | 0.995 | 0.976 |
| $C_L/C_D$ [-], $P_C = 0.162$ | 38.36 | 37.54 | 36.49 | 38.69 | 37.78 | 38.44 | 37.77 | 37.76 | 36.40 |
| $(C_L/C_D)/(C_L/C_D)_{BSL}$ [-], $P_C = 0.162$ | 1 | 0.979 | 0.951 | 1.009 | 0.985 | 1.002 | 0.984 | 0.984 | 0.949 |
| $\eta_{p,system}$, $P_C = 0.162$ | 0.8154 | 0.8315 | 0.8508 | 0.8031 | 0.7955 | 0.8126 | 0.8117 | 0.8185 | 0.8212 |
| $\eta_{p,system}/(\eta_{p,system})_{BSL}$, $P_C = 0.162$ | 1.000 | 1.020 | 1.043 | 0.985 | 0.976 | 0.997 | 0.995 | 1.004 | 1.007 |

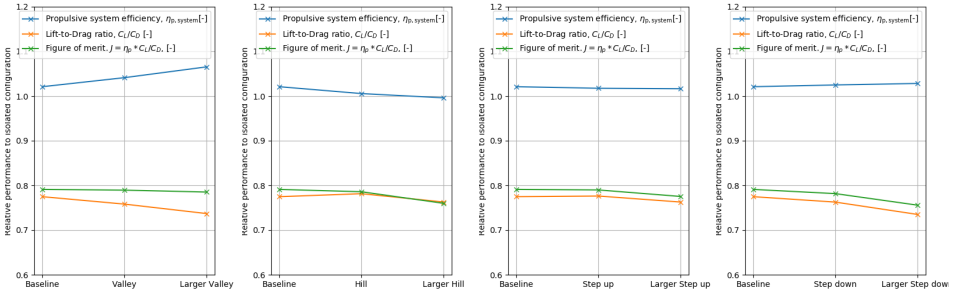


(a) Valley geometries (b) Hill geometries (c) Step-up geometries (d) Step-down geometries

Figure 7.58: Change in performance as result of varying the local wing shape below the propeller

The valley geometries have the strongest positive impact on the propulsive efficiency. To investigate the reason for this increment in propulsive efficiency, the change in axial inflow and upwash to the propeller are shown in Figure 7.59. The axial inflow to the propeller is reduced, particularly below the propeller with the propeller disk sitting in the wing boundary layer. Reducing the axial inflow velocity is observed to increase the propulsive efficiency as explained in Section 6.1.1. The effect observed here is expected to vary with Reynolds number as the boundary layer profile at higher Reynolds numbers will be thinner and the increment in propeller efficiency is expected to be lower as a result.

The valley geometries show potential in the propeller-off simulations, but when introducing the propeller, their performance suffers significantly. The isolated large valley geometry does not show the significant increment in drag coefficient, but rather shows a 0.5% reduction in drag compared to the baseline wing as can be seen from Table 7.6. The adverse pressure gradient induced by the propeller is therefore likely the reason for the increment in drag when introducing the propeller. To investigate the change in drag further, the pressure distributions are shown for the large valley geometry at $P_C = 0.162$ and $P_C = 0$ in Figure 7.60. The valley introduces additional pressure on the top surface of the main wing and increased pressure on the lower surface of the shroud, where the increased pressure on the lower surface of the shroud follows from the closer position to the wing. With this geometry, the increased suction the propeller introduces, as observed in Figure 7.60b, will have an additional pressure vector in the drag direction given the local shape of the valley upstream of the propeller which likely is the reason for the

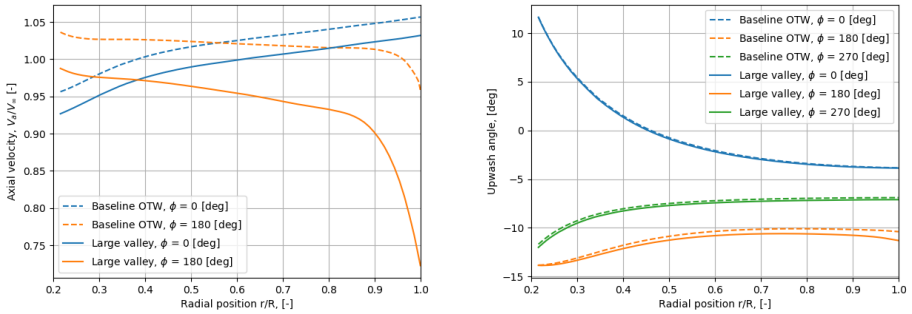


(a) Normalized axial flow velocity at $\phi$ = 0 deg and $\phi$ = 180 deg

(b) Upwash angle at $\phi$ = 0,180,270 deg

Figure 7.59: Radial velocity profiles of the large valley geometry compared to the baseline configuration at $C_L$ = 0.7272 and $P_C$ = 0.162

increment in pressure drag of the system.

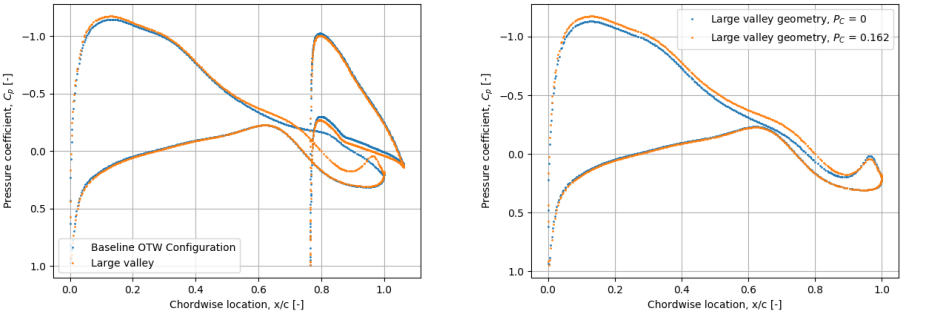


(a) Pressure coefficient compared to the baseline OTW configuration

(b) Pressure coefficient on the main wing at $P_C$ = 0.162 and $P_C$ = 0

Figure 7.60: Large valley geometry pressure coefficient the mid-plane compared to the baseline OTW configuration and propeller-off condition

The second set of geometries showing potential in increasing the propeller efficiency is the step-down geometries following Figure 7.58d. Figure 7.61 shows the change in axial inflow and upwash in to the propeller disk. Compared to the large valley results, the reduction of axial velocity close to the wing boundary layer is still present, but to a smaller extent. On the upper part of the propeller disk, the axial flow velocity is observed to increase instead. From Figure 7.61b it shows that the downwash into the propeller disk has been increased, particularly close to the wing surface. The additional downwash into the propeller is expected to increase the propeller efficiency according to investigation done in Section 6.1.1

The hill geometry would be expected to improve the $\Delta C_D$ as induced by the propeller following the study done on the axial propeller position Section 7.2, where the largest

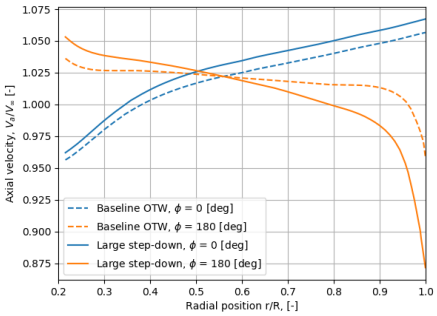


(a) Normalized axial flow velocity at $\phi = 0$ deg and $\phi = 180$ deg

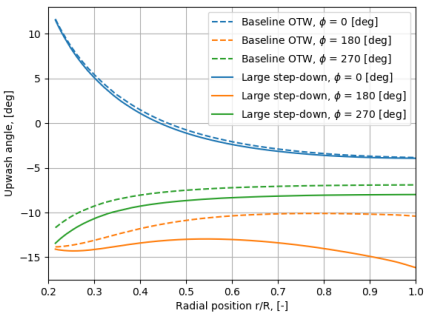


(b) Upwash angle at $\phi = 0,180,270$ deg

Figure 7.61: Radial velocity profiles of the large step-down geometry compared to the baseline configuration at $C_L = 0.7272$ and $P_C = 0.162$

drag reduction was observed to be present at the location of maximum thickness. This mechanism does seem to hold up following the results presented in Table 7.6, where introducing the propeller shows an improvement compared to the propeller-off lift to drag ratio. The propeller efficiency reduces following additional axial flow velocity into the propeller disk reducing the propulsive efficiency as can be seen in Figure 7.62a.

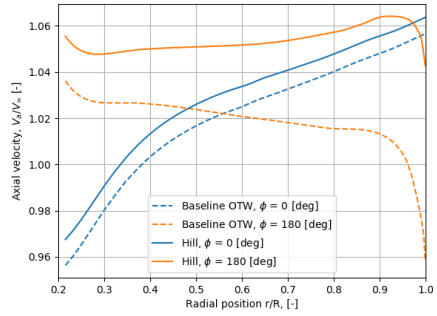


(a) Normalized axial flow velocity at $\phi = 0$ deg and $\phi = 180$ deg

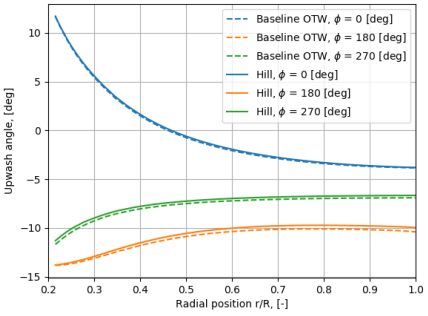


(b) Upwash angle at $\phi = 0,180,270$ deg

Figure 7.62: Radial velocity profiles of the hill geometry compared to the baseline configuration at $C_L = 0.7272$ and $P_C = 0.162$

The step-up geometry has a comparable propulsive efficiency and lift-to-drag ratio resulting in a comparable performance to the baseline configuration. The step-up geometry increases the upwash perceived by the propeller disk reducing it's efficiency, but also reduces the axial flow velocity increasing propulsive efficiency as can be seen in Figure 7.63. These two effects seem to cancel each other out to a certain extent following the comparable performance to the baseline configuration.

The larger step-up geometry reduces the lift-to-drag ratio, which mainly is contributed

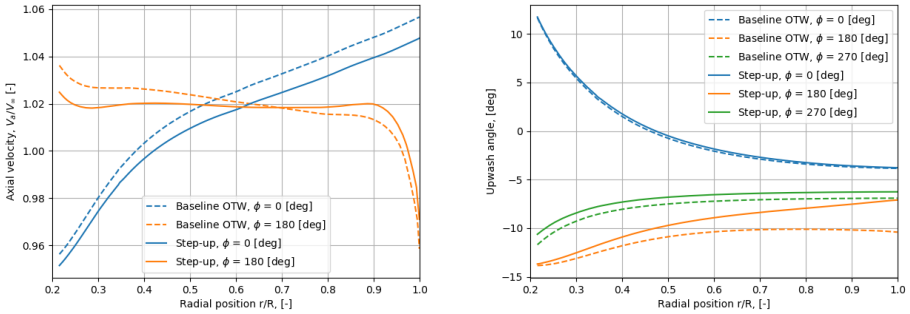


(a) Normalized axial flow velocity at $\phi$ = 0 deg and $\phi$ = 180 deg

(b) Upwash angle at $\phi$ = 0,180,270 deg

Figure 7.63: Radial velocity profiles of the step-up geometry compared to the baseline configuration at $C_L$ = 0.7272 and $P_C$ = 0.162

to the poorer performance of the propeller-off condition as can be seen from Table 7.6. The introduction of the propeller seem to improve the lift-to-drag ratio for the step-up and larger step-up geometries more than the baseline configuration. This response follows from the induced propeller suction on the wing, which in the larger step-up geometry has a greater force component in the direction of flight following the change in wing surface normal direction, which in term reduces drag.

## 7.9. IMPLICATIONS FOR FUTURE DESIGN AND OPTIMIZATION STUDIES

This section will reflect upon the results while keeping future design and optimization studies in mind. Optimization methods ordinarily want to limit the amount of design variables to be investigated and therefore knowing which parameters to include into a future study is very useful. Re-capping from the sensitivity studies, it is clear that certain parameters effect the performance more than others. Particularly, the propeller axial position, propeller incidence, shroud incidence and wing shape have a strong impact on the overall performance of the OTW system and are recommended to be included in future design and optimization studies. This study showed a preference for a more upstream axial propeller position following the smaller drag penalty observed. A more aft position of the propeller does allow for other opportunities regarding thrust vectoring which could be beneficial during take-off, so a consideration of the axial propeller location needs to be made with the performance of the entire flight envelope in mind. The wing shape has been observed to have a significant effect on both the propeller and the lift-to-drag performance and therefore will be a key parameter in future studies. A similar amount of control over the wing shape with a comparable amount of wing shape parameters is recommended, specifically at regions close to the propeller position. Improvement to the overall performance of the system by changing these parameters is highly likely given the strong sensitivities observed in this study.

To be kept in mind is that other orientations and positions of the shroud may need re-profiling of the shroud suction surface to allow for a more optimal shroud performance given the changing inflow angle to the shroud. From the results of this study, the chord

length of the shroud is to be minimized and therefore an investigation into the required support structures is in place. As discussed in Section 7.3, sufficient research into the diameter-to-chord ratio in OTW configurations is still lacking and it is expected to play a large role in the complete aircraft performance. Additionally, the effect of different disk loading in such a study is expected to play factor in the system performance. The propeller tip clearance is recommended to be reduced up to the potential limits imposed by the structural and noise constraints. When including a shroud into a OTW system, the position of the shroud relative to the propeller is observed to be relatively small in the current investigation done. However, this might change with different wing design, propeller inclination and propeller axial position. Therefore an investigation into the shroud axial position is recommended when these parameters are varied. In a similar geometrical set-up as investigated in this research, the shroud is recommended to be positioned such that it's thickest point is to be located closest to the propeller.

Propeller performance increased significantly with added geometry induced downwash and with a reduction of inflow velocity. Targeting these mechanisms is recommended in future studies when the goal is an improvement in propeller efficiency. The critical target in future research will be to improve the propeller performance, while not harming the performance of the overall system by an increase in pressure drag, which was often observed in this study.

To investigate what the potential benefit of an optimization study could be, an optimization study of the two most sensitive design variables has been performed, while keeping the propeller axial position in a aft-positioned location. The propeller inclination and shroud inclination are varied to see how a more optimal arrangement of these two parameters would look. Compared to the baseline OTW geometry presented in Table 3.2, the propeller axial position has been set to a more forward position equaling $x_p$ = 0.8c, following the benefit in system performance observed by moving propeller axial position more upstream. The resulting optimized geometry is shown in Figure 7.64, where the optimal propeller inclination $i_{prop}$ is equal to 0.33 deg and the optimal shroud inclination is equal to $i_{shroud}$ = 1.27 deg. In this configuration a 2.8% improvement to the figure of merit was obtained compared to the baseline OTW configuration. This improvement follows from the larger lift-to-drag ratio obtained, while sacrificing propulsive efficiency compared to the baseline OTW configuration.

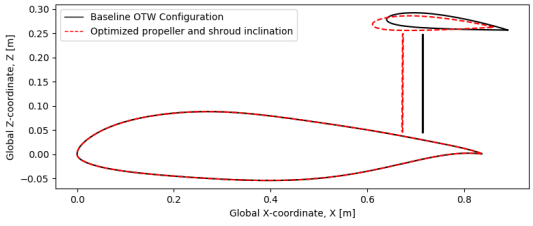


Figure 7.64: Geometrical illustration of the optimized propeller inclination and shroud inclination geometry compared to the baseline OTW configuration

# IV

# Conclusions and Recommendations

# 8

# CONCLUSIONS

In this research, a numerical investigation into the distributed over-the-wing propulsive configuration has been performed. For this, a numerical method has been developed to investigate the impact on the propeller performance and aerodynamic performance of the wing. Following this investigation, the research questions stated in Section 1.2 are answered in this section.

1. *Which type of model can accurately and swiftly estimate the performance of an over-the-wing propeller with constant lift and power coefficients?*

   (a) *How can the propeller performance be simulated and coupled to the aerodynamic performance of the system?*

   A critical part of the propeller performance estimation specific to this research is the ability to simulate the non-uniformity of the inflow to the propeller accurately. The propeller performance model used in this research makes use of a set of uninstalled propeller performance sensitivity maps to estimate the response of the local changes in tangential and axial advance ratio following from a non-uniform inflow field. This quasi-steady approach is extended by a correction to take into account unsteady effects resulting in a well approximated blade loading when compared to literature. This method is extended by a correction for the change in performance of the propeller pitch to allow for a more optimal propeller performance given the changes in inflow experienced throughout the different operating conditions. The propeller performance estimation method is highly computationally efficient and suitable for conceptual design phases. This propeller performance method is inserted in the CFD domain by using an actuator disk model.

   (b) *Which assumptions need to be made in the aerodynamic model?*

   To make this conceptual research computationally feasible, several assumptions had to be made. Firstly, the CFD model employs a Spalart–Allmaras turbulence model making use of wall functions, which model rather than

compute the aerodynamic behavior in close proximity to the wall. The velocity profiles assumed by the turbulence model will limit the accurate prediction of shear forces and location of flow separation. Secondly, the CFD simulations are performed in a steady state environment, which restricts the ability to model time-dependent phenomena and in particular interaction of the propeller tip vortices interacting with the wing boundary layer. Similar assumptions are made in the simulations run to obtain the uninstalled propeller performance sensitivity maps. A linear relation between the lift coefficient and the angle of attack is assumed to include the comparison of performance at a constant lift coefficient. The error from estimating this linear relation, is however assumed to be very small given the high degree of convergence of the lift coefficient in these simulations. The introduction of the actuator disk model means that the propeller blades themselves are not modeled. Therefore an estimation of the axial domain where the propeller disk momentum is inserted into the domain is made. This axial domain thickness is assumed to be in the same order as the propeller blade axial chord thickness.

(c) *How does experimental data compare to the numerical results obtained?*

Several aspects of the numerical results have been validated to experimental results. Firstly, the flat plate boundary layer profiles showed acceptable comparison to the experimental results, confirming acceptable performance of Spalart–Allmaras turbulence model and wall functions. To be kept in mind is that this compassion is done at a location without any pressure gradients present and therefore differences in boundary layer profiles are still expected in large adverse pressure gradients. The propeller induced pressure distributions on the wing showed fair agreement to the experimental pressure distributions, but lacked the capability of predicting the downstream impact on the wing following the introduction of the propeller at high thrust settings. At the high thrust settings the swirl was underestimated by the numerical model. At lower propeller thrust settings, the propeller induced pressures on the wing were qualitatively captured well, but the upstream peak change in pressure coefficient was overestimated by 28%. A region of a thinner boundary layer behind the propeller was not predicted by the numerical model. This discrepancy is expected to follow from the employment of the steady state simulations, which omits critical unsteady behavior present in this region. The numerical method fairs well in predicting the velocity fields downstream of the propeller in regions outside the boundary layer of the wing and nacelle geometries.

2. *How are the lift, drag and propeller efficiency affected by changing the design parameters of the system?*

   (a) *How does the inclusion of a shroud and nacelle structure affect the aero-propulsive efficiency?*

The inclusion of a un-inclined nacelle in a OTW configuration has a minimal impact on the wing pressure distribution. The inclusions showed an increase in suction upstream of the nacelle and a increases in wing pressure coefficient downstream of the nacelle. Given the size of the nacelle used in this numerical model, the uninstalled nacelle equals 17.8 % of the drag of the uninstalled wing drag. The nacelle is observed to have a strong impact on the inflow to the propeller in conditions where a large local angle of attack to the nacelle is observed. The axial flow velocity on the pressure surface of the nacelle is observed to reduce, whereas an increment in axial flow velocity is found on the suction side of the nacelle. At a nacelle angle of attack, the flow at either side is accelerated adding to the non-uniformity present in the propeller disk plane. This in turn has a strong impact on the propeller performance.

The shroud geometry introduced above the propeller in the OTW configuration follows with a 20% increment in drag following the additional wetted surface of the shroud. In an propeller-off OTW configuration, it is observed that the shroud increases the pressure on the isolated wing upper surface at $0.3 < x/c < 1.0$ for a shroud placed above the trailing edge of the wing. The inclusion of the shroud is observed to reduce the propeller induced lift and drag coefficient, given that propeller induced suction on propeller-upstream shroud geometry reduces the lift, countering the favorable increase in suction on the wing geometry. The inclusion of a shroud geometry is observed to have the potential of reducing the axial velocity into the propeller plane substantially, increasing propulsive efficiency. Studying this mechanism by varying the shroud incidence angle showed that this mechanism can be enhanced by increasing the shroud incidence, however this introduces a pressure drag penalty following the rotation of the normal force of the shroud towards direction of the drag vector. Following the significant increase in system drag from introducing a shroud geometry, reducing the shroud chord length is found to be beneficial for the lift-to-drag ratio of the system. The propulsive efficiency benefit of the inclusion of a shroud geometry did not outweigh the penalty in lift-to-drag ratio. The shroud axial position is observed to have a smaller impact on the system performance at the current geometrical configuration. The propeller efficiency has been observed to increase with a more downstream shroud position following a lower axial inflow into the propeller disk.

(b) *How does the position, tip clearance, diameter and inclination of the propeller affect the aero-propulsive efficiency?*

Expected from literature and confirmed in this research is that the axial propeller position in an OTW configuration plays a large role in the aero-propulsive performance of the system. The lowest propeller induced drag coefficient is observed to be found at a propeller location of 0.3c to 0.4c depending on the inclusion of a shroud geometry. In the un-shrouded configuration, a larger

increase in lift is observed by moving the propeller downstream following a larger region of suction on the wing. The propeller efficiency increases when moving the propeller downstream, following the lower axial velocities present in this region. Reducing propeller tip clearance is observed to increase the suction on the geometries upstream of the propeller disk. This increased suction increases the lift coefficient to a larger extent at lower tip clearances. A minor increase in propeller efficiency is observed following a very slight reduction in axial flow velocity when entering the propeller into the wing boundary layer. The overall sensitivity to this parameter is relatively small when compared with the sensitivity to other design variables, but an increase in aero-propulsive efficiency is expected at lower tip clearances. The propeller diameter-to-chord ratio is evaluated by varying the wing chord length, which introduces changes in the Reynolds number meaning that these results need to be interpreted with care. Increasing the diameter-to-chord ratio is observed to increase the propulsive efficiency slightly following a reduction in propeller angle of attack. The propeller inclination has a strong impact to both the lift-to-drag ratio of the system and the propulsive efficiency. Similar to an uninstalled propeller at an angle of attack, the propeller efficiency increases with increasing propeller angle of attack. In an uninstalled configuration, when looking at the propulsive efficiency in the direction of flight, the increment of the propeller in-plane forces mean that the propulsive efficiency is optimal at a zero angle of attack. This however is not the case in an installed OTW configuration, where the circulation generated by the wing introduces a substantial downwash angle into the propeller disk, increasing it's efficiency without penalizing it's performance by propeller in plane forces. Exploiting this mechanism, by inclining the propeller to create a larger negative angle of attack, was proven to be inefficient following the increment of drag coefficient at larger negative propeller inclinations.

(c) *How does the shape of the wing affect aero-propulsive efficiency?*

The geometry of the wing is altered locally in the proximity of the propeller to investigate the aero-propulsive efficiency of the system. Four types of elementary geometries including a local hill, valley, step-down and step-up have been evaluated. The valley geometries showed a strong increment in propulsive efficiency following a strong reduction of axial flow velocity into the propeller disk. This followed from a substantial increase in the boundary layer ingested by the propeller. This does increase the propulsive efficiency, however to be kept in mind is that this mechanism will be smaller at higher Reynolds numbers. Geometries that increased the downwash angle into the propeller disk by turning the flow downwards upstream of the propeller were observed to increase the propeller efficiency. This local orientation of the geometry upstream of the propeller does mean that the additional suction introduced by the propeller now increases the wing drag to a larger extent, reducing performance. Alternatively orienting the upstream geometry to have a greater normal component in the direction of flight is observed to be ben-

eficial for reducing the pressure drag after the introduction of the propeller. However, these geometries did come with an inherent drag penalty over the baseline wing.

3. *How does the overall aero-propulsive performance of the over-the-wing configuration compare to an uninstalled propeller-wing system?*

   (a) *How does the propulsive efficiency of a propeller in an over-the-wing configuration compare to the uninstalled propulsive efficiency?*

   The propulsive efficiency in the OTW configuration is observed to be affected by both the downwash perceived by the propeller following the circulation of the wing and the axial flow velocity into the propeller disk. The inherent benefit of the OTW configuration is the increase in propeller efficiency following the local propeller disk angle of attack even when the propeller is aligned in the direction of flight. This results in additional propulsive efficiency without being penalized by any in-plane propeller forces. The second mechanism present in the OTW configuration is the change in axial flow field as perceived by the propeller. This is highly dependent on the geometrical configuration of the system, given that inclining a shroud geometry can significantly reduce the axial flow velocity between the wing and shroud. This in turn can significantly increase the propulsive efficiency of the system, although it is observed in this study, that doing so comes at a penalty of lift-to-drag ratio.

   (b) *How is the lift and drag affected by the over-the-wing propulsive configuration?*

   The propeller introduces additional suction upstream of the propeller disk onto the geometries. The way this affects the system performance is highly dependent on the orientation of the geometry. The increased suction can lead to increased lift, increased drag or decreased drag. The largest increment in lift is found in an un-shrouded OTW propeller placed at the trailing edge of the wing, since at this position the increased suction covers the largest portion of the wing. Adding a shroud to this geometry, will reduce this benefit in lift, following the increased suction on the shroud lower surface. The largest reduction in drag can be observed by installing the propeller such that the additional suction provided onto the geometry contributes to a reduction in pressure drag. In the case of an un-shrouded OTW propeller, placing the propeller at the maximum thickness location of the wing will result in the largest drag reduction. Learning from this drag reduction mechanism, applying a local increment of thickness below the propeller onto the wing geometry is observed to reduce the drag to a larger extent.

   (c) *How does the combined overall aero-propulsive performance compare to an uninstalled system?*

The baseline OTW configuration shows a significant reduction in aero-propulsive performance as compared to the uninstalled system, following the additional friction drag of the shroud geometry. The un-shrouded baseline configuration has a slightly improved aero-propulsive performance compared to the uninstalled system. Moving the propeller axial position upstream is observed to show a significant increment in the lift-to-drag ratio of the system (45.5%) compared to the uninstalled system. When opted to include a shroud geometry for noise shielding or structural reasons, improvements to the OTW configuration are expected to reduce the current penalty, especially when opted for a smaller shroud structure.

To conclude, this research shows that there is a strong sensitivity in changing the propeller axial position, propeller incidence, shroud incidence and wing shape in an OTW configuration. These parameters have the ability to significantly increase the propulsive efficiency and show potential in enhancing the beneficial propeller-wing mechanisms following additional lift and drag augmentation. The shrouded OTW configuration did not show improvement over the uninstalled configuration, but the un-shrouded OTW configuration has significant potential.

# 9

# RECOMMENDATIONS

Looking ahead to further investigation in to the OTW distributed propulsive configuration several recommendations are made following the research performed in this report.

- The modeling of the impact of propeller pitch should ideally be implemented by expanding the propeller sensitivity maps. This will remove the introduction of additional modeling errors when removing the need to transition between a second lower order method to estimate the impact of changing propeller pitch.
- An investigation of the aerodynamic performance impact on the integration of alternative duct-like geometries could be interesting to determine the wetted surface penalty and impact on propulsive efficiency different propeller shrouding concepts introduce. In this study, the inclusion of the shroud significantly increased the friction drag of the over-the-wing propeller configuration, while gaining minimal benefit in propulsive efficiency and therefore the need of such a structure should be re-evaluated for an optimal final over-the-wing propulsive configuration.
- Developing a numerical model with an integrated way to easily perform investigations with different propeller diameters will be valuable in future studies given the lack of literature on the aerodynamic benefits of the amount of propulsors spanning the OTW array.
- The automated geometry creation, meshing and solving setup worked particularly well in evaluating a large amount of design variables and geometries. Once such a system is set-up and running, the freedom in design space was observed to be large enough for a wide design space, particularly useful in a preliminary design stage.
- Shroud alignment to the local flow should be a future consideration when evaluating shroud locations where the local shroud angle of attack changes significantly. This to prevent the observed suction peaks and following large adverse pressure gradients on the shroud at several geometries.
- This study focused on a aft-chord located OTW propeller keeping in mind the potential benefit in the take-off condition when including a propeller is inclined with

the flap. Further investigation to the high-lift condition of a shrouded OTW configuration will be needed to better understand the performance of such a system in a more complete flight envelope. However, flowing numerical simulations by Müller [22] and experimental investigation by de Vries et al. [20], it is recommended that such an investigation is done either experimentally or with a higher than RANS fidelity simulation given the complexity and unsteady nature of the problem.

- This study explored adaptation to the wing geometry to benefit the overall system performance, but with a similar goal, the optimal propeller design may be different in the installed OTW configuration compared to the isolated or tractor configuration. Therefore it would be interesting to investigate the adaptation of propeller design for a given non-uniform inflow as introduced in a OTW configuration.

- Although individual aspects of the model have been validated with experimental results, further experimental validation of the various parameters investigated in this study would give more confidence in the results and would be a logical next step in the investigation to shed a more complete picture of the aerodynamic performance of the investigated design variables.

# BIBLIOGRAPHY


[1] H. D. Kim, A. T. Perry, and P. J. Ansell, "A review of distributed electric propulsion concepts for air vehicle technology", in 2018 AIAA/IEEE electric aircraft technologies symposium (EATS) (IEEE, 2018), pp. 1–21.

[2] N. K. Borer, J. M. Derlaga, K. A. Deere, M. B. Carter, S. Viken, M. D. Patterson, B. Litherland, and A. Stoll, "Comparison of aero-propulsive performance predictions for distributed propulsion configurations", in 55th aiaa aerospace sciences meeting (2017), p. 0209.

[3] C. Friedrich and P. A. Robertson, "Hybrid-electric propulsion for aircraft", Journal of Aircraft **52**, 176–189 (2014).

[4] J. Johnson Jr and E. White, "Exploratory low-speed wind-tunnel investigation of advanced commuter configurations including an over-the-wing propeller design", in Aircraft design, systems and technology meeting (1983), p. 2531.

[5] R. Cooper, W. McCann, and A. Chapleo, "Over wing propeller aerodynamics", in ICAS proceedings, Vol. 18 (American Institute of Aeronautics and Astronautics, 1992), pp. 266–266.

[6] L. Müller, W. Heinze, D. Kožulović, M. Hepperle, and R. Radespiel, "Aerodynamic installation effects of an over-the-wing propeller on a high-lift configuration", Journal of Aircraft **51**, 249–258 (2014).

[7] P. Marcus, "Aerodynamic modelling and performance analysis of over-the-wing propellers: a combined numerical and experimental study", MSc Thesis (TUDelft, 2018).

[8] National Aeronautics and Space Administration, *Strategic implementation plan 2017 update*, "https://www.nasa.gov/sites/default/files/atoms/files/sip-2017-03-23-17-high.pdf, [retrieved 21 June 2019], Washington DC, 2017.

[9] S. Kallas and M. Geoghegan-Quinn, *Flightpath 2050: europe's vision for aviation: report of the high level group on aviation research*, 2011.

[10] M. Hoogreef, R. Vos, R. de Vries, and L. L. M. Veldhuis, "Conceptual assessment of hybrid electric aircraft with distributed propulsion and boosted turbofans", in AIAA scitech 2019 forum (2019), p. 1807.

[11] H. D. Kim, "Distributed propulsion vehicles", 27th International Congress of the Aeronautical Sciences, ICAS (2010).

[12] N. K. Borer, M. D. Patterson, J. K. Viken, M. D. Moore, J. Bevirt, A. M. Stoll, and A. R. Gibson, "Design and performance of the nasa sceptor distributed electric propulsion flight demonstrator", in 16th AIAA aviation technology, integration, and operations conference (2016), p. 3920.

[13] D. J. Arend, J. D. Wolter, S. M. Hirt, A. Provenza, J. A. Gazzaniga, W. T. Cousins, L. W. Hardin, and O. Sharma, "Experimental evaluation of an embedded boundary layer ingesting propulsor for highly efficient subsonic cruise aircraft", in 53rd AIAA/SAE/ASEE joint propulsion conference (2017), p. 5041.

[14] J. Felder, H. Kim, and G. Brown, "Turboelectric distributed propulsion engine cycle analysis for hybrid-wing-body aircraft", in 47th AIAA aerospace sciences meeting including the new horizons forum and aerospace exposition, Orlando, Fl ,Jan. 5-8 (2009), p. 1132.

[15] J. Felder, M. Tong, and J. Chu, "Sensitivity of mission energy consumption to turboelectric distributed propulsion design assumptions on the n3-x hybrid wing body aircraft", in 48th AIAA/ASME/SAE/ASEE joint propulsion conference & exhibit (2012), p. 3701.

[16] H. D. Kim, G. V. Brown, and J. L. Felder, "Distributed turboelectric propulsion for hybrid wing body aircraft", 2008 International Powered Lift Conference Royal Aeronautical Society; July 22, 2008 - July 24, 2008; London; United Kingdom (2008).

[17] M. J. Armstrong, C. A. Ross, M. J. Blackwelder, and K. Rajashekara, "Trade studies for nasa n3-x turboelectric distributed propulsion system electrical power system architecture", SAE International Journal of Aerospace **5**, 325–336 (2012).

[18] L. L. M. Veldhuis, "Propeller wing aerodynamic interference", PhD thesis (TU Delft, 2005).

[19] B. Magliozzi, D. Hanson, and R. Amiet, "Propeller and propfan noise", NASA, Langley Research Center, Aeroacoustics of Flight Vehicles: Theory and Practice **1**, 1–64 (1991).

[20] R. de Vries, N. van Arnhem, F. Avallone, D. Ragni, R. Vos, G. Eitelberg, and L. L. M. Veldhuis, "Aerodynamic interaction between an over-the-wing propeller and the wing boundary-layer in adverse pressure gradients", in AIAA aviation 2019 forum (2019), p. 3035.

[21] B. Sören, "Aerodynamic interaction effects present in tiltable over-the-wing propeller systems: a numerical study", MSc Thesis (TUDelft, 2020).

[22] L. Müller, D. Kozulovic, and J. Friedrichs, "Unsteady flow simulations of an over-the-wing propeller configuration", in 50th AIAA/ASME/SAE/ASEE joint propulsion conference (2014), p. 3886.

[23] A. T. Perry, P. J. Ansell, and M. Kerho, "Aero-propulsive and propulsor cross-coupling effects on a distributed propulsion system", in 2018 AIAA aerospace sciences meeting (2018), p. 2051.

[24] L. Müller, D. Kožulović, and R. Radespiel, "Aerodynamic performance of an over-the-wing propeller configuration at increasing mach number", CEAS Aeronautical Journal **5**, 305–317 (2014).

[25] L. Müller, D. Kozulovic, M. Hepperle, and R. Radespiel, "The influence of the propeller position on the aerodynamics of a channel wing", in Proceedings of deutscher luft-und raumfahrtkongress (2012).

[26] M. Rwigema, "Propeller blade element momentum theory with vortex wake deflection", in Proceedings of the 27th congress of the international council of the aeronautical sciences, nice, france, september (2010), pp. 19–24.

[27] B. W. McCormick, *Aerodynamics aeronautics and flight mechanics john wiley & sons inc* (New York NY, 1979).

[28] Q. R. Wald, "The aerodynamics of propellers", Progress in Aerospace Sciences **42**, 85–128 (2006).

[29] D. Black and C. Rohrbach, "Shrouded propellers-a comprehensive performance study", in 5th annual meeting and technical display (1968), p. 994.

[30] D. Küchemann and J. Weber, *Aerodynamics of propulsion*, Vol. 2 (McGraw-Hill, 1953).

[31] L. L. M. Veldhuis and A. Khajehzadeh, "Analysis and design of a wing trailing edge mounted over-the-wing distributed propeller propulsion system", in AIAA aviation 2019 forum (2019), p. 3692.

[32] H. Mourão Bento, "Aerodynamic interaction effects of circular and square ducted propellers", MSc Thesis (TUDelft, 2019).

[33] A. Khajehzadeh, "Analysis of an over the wing based distributed propulsion system", MSc Thesis (TUDelft, 2018).

[34] N. van Arnhem, R. de Vries, T. Sinnige, R. Vos, G. Eitelberg, and L. L. Veldhuis, "Engineering method to estimate the blade loading of propellers in nonuniform flow", AIAA Journal, 1–15 (2020).

[35] B. Kulfan and J. Bussoletti, ""Fundamental"parameteric geometry representations for aircraft component shapes", in 11th AIAA/issmo multidisciplinary analysis and optimization conference (2006), p. 6948.

[36] V. Sripawadkul, M. Padulo, and M. Guenov, "A comparison of airfoil shape parameterization techniques for early design optimization", in 13th AIAA/issmo multidisciplinary analysis optimization conference (2010), p. 9050.

[37] M. Ceze, M. Hayashi, and E. Volpe, "A study of the cst parameterization characteristics", in 27th AIAA applied aerodynamics conference (2009), p. 3767.

[38] L. Boermans and P. Rutten, *Two-dimensional aerodynamic characteristics of airfoil nlf-mod22 with fowler flap*, tech. rep. (Internal Report LSW-95-3, Delft University of Technology, 1995).

[39] N. van Arnhem, R. de Vries, R. Vos, and L. L. Veldhuis, "Aerodynamic performance of an aircraft equipped with horizontal tail mounted propellers", in AIAA aviation 2019 forum (2019), p. 3036.

[40] R. de Vries, N. van Arnhem, F. Avallone, D. Ragni, R. Vos, G. Eitelberg, and L. L. Veldhuis, "Experimental investigation of over-the-wing propeller–boundary-layer interaction", AIAA Journal **59**, 2169–2182 (2021).

[41] R. de Vries, N. van Arnhem, T. Sinnige, R. Vos, and L. L. Veldhuis, "Aerodynamic interaction between propellers of a distributed-propulsion system in forward flight", Aerospace Science and Technology, 107009 (2021).

[42] Q. Li, K. Öztürk, T. Sinnige, D. Ragni, G. Eitelberg, L. L. M. Veldhuis, and Y. Wang, "Design and experimental validation of swirl-recovery vanes for propeller propulsion systems", AIAA Journal **56**, 4719–4729 (2018).

[43] J. H. Ferziger, M. Perić, and R. L. Street, *Computational methods for fluid dynamics*, Vol. 3 (Springer, 2002).

[44] A. Fluent et al., "Ansys fluent theory guide", ANSYS Inc., USA **15317**, 724–746 (2011).

[45] H. Schlichting and K. Gersten, "Boundary layer theory (chapter 21)", Springer **8**, 523 (1979).

[46] P. Spalart and S. Allmaras, "A one-equation turbulence model for aerodynamic flows", in 30th aerospace sciences meeting and exhibit (1992), p. 439.

[47] T. C. Stokkermans, N. Van Arnhem, T. Sinnige, and L. L. Veldhuis, "Validation and comparison of rans propeller modeling methods for tip-mounted applications", AIAA Journal **57**, 566–580 (2019).

[48] B. Stanković, A. Stojanović, M. Sijerčić, S. Belošević, and S. Čantrak, "Evaluation and limitations of standard wall functions in channel and step flow configurations", Journal of Serbian Society for Computational Mechanics **8**, 1–22 (2014).

[49] W. R. Sears, "Some aspects of non-stationary airfoil theory and its practical application", Journal of the Aeronautical Sciences **8**, 104–108 (1941).

[50] M. Drela and H. Youngren, "Xrotor", URL: http://web.mit.edu/drela/Public/web/xrotor, [Accessed 06 April 2021].

[51] J. Sørensen, W. Shen, and X. Munduate, "Analysis of wake states by a full-field actuator disc model", Wind Energy: An International Journal for Progress and Applications in Wind Power Conversion Technology **1**, 73–88 (1998).

[52] R. de Vries, M. Hoogreef, and R. Vos, "Preliminary sizing of a hybrid-electric passenger aircraft featuring over-the-wing distributed-propulsion", in AIAA scitech 2019 forum (2019), p. 1811.

[53] M. Hoogreef, R. de Vries, T. Sinnige, and R. Vos, "Synthesis of aero-propulsive interaction studies applied to conceptual hybrid-electric aircraft design", in AIAA scitech 2020 forum (2020), p. 0503.

[54] IHS, *Jane's all the worlds aircraft*, Accessed 21 August 2021. URL: https://janes.ihs.com.

[55] L. Eça and M. Hoekstra, "A procedure for the estimation of the numerical uncertainty of cfd calculations based on grid refinement studies", Journal of computational physics **262**, 104–130 (2014).

[56] M. Drela, "Xfoil: an analysis and design system for low reynolds number airfoils", in *Low reynolds number aerodynamics* (Springer, 1989), pp. 1–12.

[57] A. T. Wick, J. R. Hooker, and C. H. Zeune, "Integrated aerodynamic benefits of distributed propulsion", in 53rd AIAA aerospace sciences meeting (2015), p. 1500.

[58] L. E. Putnam, *Exploratory investigation at mach numbers from 0.40 to 0.95 of the effects of jets blown over a wing* (National Aeronautics and Space Administration, 1973).